Harald Thommesen, BSc

Simulation of radiation exposure in the atmosphere of the Earth caused by galactic and solar cosmic radiation

MASTER THESIS

For obtaining the academic degree
Diplom-Ingenieur

Master Programme of
Space Sciences and Earth from Space

Graz University of Technology

Supervisor:

Assoc.Prof. Dipl.-Phys. Dr.rer.nat. Wolfgang Sprengel

Institute of Material Physics

in cooperation with:

Seibersdorf Labor GmbH

Graz, May 2015

STATUTORY DECLARATION

I declare that I have authored this thesis independently, that I have not used other than the declared sources / resources and that I have explicitly marked all material which has been quoted either literally or by content from the used sources.

…… ……..

date (signature)

Acknowledgement
I could not have written this thesis without the support of my team colleagues at the *Seibersdorf Labor GmbH*. Therefore I am very grateful to them. Special thanks goes to Dipl. Ing. Dr. Peter Beck for welcoming me to his team, for giving me the opportunity to use the facility and also for his excellent leadership during the project. Also, I would like to thank Dipl. Ing. Marcin Latocha, my main contact person concerning all technical matters, for always taking the time to answer my many questions. His technical expertise was of great value to me.

Furthermore I want to thank my supervisor Assoc.Prof Dr. Wolfgang Sprengel from the *Graz University of Technology* for this competent support and cooperativeness, without which this work would not have been possible.

Last but not least, I thank my parents and my brother for their encouragement throughout this work and also throughout my entire studies.

Abstract

The Earth is constantly bombarded by high-energetic particles, which penetrate our atmosphere. They belong to the cosmic radiation and can be further classified according to their origin in a galactic and a solar component. When these particles hit the atmosphere, a multitude of particle interactions with the atmospheric molecules takes place. The result is the secondary cosmic radiation, which can, depending on its intensity, pose a threat to passengers and most of all to the crew on civilian aircrafts. The intensity of the secondary cosmic radiation depends heavily on four aspects. First of all, it is coupled to the galactic cosmic radiation flux, which anticorrelates with the solar activity. Secondly, the radiation exposure is a function of the flight altitude. Thirdly, the shielding effect of the magnetic field is latitude-dependent. The fourth aspect is the very sporadically occurring solar component. In the rare case that protons from a solar particle event hit the Earth, the radiation exposure in polar regions increases dramatically.

This work describes the development of a GEANT4-based simulation model that considers all the above mentioned aspects and returns the level of radiation exposure in the form of dosimetric quantities. Additionally, it presents simulation results produced by this very model that illustrate the magnitude and also the global distribution of radiation doses that arise from galactic and solar cosmic rays. Lastly, the model was used to estimate the absorbed radiation doses on long-distance flights during a solar energetic event.

Table of Contents

1 Introduction

The Earth is constantly hit by an ionizing particle radiation, called the *cosmic radiation*, which consists of a galactic and a solar component. Near the ground level this radiation is harmless, since most of its intensity is shielded by both the atmosphere and the magnetic field. At flight altitudes however, the situation looks very different because the shielding is a lot weaker. At these elevations, the radiation doses are by at least an order of magnitude higher than they are on the ground. The exact radiation doses depend on a multitude of parameters, such as altitude, geographical position and solar activity. Nonetheless, the biggest radiation doses occur, when solar energetic particles strike the Earth. These events are very rare, but when they do happen, there is a sharp increase of radiation exposure in the polar regions.

The aim of this thesis is to develop a simulation model that allows a real-time assessment of the radiation hazard in the atmosphere, so that the absorbed doses by aircraft personnel and passengers can easily be estimated. For this purpose it is necessary to determine the galactic and solar cosmic proton spectra and evaluate the radiation doses at a specific altitude and coordinate on Earth.

All the background knowledge that is necessary to successfully understand the content of this master thesis is given in Chapter 2. This includes an extensive description of the characteristics and the classification of cosmic radiation, what it depends on, and how its effects can be measured on Earth. Furthermore it sheds light on the particle interactions that take place in the atmosphere due to the bombardment with primary particles of the cosmic radiation. All results in this work are given in dosimetric quantities, therefore a detailed description of all units used is given Finally the simulation software that is used for the calculations of the particle interactions is explained.

The main part of this theses starts in chapter 3, which illustrates the structure and the components of the developed simulation model, as well as its further processing into a user-friendly programm. The calculation of the primary galactic and solar cosmic ray spectra as well as how they behave when they face the magnetic field of the Earth is described in chapter 3.3 sections 3.3.1 and 3.3.2 respectively.

In chapter 4 the ready-to-use simulation model is tested by comparing selected simulation results with reference values from the literature. Also a variety of simulation results for dose rates produced by the galactic component of the cosmic radiation is presented. These results demonstrate very well the dependence of the radiation exposure on altitude, geographical position and solar activity. The simulation model is not only validated by reference values from the literature, but also by data obtained from an in-flight measurement, which was performed in September 2014. The outcome of this validation is revealed in chapter 4.3.

As mentioned previously, the cosmic radiation is not only made up of a galactic but also of a solar component. This second part of the cosmic radiation is investigated in chapters 5 and 6, which include the evaluation of the radiation hazard during historic solar events.

2 Basics of Cosmic Radiation, Dosimetry and Simulation Techniques

This chapter offers a quick overview of the basic background knowledge that is necessary to better understand the content and the aim of this master thesis, such as dosimetric quantities, elementary particle physics, cosmic radiology and computer based simulation methods.

2.1 Types of cosmic radiation

Our planet is exposed to an uninterrupted bombardment of high energetic particles, which have their source outside the Earth. However, this fact was only discovered at the beginning of the last century as the result of studies aimed to explain the electric conductivity of gases. Originally, it was believed, that the conductivity of air originates only from ionization due to the emission of radioactive elements contained in the soil. Nevertheless, a residual conductivity was found that could not be easily explained. From 1911 to 1912, the Austrian physicist *Victor Franz Hess* performed several experiments using ionization chambers mounted on balloons with which he was able to demonstrate the altitude dependence of the electric current in an ion chamber. Against all expectations, the conductivity of air did not decrease with altitude but was actually several times greater at a height of 5350 meters than at sea level. Therefore, Hess concluded that a hitherto unknown radiation from outside the Earth must cause this conductivity increase. Furthermore, he ruled out the Sun as the newly discovered radiation source as experiments conducted at night did not show different results than those conducted during the day. [1] [2]

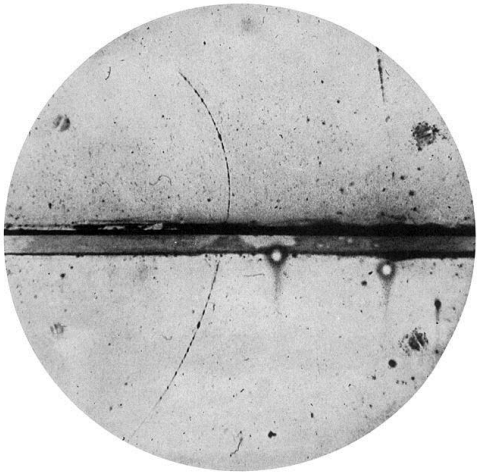

Figure 1: Positron track photographed by C. D. Anderson (1932), taken from ref. [2]

The discovery of the cosmic radiation was the very beginning of elementary particle physics, because back in these days, it was the only source of high-energy particles with which to conduct experiments. In fact, the first elementary particles were detected in the atmosphere of the Earth long before the first particle accelerator was built, such as the positron, the muon, the pion or the kaon. These by-products are also called 'secondary cosmic ray particles' and were first made visible in the 1930ies by *C. D. Anderson*. He used cloud chambers placed in strong magnetic fields where he was able to determine the trajectory, the energy, the mass and the charge of a particle. Figure 1 shows the track of the first positron ever identified. In 1936, Victor Franz Hess and C.D. Anderson were awarded the Nobel Prize in Physics for their discoveries. [2]

In the following decades many aspects of cosmic radiation were examined. Astrophysicists were interested in its origin, formation and composition while geophysicists dealt with its influence on the atmosphere and magnetosphere of the Earth. Particle physicists detected hitherto unknown or only postulated particles. With technological progress, it became possible to transport satellites and later on even humans into space which also made cosmic radiology an important topic in the field of biophysics.

At this point it has to be emphasized that cosmic radiation is, in fact, made up of particles and not electromagnetic radiation. This confusing expression came to be because at the time of the

discovery of cosmic radiation it was wrongly believed to consist mainly of gamma rays. Nonetheless, scientists still stick to the old expression.

Cosmic radiation can be classified into three categories, the *galactic cosmic radiation,* the *solar cosmic radiation* and the *secondary cosmic radiation.* [3]

The *galactic cosmic radiation* has its origin outside of the solar system but inside of our galaxy. It is also speculated that very high energetic rays (up to 10^{21} eV) are of extragalactic origin [2]. In addition to the radiation coming from the galaxy, there is another source of radiation, namely the Sun. At the time of solar maximum, huge amounts of energy are released in solar particle events (SPE). When such an event occurs, the low energy particle flux arriving at the Earth can be increased by several orders of magnitude. [1] This additional flux of low energy particles is the *solar cosmic radiation.* Furthermore, the Sun emits a continuous stream of particles which is called solar wind. The magnetic field of the Sun is glued to the plasma ("frozen-in") and as the solar wind moves radially away, the Sun rotates and the famous Parker-spiral is formed. The solar wind and the interplanetary magnetic field (IMF) impede the movement of the galactic cosmic rays and therefore its flux is modulated by the solar cycle. [1]

The primary cosmic radiation penetrates the atmosphere of the Earth, which leads to a variety of effects where the primary particles are quickly transformed into secondary particles, which again interact and produce even more secondary particles. The result is a so-called "particle shower" or "particle cascade". This newly produced *secondary cosmic radiation* can reach the surface of the Earth. Therefore it is also called *terrestrial cosmic radiation.* [3]

2.1.1 Galactic cosmic radiation

Galactic cosmic radiation (GCR) is a constant flux of particles, which only varies slowly with the state of the solar cycle. It impinges isotropically on the surface of Earth's atmosphere. Nowadays it is believed that the particles are accelerated in supernova explosions. Such an explosion occurs in our galaxy every 30 to 50 years, which would be enough to maintain the cosmic ray flux in a state of equilibrium. At the top of Earth's atmosphere the following composition is found: [1] [3]

- 85 % protons
- 14 % alpha particles
- 1 % heavier nuclei

The energy spectrum is usually defined as the number of particles (dN), per area (dF), per unit of time (dt), per solid angle (dΩ) and per kinetic energy (dE). [1]

Unit: $\mathrm{cm^{-2}\ s^{-1}\ sr^{-1}\ (GeV)^{-1}}$

$$\Phi = \frac{dN}{dF \cdot d\Omega \cdot dt \cdot dE} \tag{1}$$

Instead of the kinetic energy, the *magnetic rigidity R* can be used. The rigidity is a convenient unit for particle energies since particles with the same rigidity travel identical paths in a magnetic field. It is defined as

Unit: GV

$$R_p = \frac{pc}{q} \tag{2}$$

with *p* the momentum of the particle, *c* the speed of light *q* the charge of the particle. [1]

As mentioned previously, the shape of the GCR spectrum varies slowly in an 11-year solar cycle. During one solar cycle, the Sun changes from a quiet state to an active state. The activity is directly connected to the number of sunspots, which is counted by many observatories every day, see Figure 2. The increased emission of protons during the solar maximum and the elevated interplanetary magnetic field strength have the effect that particles from outside the solar system need more energy to overcome this barrier. Therefore, many particles in the low-energy region of the spectrum are lost. This variability of the proton flux with the solar cycle is demonstrated in Figure 3. For more details regarding the calculation of the GCR proton spectrum, see section 3.3.1.1 on page 26.

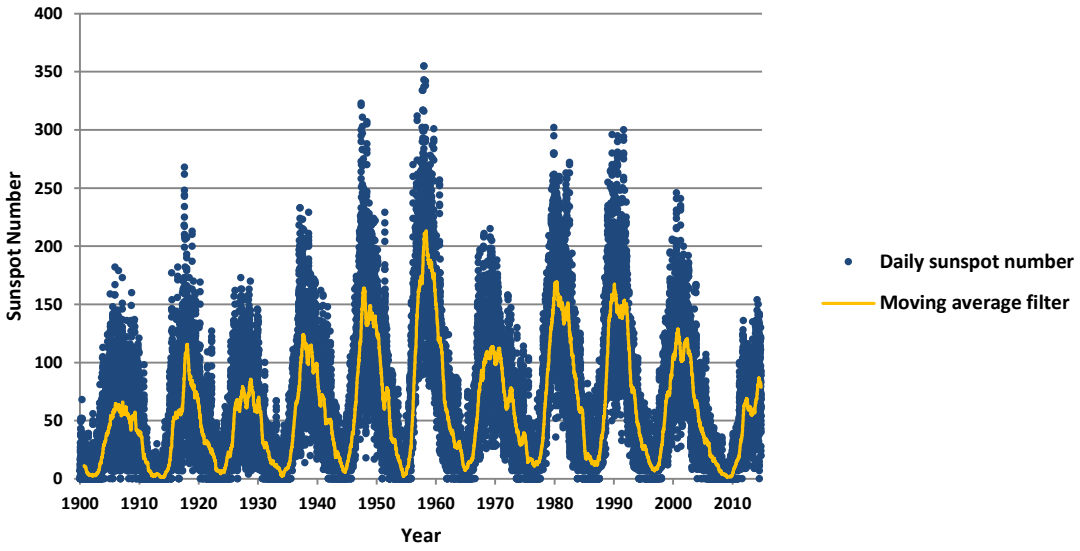

Figure 2: Daily total sunspot number since 1900 (Data from [4])

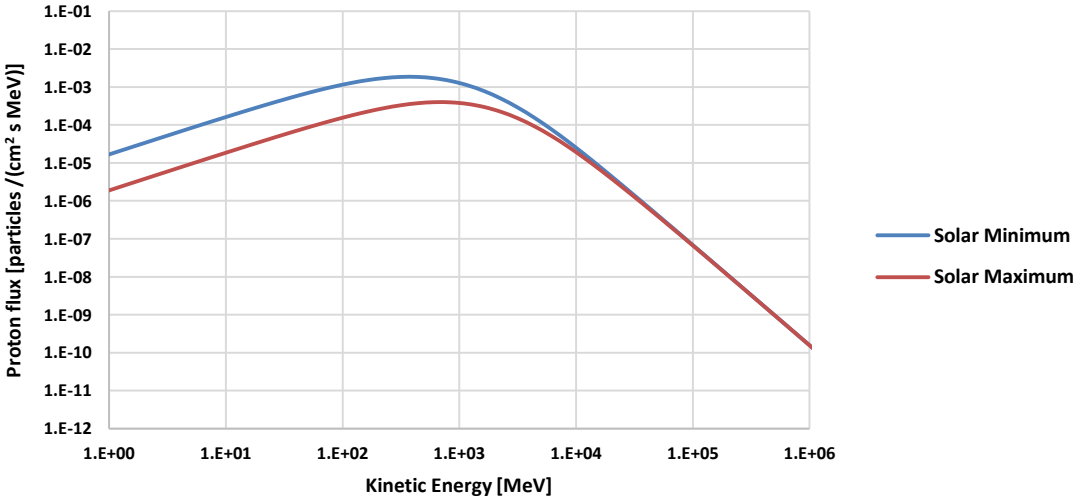

Figure 3: GCR Proton for solar minimum and solar maximum)

2.1.2 Solar cosmic radiation

The second contributor to the cosmic radiation is the Sun. In the quiet state of the Sun, it is largely low energetic solar wind emitted. However, when the Sun is active, along with the elevated output of solar wind, large amounts of high-energy particles are expelled in solar particle events. The energy spectrum of such an event is usually a lot softer than the GCR

spectrum and changes rapidly with time. The high-energy particles are the first ones to arrive at the orbit of the Earth and thus, at the beginning, the spectrum is quite hard. Later on, the distribution changes and the spectrum becomes softer and softer, as the low-energy particles catch up and the high-energy particles disappear. More details regarding the reconstruction and the shape of solar cosmic ray (SCR) spectra are given in section 3.3.1.2.

If an SPE is very energetic and its protons happen to strike the Earth, enhanced particle count rates can be detected on the surface of our planet. Such an event is called *Ground Level Enhancement (GLE)* and occurs, on average, about once per year. Since 1942 only 71 of these events were recorded, which are listed in Table 1. The magnitude of a flare is given by the increase of the count rate of a neutron monitor, see section 2.3.

Table 1: List of Ground Level Enhancements since 1942 (Data from [5] and [6]); the GLEs marked in red will be further investigated it section 5.1 starting on page 46

Event no.	Date (dd.mm.yyyy)	Increase	Event no.	Date (dd.mm.yyyy)	Increase
1	28.02.1942	--	**37**	26.11.1982	4 %
2	07.03.1942	--	**38**	07.12.1982	26 %
3	25.07.1946	--	**39**	16.02.1984	15 %
4	19.11.1949	--	**40**	25.07.1989	2 %
5	23.02.1956	--	**41**	16.08.1989	12 %
6	31.08.1956	--	**42**	29.09.1989	174 %
7	17.07.1959	--	**43**	19.10.1989	37 %
8	04.05.1960	--	**44**	22.10.1989	17 %
9	03.09.1960	--	**45**	24.10.1989	94 %
10	12.11.1960	--	**46**	15.11.1989	5 %
11	15.11.1960	--	**47**	21.05.1990	13 %
12	20.11.1960	--	**48**	24.05.1990	8 %
13	18.07.1961	--	**49**	26.05.1990	6 %
14	20.07.1961	--	**50**	28.05.1990	5 %
15	07.07.1966	1 %	**51**	11.06.1991	7 %
16	28.01.1967	17 %	**52**	15.06.1991	24 %
17	28.01.1967	17 %	**53**	25.06.1992	5 %
18	29.09.1968	3 %	**54**	02.11.1992	3 %
19	18.11.1968	3 %	**55**	06.11.1997	11 %
20	25.02.1969	1 %	**56**	02.05.1998	7 %
21	30.03.1969	6 %	**57**	06.05.1998	4 %
22	24.01.1971	16 %	**58**	24.08.1998	3 %
23	01.09.1971	14 %	**59**	14.07.2000	30 %
24	04.08.1972	10 %	**60**	15.04.2001	57 %
25	07.08.1972	5 %	**61**	18.04.2001	5 %
26	29.04.1973	4 %	**62**	04.11.2001	3 %
27	30.04.1976	4 %	**63**	26.12.2001	5 %
28	19.09.1977	3 %	**64**	24.08.2002	5 %
29	24.09.1977	7 %	**65**	28.10.2003	5 %
30	22.11.1977	13 %	**66**	29.10.2003	--
31	07.05.1978	84 %	**67**	02.11.2003	6 %
32	23.09.1978	7 %	**68**	17.01.2005	3 %
33	21.08.1979	4 %	**69**	20.01.2005	269 %
34	10.04.1981	1 %	**70**	13.12.2006	92 %
35	10.05.1981	2 %	**71**	17.05.2012	16 %
36	12.10.1981	11 %			

2.1.3 Secondary cosmic radiation

When the galactic and solar cosmic radiation hits the atmosphere, the particles (mainly protons) collide with the air molecules and a vast number of interaction processes takes place. As a result, new (secondary) particles are produced, such as pions, muons, positrons and electrons. These particles can start interactions on their own, if their energies are high enough. The result is particle cascades (see Figure 9), which have already been introduced earlier in this chapter. A more detailed explanation on the involved physical processes and cascade showers is given in section 2.4.

2.2 Influence of geomagnetic latitude

The intensity of particles arriving at a certain position on Earth does not only depend on the state of the solar cycle and on the occurrence of solar flares, but also on the *geomagnetic latitude*. When charged particles enter the magnetosphere of the Earth, their paths are strongly influenced by the direction (= inclination) and strength of the magnetic field as every movement perpendicular to it is superimposed by the Lorentz force. The resulting trajectory is either circular or helical, depending on whether the particle has a parallel velocity component or not. The radius of this motion is given by the *gyroradius* r_g [7]:

$$r_g = \frac{m \cdot v_\perp}{|q| \cdot B} \tag{3}$$

Here, m is the mass of the particle, $v_\perp$ the velocity component perpendicular to the magnetic field lines, q is the electric charge and B is the magnetic flux density.

In the equatorial plane, the magnetic field lines are almost horizontal, so particles that incident vertically from above are deflected and cannot propagate deeper into the magnetosphere. Near the poles however, where the magnetic field lines are almost vertical, incidenting particles have almost no velocity component perpendicular to the field lines and therefore they can penetrate easily into the atmosphere and even right down to the ground. This leads to a higher production rate of secondary particles than on low latitudes. To take this latitude dependence into account, one can calculate the minimum kinetic energy that a particle must have in order to enter the magnetosphere, depending on the magnetic field strength and orientation at a certain coordinate on Earth. This quantity is called *Vertical Cutoff Rigidity* R_{cv} and its unit is GV (see equation (2) on page 3).

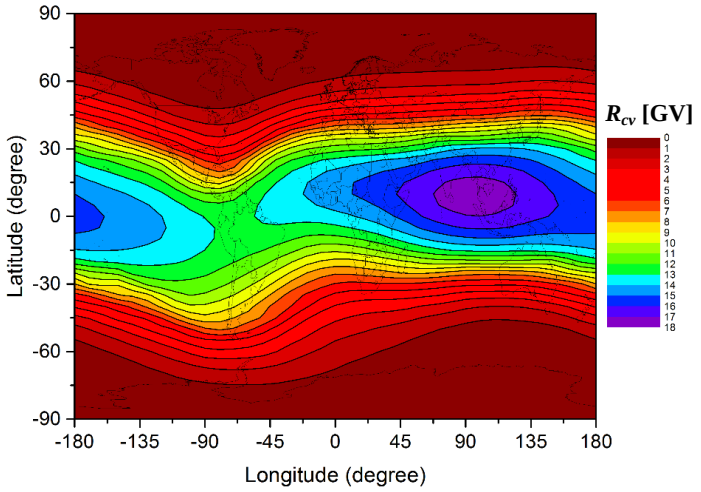

Figure 4: Vertical Cutoff Rigidity R_{cv} (data from [8])

Figure 4 shows a world map of vertical cutoff rigidities that were calculated by D.F. Smart and M.A. Shea [8]. The distribution of high and low rigidity values also shows a longitude dependence, because the dipole axis and the axis of rotation are not perfectly aligned. The dipole axis is somehow shifted so that it does not intersect Earth's centre of mass. Because of that, the cutoff rigidities are not perfectly symmetric along the prime meridian. The vertical cutoff rigidity significantly influences the radiation exposure at flight altitudes. This dependence was demonstrated by in-flight measurements of the radiation exposure at Aalborg ($57° N$; $R_{CV} = 1.8$ GV) and Rome ($42° N$; $R_{CV} = 6.4$ GV), where the results show far lower dose rates at the location with the higher cutoff rigidity [9]. For more details on how the vertical cutoff rigidity is considered in the calculation of the primary proton spectra, refer to section 3.3.2 on page 30.

2.3 Ground level neutron monitor

A neutron monitor is a measuring device that indirectly determines the cosmic ray flux arriving at Earth by measuring the amount of high energy nucleons on the ground. These nucleons are part of the secondary cosmic radiation that was produced by primary cosmic radiation high up in the atmosphere. When the secondary nucleons hit the material of the neutron monitor, nuclear interactions take place, which produce neutrons. These neutrons are measured by the neutron monitor, hence the name [10]. For more details regarding the working principle of a neutron monitor, see section 2.3.1.

A neutron monitor cannot give exact information on the energy distribution of the primary particles, but it does provide a very good knowledge of the current solar activity and the intensity of solar particle events. Most of the time, a neutron monitor only "sees" the galactic cosmic radiation that is anti-correlated to the sunspot cycle. Figure 2 shows this anti-correlation very well. While the activity of the Sun is in its maximum, which leads to a high sunspot number (bottom diagram), the count rate of neutrons on the ground is in its minimum, which corresponds to a low flux of galactic cosmic rays (top diagram). This is due to the shielding effect described in section 2.1.1.

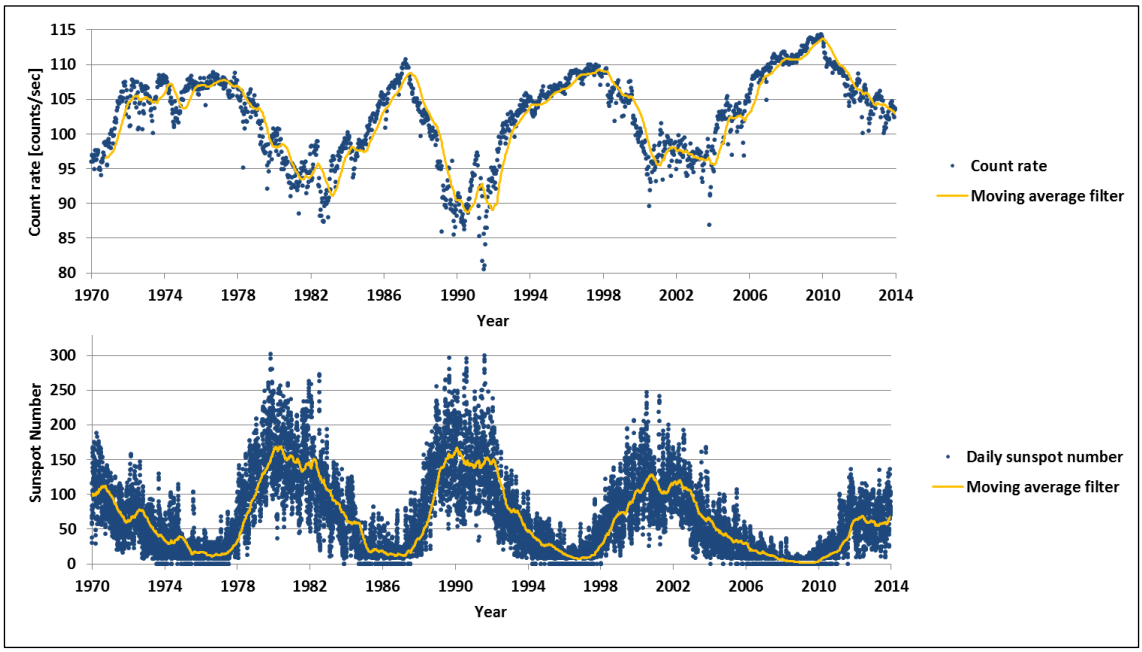

Figure 5: Top – Count rate of neutrons (data from OULU cosmic ray station); Bottom – Daily sunspot number (data from [4])

Due to the fact that the count rate induced by the galactic cosmic radiation only varies in the course of several years, it is obvious that short-term variations (so-called ground level enhancements; see Table 1) must be the result of solar particle events. The intensity of such an event is given by the increase of neutron count rate compared to the pre-increase average. Figure 6 (top) shows this increase during GLE42 on 29th of September 1989. Within only several hours, the count rate climbed to almost twice its original value. The whole event lasted about 12 hours.

In some cases, the count rate decreases after the SPE to values lower than the count rate prior to the event and later on recovers to its original value within a couple of days (see Figure 6, bottom). This effect is called *Forbush Decrease* [1]. The underlying mechanism is thought to be the shielding effect of the magnetized plasma cloud, which reduces the flux of GCR particles. [1] Flight measurements performed in 2003 have shown, that the cosmic radiation exposure in aircrafts decrease during such Forbush events [11]. The impact of these solar events on the radiation exposure on flight altitudes is investigated in chapter 5 and 6.

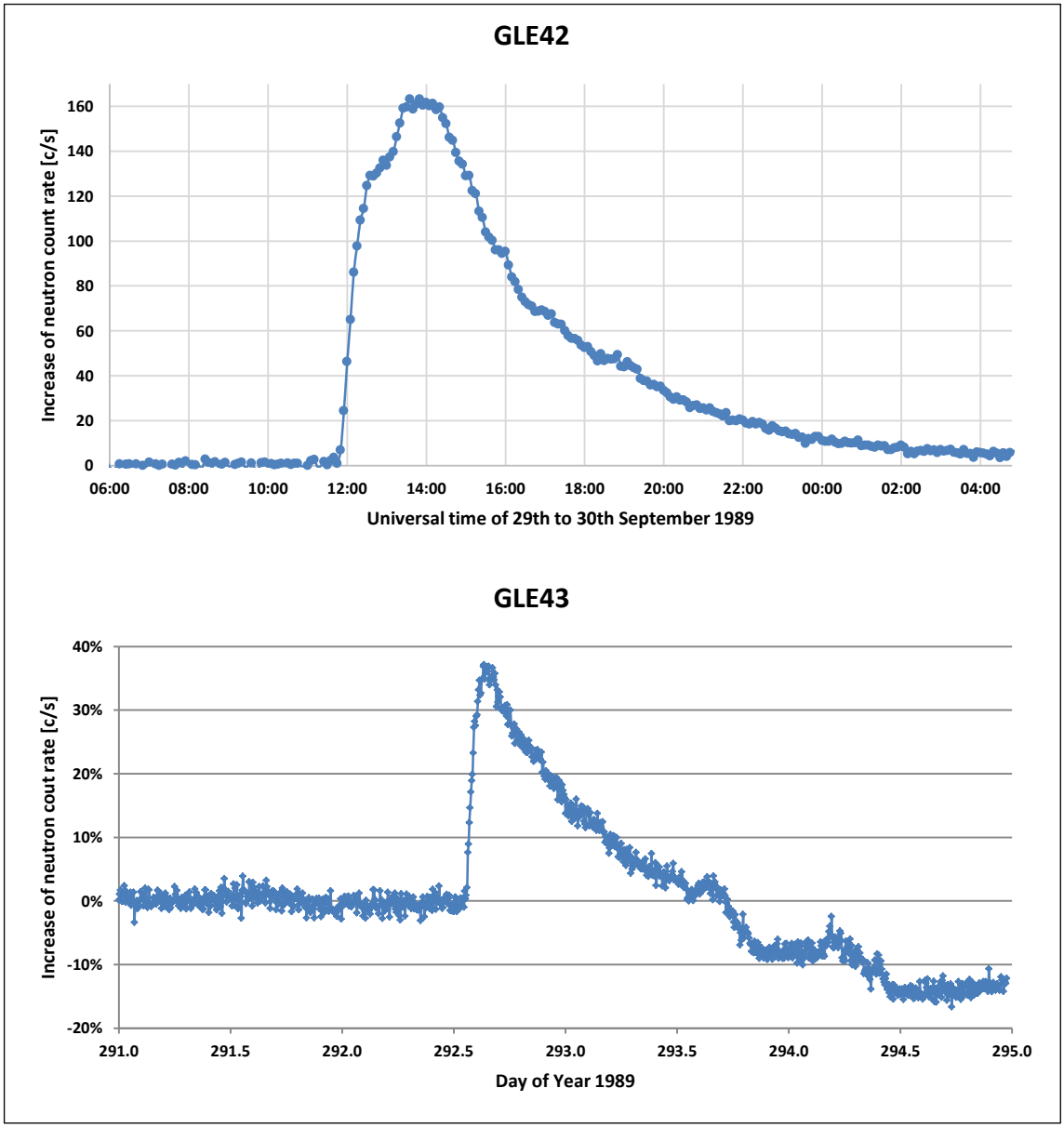

Figure 6: Percentage increase of neutron count rate during GLE42 on 29th of September 1989 (top) and GLE43 on 19th of October 1989 (bottom) (data from OULU cosmic ray station)

2.3.1 Setup and working principle of a neutron monitor

A neutron monitor consists of special gasfilled *proportional counters*, which are surrounded by a *moderator*, a *neutron producer* made from lead, and a *reflector*. The incident protons and neutrons from the secondary cosmic radiation hit the lead shielding, leading to nuclear interactions that result in free neutrons. In order to increase the probability of interactions with the gas in the proportional counters, the neutrons are decelerated down to thermal energies. This is done by the moderator, which is typically made of polyethylene or paraffin. [10]

The proportional counters are filled with either BF_3 or ^3He gas. The thermal neutrons entering the counter tubes are detected via the reaction products of one of the following exothermic reactions: [10]

$$^{10}_{5}B + n \rightarrow ^{7}_{3}Li + ^{4}_{2}He \tag{4}$$

$$^{3}He + n \rightarrow ^{3}_{1}H + p \tag{5}$$

The whole setup including the counter, moderator and lead producer is additionally incased by the reflector, which is also made of moderator material. This material reflects the neutrons produced in the lead back into the proportional counters. It also shields the monitor from neutrons that are produced in the material surrounding the detector, such as the detector housing. This ensures, that changes of the surrounding environment cannot influence the detector efficiency. [10]

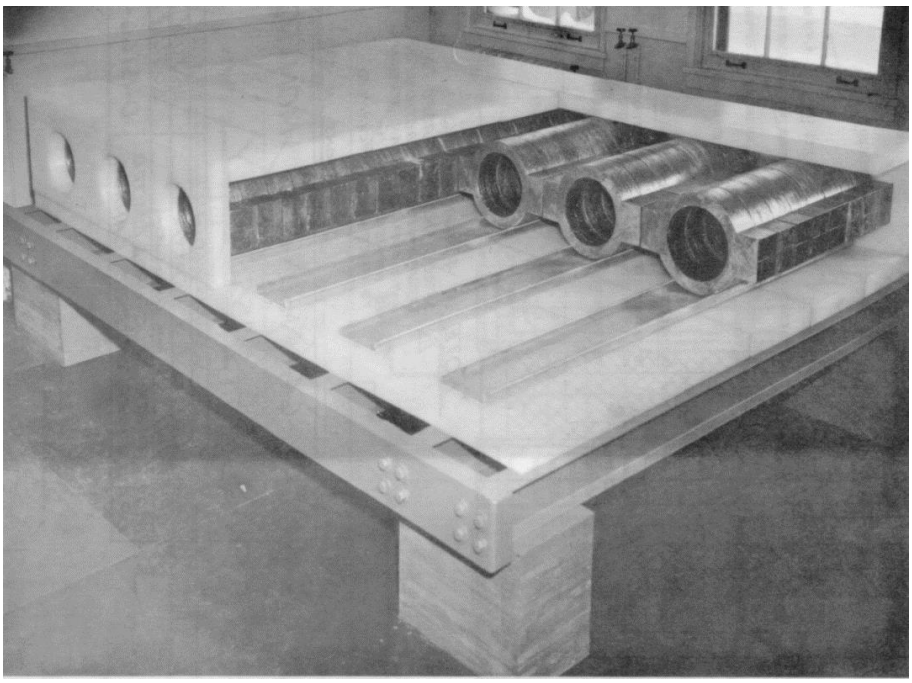

Figure 7: Setup of a neutron monitor; visible is the reflector material and the lead producers [10]

2.4 Interactions with matter

The high-energy collisions between the primary cosmic radiation and the air molecules in the atmosphere lead to a multitude of physical interaction processes, in which the initial energy is transformed into new particles or electromagnetic radiation. The result is a series of alternating interaction processes, a so called *atmospheric shower,* which occurs in the atmosphere until the particle energies are too small to start any further processes. In order to help provide an understanding of the happenings in the atmosphere, the main interaction processes are introduced in section 2.4.1. The atmospheric showers are explained in more detail in section 2.4.2. Additional information regarding the classification and properties of the involved physical particles may be looked up in the appendix starting on page 76.

2.4.1 Interaction processes

All physical processeses are based on one of the four fundamental forces: [12]

- Gravitation
- Electromagnetic interaction
- Strong interaction
- Weak interaction

Every particle is subject to gravity. Gravity plays an important role in the formation of galaxies, stars and planets. In the microscopic range however, it may be ignored, because it is dominated by the other three forces. [12] For this reason, gravity is not considered in the further analysis.

To the *electromagnetic processes* belong processes such as compton and coulomb scattering, the photoelectric effect or the production of Čerencov radiation. However, the most important electromagnetic processes occurring in the atmosphere are *pair production* and the generation of *bremsstrahlung*. If a high-energy electron is decelerated in the coulomb field of an atom, part of its energy is transformed into bremsstrahlung. Pair-production can occur, if a photon has at least twice the energy of the rest energy of an electron (i.e. 1.02 MeV) and passes close to a nucleus. As a result, the photon is converted into an electron and a positron. [1] These two processes are sketched in Figure 8.

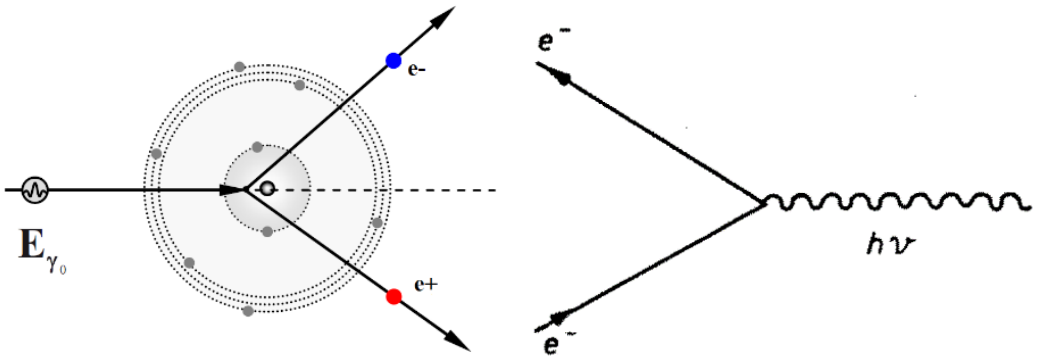

Figure 8: Left: Pair production [13]; Right: Bremsstrahlung [1]

Strong interactions take place when high energy hadrons traverse matter. The result is nuclear interactions inwhich free nucleons, mesons as well as alpha particles and fragments of heavier

nuclei are produced. Along with this, nuclei are raised to excited states and evaporate nucleons and gamma rays. [1]

The *weak interaction* manifests itself in the decay processes of many unstable particles, such as charged pions or myons: [1]

$$\pi^+ \rightarrow \mu^+ + \nu_\mu \tag{6}$$

$$\pi^- \rightarrow \mu^- + \bar{\nu}_\mu \tag{7}$$

$$\mu^+ \rightarrow e^+ + \nu_e + \bar{\nu}_\mu \tag{8}$$

$$\mu^- \rightarrow e^- + \bar{\nu}_e + \nu_\mu \tag{9}$$

The electrically neutral pion however decays via the electromagnetic interaction: [1]

$$\pi^0 \rightarrow 2\gamma \tag{10}$$

2.4.2 Particle showers in the atmosphere of the Earth

If a cosmic ray particle collides with an atmospheric atom or molecule and its energy is high enough, a series of physical processes is initiated, which leads to *particle showers* or *particle cascades.* The two main mechanisms that take place during a particle shower are *electromagnetic cascades* and *hadronic cascades.* [1]

An electromagnetic cascade is carried by photons, electrons and positrons. The two main processes involved are the *pair-production* and the generation of *bremsstrahlung*. If an incoming electron is decelerated by the Coulomb field of an atmospheric atom, part of its energy is converted into bremsstrahlung. If the energy of the produced photon is high enough, it can be converted into an electron-positron pair, as described in the previous section. The sequence can start again from the beginning if the produced electron-positron-pair still has enough energy to produce further bremsstrahlung. In this way, a cascade of alternating photons, electrons and positrons is formed. [1] The procedure is depicted in Figure 9.

A hadronic cascade is carried out by hadrons. An incoming galactic proton hits an atom in the atmosphere and interacts with its nucleus, leading to a multitude of hadronic secondary particles, such as nucleons and mesons. These particles either interact again or decay into further particles. Among these secondary particles, the pion triplet π^0, π^+ and π^- is the most abundant. The neutral pions decay into gamma rays, which in turn can activate electromagnetic cascades. The charged pions either contribute to the hadronic cascade if they get the chance to interact before they decay, or form a muonic component in the atmosphere by decaying into muons and neutrinos via the processes (6) and (7). Most of these muons reach sea level, but some of them decay further into electrons and neutrinos (see process (8) and (9)). [1] This process is sketched in Figure 9.

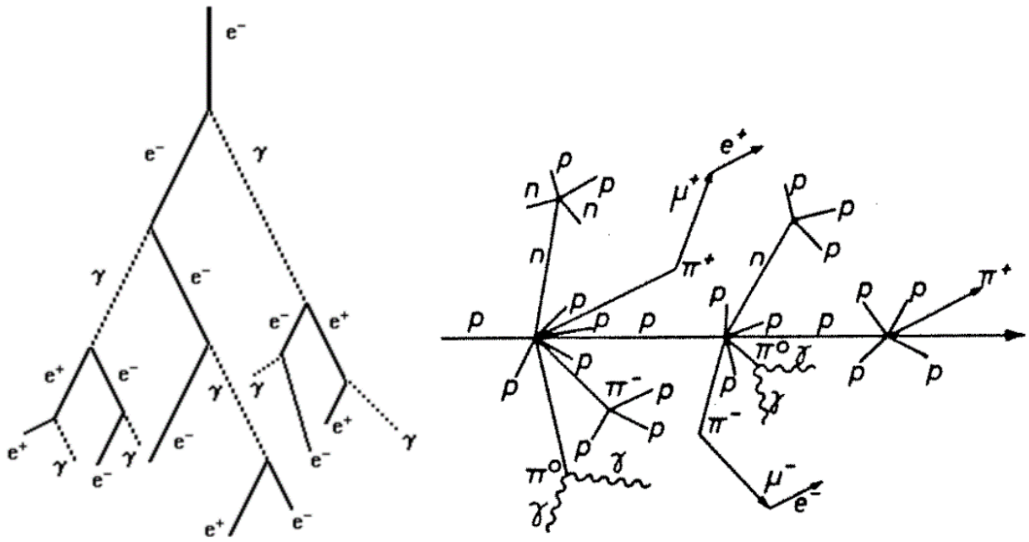

Figure 9: Schematic representation of an electromagnetic cascade (left) [14] and a hadronic cascade (right) [1]

Because of the interplay of recombination processes, absorption and atmospheric densities, there is a distinct maximum in the particle production rate at an altitude of about 20 km. This maximum is called the *Pfotzer Maximum.* [1]

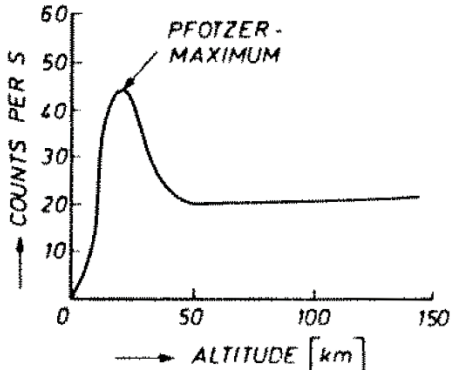

Figure 10: Pfotzer maximum [1]

2.5 Dosimetric quantities

In order to assist in the interpretation of the plots of the following sections, the used dosimetric quantities are briefly explained below.

Energy imparted ϵ

The fundamental dosimetric quantity is the *energy imparted* ϵ. It is the energy, which is built up by ionizing radiation in matter in a volume.

Unit: Joule (J)

$$\epsilon = R_{in} - R_{out} + \sum Q \tag{11}$$

R_{in} is the sum of the energies of all ionizing particles entering the volume. In order to calculate the energy which is imported into the volume, the particle energies of all particles that leave the volume, R_{out}, have to be subtracted. The term $\sum Q$ considers all the changes of rest mass energy. A quantity closely related to the energy imparted is the *absorbed dose* which uses the mean value $\bar{\epsilon}$. [15]

Absorbed Dose D

The *absorbed dose D* defines the deposited energy per unit mass at a certain point in a volume:

Unit: Gy (J kg^{-1})

$$D = \frac{d\bar{\epsilon}}{dm} \tag{12}$$

The energy which is deposited in matter can lead to certain effects which are either proportional to D or are dependent in a more complex way. The unit of this quantity was given a special name, the *Gray*. [16]

Absorbed Dose Rate Ḋ

The *absorbed dose rate* $\dot{D}$ is the deposited energy per unit mass and unit time. [15]

Unit: Gy s^{-1} (J kg^{-1} s^{-1})

$$\dot{D} = \frac{dD}{dt} \tag{13}$$

Linear Energy Transfer L

A particle travelling through a material will lose some of its energy due to collisions with other particles. This loss can either be built up in the material or it can escape, e.g. in form of bremsstrahlung. The *linear energy transfer* (also called linear collision stopping power) is the amount of energy deposited along the particle track, therefore excluding the bremsstrahlung, which can travel a long way before it is absorbed. This quantity is directly proportional to the damage in biological tissue. [15] [17]

Unit: J m^{-1}

$$L = \frac{dE}{dl} \tag{14}$$

Lineal Energy y

The *lineal energy* is similar to the linear energy transfer, but in contrast to this, it is a stochastic quantity. It is defined as the energy imparted of a single energy-deposition event divided by the mean chord length $\bar{l}$ in the considered volume. [15]

Unit: J m^{-1}

$$y = \frac{\epsilon}{\bar{l}} \tag{15}$$

Dose Equivalent H

Not every type of radiation has the same damaging effect on biological tissue. Different ionizing particles may deposit the same amount of energy yet vary in the severity of their impact on organisms. Electrons for instance are less damaging than heavy particles, such as protons, neutrons or alpha particles. Therefore, a dimensionless quality factor *Q* has been introduced to weight the absorbed dose so that different kinds of radiation may more easily be compared. [17]

Unit: Sv (J kg^{-1})

$$H = Q \cdot D \tag{16}$$

The unit for this quantity was given a special name, the *Sievert* (Sv). The quality factor depends on the Linear Energy Transfer *L* in the following way:

Table 2: Quality factor depending on L [17]

$L(keV/\mu m)$	$Q(L)$
< 10	1
$10 - 100$	$0.32 \cdot L - 2.2$
> 100	$300/\sqrt{L}$

Dose Equivalent Rate Ḣ

The *Dose Equivalent Rate* is the weighted absorbed dose per unit time. [15]

Unit: Sv s^{-1} (J kg^{-1} s^{-1})

$$\dot{H} = \frac{dH}{dt} \tag{17}$$

Ambient Dose Equivalent $H^*(d)$

The *Ambient Dose Equivalent* is a quantity which was defined for practical measurements. It is the Dose Equivalent that would result due to an aligned radiation field at a certain point in the ICRU sphere[1] at a depth *d,* where *d* is measured along a radius facing the source of radiation. For strongly penetrating radiations a depth of 10 mm is used. This quantity is denoted by *H*(10)* and has the unit Sievert. [17]

[1] The ICRU sphere a 30 cm diameter tissue-equivalent sphere with a density of 1 g cm-3 and a mass composition of 76.2 % oxygen, 11.1 % carbon, 10.1 % hydrogen and 2.6 % nitrogen. [13]

Equivalent Dose H_T

The *Equivalent Dose* H_T is similar to the Dose Equivalent H, however it is not a point quantity but an average over a tissue or a whole organ. It is calculated from the Absorbed Dose $D_{T,R}$, averaged over a tissue or organ and multiplied by a radiation weighting factor w_R (see Table 3). [17]

$$H_{T,R} = w_R \cdot D_{T,R} \tag{18}$$

If the radiation is not uniform but consists of a mix of radiations, then the total Equivalent Dose H_T is given by the sum over all radiation components. [17]

$$H_T = \sum_R H_{T,R} = \sum_R w_R \cdot D_{T,R} \tag{19}$$

Table 3: Radiation weighting factor [18]

Radiation Type	Radiation Weighting Factor w_R
Photons	1
Electrons, Positrons, Muons	1
Neutrons E > 10 keV	5
10 – 100 keV	10
0.1 – 2 MeV	20
2 – 20 MeV	10
E > 20 MeV	5
Protons	5
Alpha particles, heavy nuclei, fission fragments	20

Effective Dose E

Not every tissue or organ is equally sensitive to ionizing radiation. Human skin for instance is less vulnerable than the human lung. Therefore the Equivalent Dose, which takes into account the radiation type, is additionally weighted by a tissue weighting factor, see Table 4. [17]

$$E = \sum_T w_T \cdot H_T \tag{20}$$

Table 4: Tissue weighting factor [19]

Tissue / Organ	w_T - factor
Lung, Red Bone Marrow, Breast, Colon, Stomach	0.12
Gonads	0.08
Thyroid, Bladder, Liver, Oesophagus	0.04
Bone Surface, Skin, Brain, Salivary glands	0.01
Rest	0.12

2.6 Tissue equivalent proportional counter (TEPC)

The *Tissue Equivalent Proportional Counter (TEPC)* is a powerful tool in dosimetry to determine the distribution of linear energy transfer (LET) of secondary particles. This quantity is directly proportional to the damage caused to biological tissue (see section 2.5). The TEPC is a special type of proportional counter, built in such a way, that the experimental setup simulates the energy deposition processes taking place in a human cell. [20]

The size of a human cell lies in the micrometre range. Determining the energy deposition processes in volumes of these dimensions would be very elaborate, which is why another approach is taken. The experiment is not conducted in the microscopic, but in the macroscopic range. In return, the density is reduced so that the interactions do not take place in a solid medium, but in a gaseous medium instead. For the chamber wall and the filling gas, a composition is chosen that resembles the composition of human tissue. The aim is to achieve an experimental setup, in which the same processes occur, as in a human cell, only on larger scales. Nevertheless, the effective dimensions (e.g. equal products of diameter and density) [20] must stay the same. This allows for two major advantages.. For one thing, the geometrical magnification leads to an enhanced interaction probability with the volume. For another thing, the gas multiplication[2] in the proportional counter makes the detection of even a few ionizations possible. Therefore, the signal-to-noise ratio is very good. [17] [20]

2.6.1 TEPC "HAWK"

In this work, a TEPC with the model name "HAWK" is used to measure the effects of cosmic radiation during a test flights in Zeltweg (Austria). The detector was manufactured by *Far West Technology*. Its chamber is spherical with a diameter of 12.7 cm and it is filled with propane gas under a very low pressure of 933.2 Pa. The 0.21 cm thick sphere is made of A150 conducting tissue equivalent plastic. [21] This combination of tissue equivalent plastic and propane gas is designed to mimic the elemental composition of human tissue of a volume 2 µm in diameter [22]. The acceleration voltage is applied between the sphere (cathode) and a thin wire (anode), which passes through the sphere. Attached to the detector sphere is an instrumentation package that analyses and stores the measured data. The setup is sketched in Figure 11.

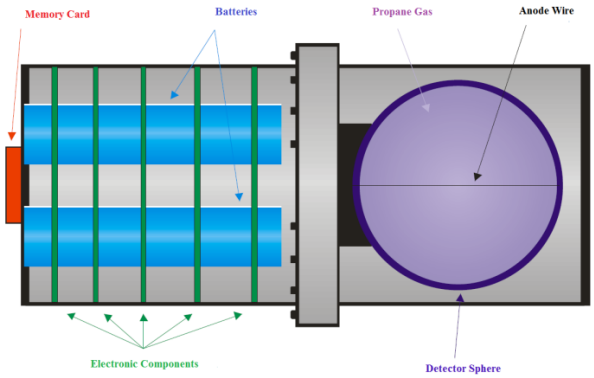

Figure 11: Sketch of the TEPC "HAWK" [23]

Every ionization event in the chamber leads to a charge pulse whose amplitude depends on the LET of the particle and the path length it travels in the gas. [17] A pre-amplifier and a shaping-amplifier amplify this signal and following this, two Multi-Channel Analysers convert the analogue signal into a digital signal. There are two channels, one for high-gain and one for low-

[2] e.g. amplification of the signal due to the avalanche effect caused by acceleration of the original ion pairs in the electric field of the proportional counter [15]

gain. The low-gain channel is a 10 bit analogue to digital converter covering the range from 0 to 1024 keV/µm. In addition, the high-gain 8 bit analogue to digital converter improves the resolution in the low LET range from 0 to 25.6 keV/µm. [21] The measured distribution of absorbed dose as a function of lineal energy is converted to dose equivalent by folding the distribution with the quality factor Q (Table 2), which is a function of linear energy transfer (LET) [11]. In order to obtain the result in the unit ambient dose equivalent, the dose equivalent has to be multiplied by calibration factors for the low- and high-LET range [11].

2.6.2 Microdosimetric spectra

The TEPC not only allows to determine the total dose rates, but also the distribution of energy deposition events with respect to their lineal energy y (see equation (15)). This distribution is depicted in the form of *microdosimetric spectra.* This section explaines how to develop a microdosimetric spectrum from the output of the TEPC as well as what information one can gain from it.

The typical output of a TEPC measurement is depicted in Figure 12. It shows the number of events that occurred within an interval of lineal energy summed up over a certain period of time. From this, the probability distribution $f(y)$ may be calculated, see Figure 13. The likelihood, that an energy deposition event has a lineal energy in the interval $[y, y + dy]$ is given by $f(y)\, dy$ [20].

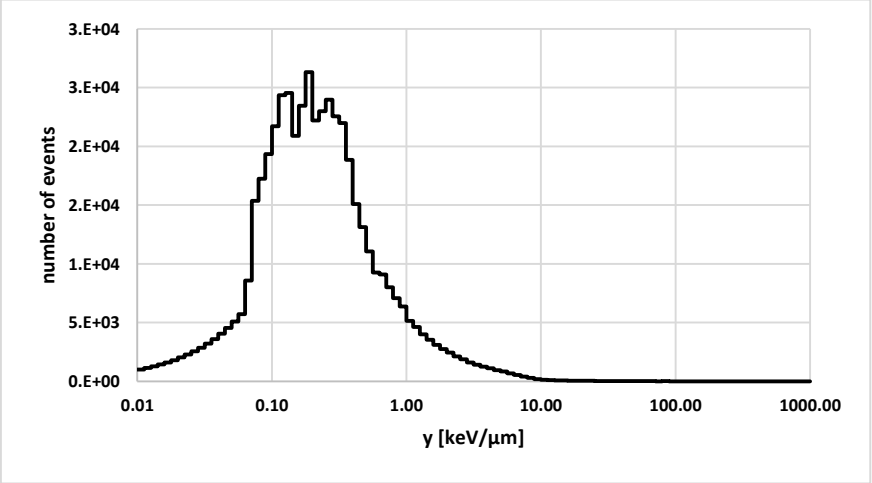

Figure 12: Typical output of a TEPC measurement

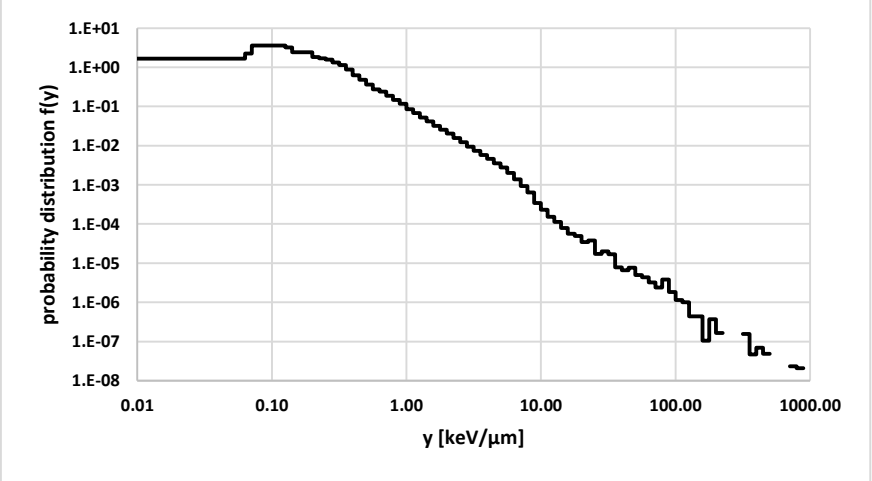

Figure 13: Probability distribution of events

Microdosimetric spectra are usually displayed in a $y\,f(y)$ versus y representaion, where y is plotted logarithmically. This increases the readability of the spectra, because the area limited by any two values of y is directly proportional to the fraction of events that happened in the chosen interval [20]. This is true because of the following relation: [20]

$$\int_{y_1}^{y_2} f(y)dy = \int_{y_1}^{y_2} [yf(y)]d\log(y) \tag{21}$$

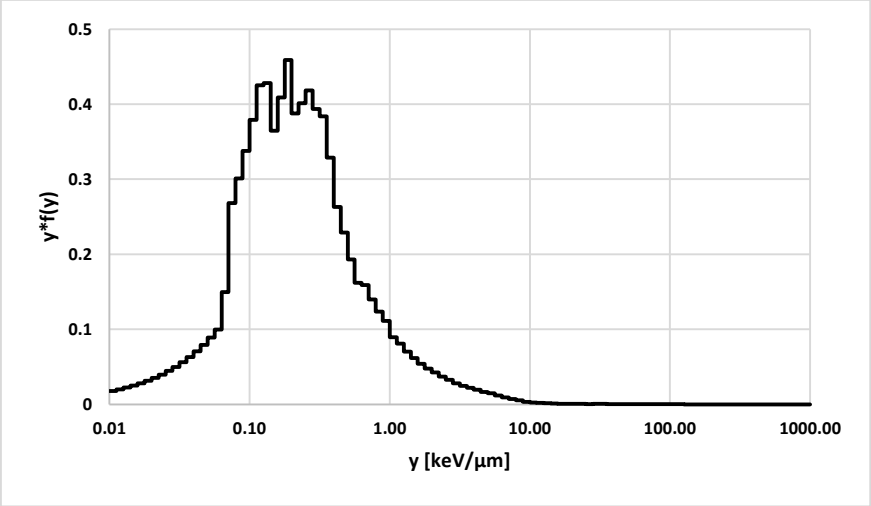

Figure 14: Probability distribution multiplied by y

The quantity $y\,f(y)$ is defined as the dose distribution $d(y)$, which is again plotted as described above, thus $y\,d(y) = y^2\,f(y)$ versus y on a logarithmic scale. Any area limited by two values of lineal energy represents the fraction of absorbed dose caused by events with lineal energy values within the chosen interval. [20]

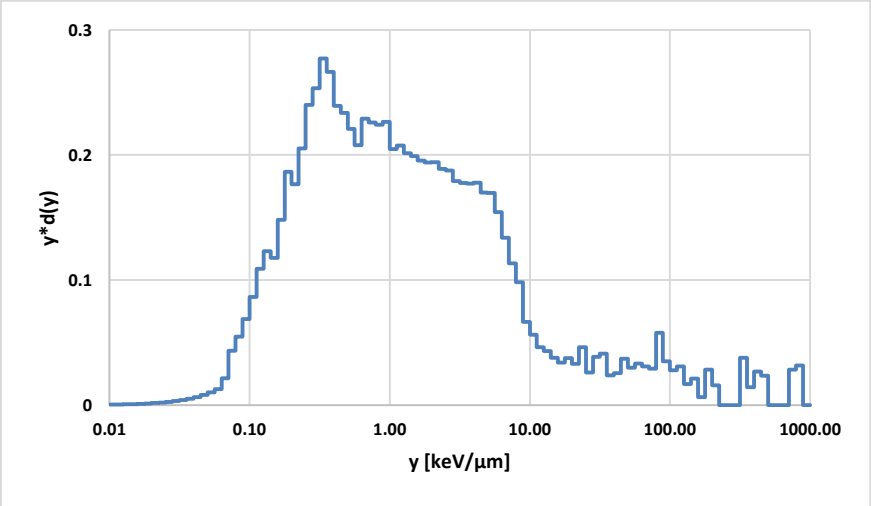

Figure 15: Dose distribution multiplied by y

The distribution of dose equivalents is gained by multiplying the dose distribution from above by the quality factor Q listed in Table 2, thus $h(y) = Q \cdot d(y) = y \cdot Q \cdot f(y)$. [20] The result is depicted in Figure 16. Again, enclosed areas represent the fractions of dose equivalents produced by events with lineal energy in the respective range. By comparing the distributions of $d(y)$ and $h(y)$ it becomes apparent, which ranges of lineal energy are important for the

biological effectiveness. Even though only a small fraction of the absorbed dose is produced by high LET events, these are the ones with the highest damaging effect on human tissue.

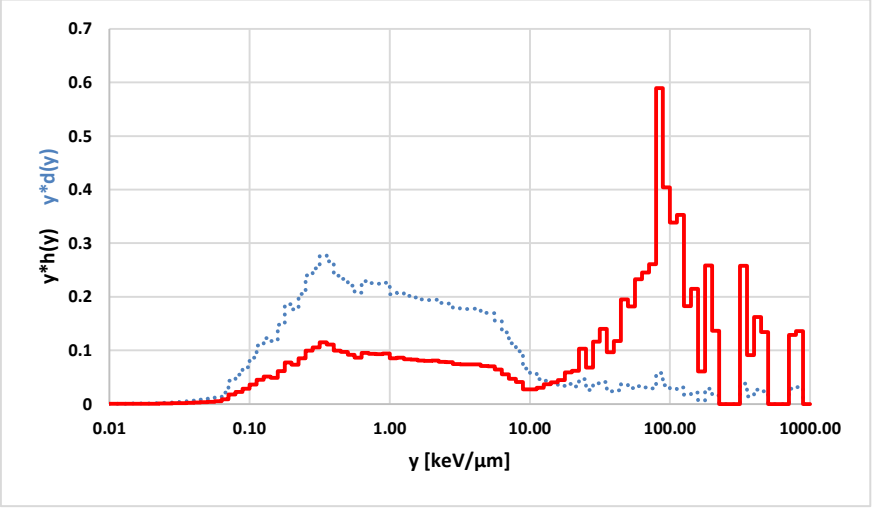

Figure 16: Distribution of dose equivalent multiplied by y; For comparison of biological effectivness, the dose distribution is represented by the dashed line

The normalisation of microdosimetric spectra is an important aspect. When developing microdosimetric spectra, the logarithmic y-axis is divided into intervals with a fixed number of increments per decade. Let B be the number of increments per decade, then the plots are normalized so that the following equations hold: [24]

$$\frac{\ln 10}{B}\sum_{i=1}^{\infty} y_i\, f(y_i) = 1 \tag{22}$$

$$\frac{\ln 10}{B}\sum_{i=1}^{\infty} y_i\, d(y_i) = 1 \tag{23}$$

$$\frac{\ln 10}{B}\sum_{i=1}^{\infty} y_i\, h(y_i) = 1 \tag{24}$$

2.7 Simulation methods and tools

All simulations in this work were computed by the *PLANETOCOSMICS* code. This code is based on the *GEANT4* particle transport toolkit, which makes use of the *Monte Carlo method* to obtain its results. Section 2.7.1 illustrates the basic idea behind this simulation technique. Additionally, the most important characteristics of GEANT4 and its application PLANETOCOSMICS are outlined in section 2.7.2 and 2.7.3.

2.7.1 Monte Carlo Method

The Monte Carlo method is a very powerful technique to solve problems in physics, mathematics and several other fields that would be too complex to solve analytically. Some examples include the simulation of radiation passing through matter, processes that involve thermal motion or high dimensional integrals [25]. Here, the number of input variables is extremely large, which makes an analytical solution unfeasible. The Monte Carlo method is a

way to solve these problems numerically by making use of random numbers that serve as input variables for the considered problem.

The starting point for a Monte Carlo Simulation is a mathematical model that describes a physical process. This process depends on a certain amount of input parameters that result, after the evaluation of the mathematical formulas, in a certain amount of output parameters. The basic approach of any MC simulation is to assign a probability distribution to every input parameter. These distributions are modelled according to their underlying physics. Following this a random variable is drawn from each distribution, leading to a unique set of input parameters for the mathematical model. After the calculation of the results, a new set of random parameters is sampled and the results are re-calculated. This process is repeated many times. Consequently, there is not only one outcome of the simulation but many outcomes of many simulation runs. The end result is a distribution of many possible outcomes, rather than the one predicted outcome that a deterministic model would deliver. These outcomes are collected and averaged to form an estimate of the quantity of interest.

The quality of the result of an MC simulation depends heavily on the amount of simulation runs. The higher the number of runs, the more histories are collected and the more accurate the mean of the distribution of outcomes. This is a direct consequence of the law of large numbers, formulated by Jacob Bernoulli in 1689. It states, that the mean value of samples of a distribution approaches the true population mean as the number of samples gets large [26].

$$\lim_{N\to\infty} \bar{x} = \langle x \rangle \tag{25}$$

In other words, the solution of a MC simulation is always further improvable by increasing the number of iterations. Unfortunately, this also results in an increase of calculation time. Therefore, a good compromise of those two competing factors has to be found.

[25 - 28]

2.7.2 GEANT4 C++ Toolkit

The backbone of the simulation software used in this work is GEANT4 (short for **Ge**ometry **an**d **T**racking). It is a toolkit designed for the simulation of interaction processes and particle transport in matter that is developed and maintained by a worldwide collaboration. The main contributors are CERN and ESA. The program is written in the object-oriented programming code C++ and makes use of the MC method to take account of the huge amount of possible particle interactions. [29 - 31]

The simulations conducted in the course of this master thesis were performed by Planetocosmics, an application that accesses the large variety of physical models implemented in GEANT4. Among them are models that describe electromagnetic processes, hadronic processes, decay processes and many more [27]. However, the validity of each of these models is limited to specific particle families and energy ranges. The reason there is not a 'default mode' that contains a complete set of physical models is the fact, that no application requires all the physical processes that GEANT4 has to offer. The calculation time of a simulation is a crucial factor, which makes it necessary to apply approximations and to neglect all unnecessary processes. This implies that the user has to choose appropriate models that match the considered problem without exceeding its limits of applicability. Therefore, GEANT4 combines several models to so-called "physics lists" that are significant for a certain type of application. If these predefined physics lists do not fulfil the user's wishes, it is possible to add or alter some models. [27]

The GEANT4 physics models are highly complex. A detailed description of all physics lists is not the aim of this work. However, the following paragraphs give a short description of the physics list used for the simulations in this work.

2.7.2.1 Physics lists

The main physics list used for the calculations in this work is *QGSP_BERT_HP*. This stands for [27]:

QGS ..... *Quark Gluon String model*

P ..... *G4Precompound model (used for de-excitation)*

BERT .... *Bertini-style cascade*

HP ..... *High Precision neutron model*

The QGSP part of the physics list handles the hadronic high-energy collisions between protons, neutrons, pions and kaons and nuclei, by applying the *Quark Gluon String model*. The end result of such a collision is a highly excited remnant nucleus, which is then passed on to the *G4Precompound model* that models its de-excitation. The QGSP model can be applied for incident nucleons, pions and kaons in the energy range of 12 GeV to 100 TeV. [28] For interactions below this energy range the *Bertini style cascade* becomes effective, which generates the final state for hadron inelastic scattering. Here, incident hadrons collide with nucleons in the target nuclei, which results in a particle cascade inside the nucleus. The model is valid in the energy range from 0 to 10 GeV. [29] The last part of the physics list is the *High Precision Neutron model* that provides more accurate results for neutrons with energies below 20 MeV [30].

The QGSP component already contains a "standard" physics list for electromagnetic processes. To the standard electromagnetic physics list belong models that describe the multiple scattering of electrons and muons, the generation of bremsstrahlung and the photo-electric effect [31]. In this work an additional electromagnetic physics list with the name *Livermore* is used, which extends the coverage of electromagnetic interactions to lower energies. Furthermore it adds supplementary low energy processes for photons, electrons, hadrons and ions. These include the photo-electric effect, Compton scattering, Rayleigh scattering, gamma conversion, bremsstrahlung and ionization. More importantly it considers atomic de-excitation in terms of fluorescence and Auger electron emission. [32]

2.7.3 Planetocosmics GEANT4 Application

Planetocosmics is a GEANT4 application focusing on the interaction of cosmic radiation with the planets Mercury, Earth and Mars. In this case it is possible to consider the magnetic field, the atmosphere and the soil. It is constructed in such a way that the implementation of additional planets or moons is fairly simple. [33]

In this work *Planetocosmics* was used to build a computer model that simulates the effects of cosmic radiation impinging on the atmosphere. The results were particle fluxes for various particle species at user defined altitudes. In a later step these fluxes were used to determine the effective dose E and the ambient dose equivalent $H^*(10)$. For more information on the Planetocosmics simulation model see section 3.1.

Above that the program can be used for additional applications such as: [33]

- The study of quasi trapped particle population
- The computation of cutoff rigidity
- The visualisation of magnetic field lines

3 Modelling of radiation exposure at flight altitudes

This chapter describes the general structure of the simulation model for the dose calculations as well as its further processing into a user-friendly program. The aim is a tool that can be used to easily and quickly estimate the radiation dose at a user defined coordinate and altitude on Earth. Most important is the altitude range from the surface to a height of about 20 km, since the majority of the public and military air traffic takes place in this range. The model has to take a multitude of parameters into consideration. The radiation doses depend on the altitude due to atmospheric shielding and on the geographical position due to magnetic shielding. In addition, the solar activity has to be considered. This includes the 11-year periodicity of the GCR flux and also solar particle events, as described in section 2.1. The output parameters of the model are the *ambient dose equivalent rate* $dH^*(10)/dt$ and the *effective dose rate* dE/dt (cf. section 2.5).

Another important requirement for the model is its flexibility to changes in the proton input spectrum. The proton input spectrum stretches over several orders of magnitude in energy, which is why the simulation run for a whole spectrum demands a considerable amount of time. Therefore, it would be impractical if the simulation results would have to be recalculated over and over again, every time the input spectrum is modified. A quick estimation of the radiation dose would be impossible. This is why the simulation tool consists of two parts: The first is the *Planetocosmics* simulation model, which simulates the physical effects and results for a certain input spectrum in particle fluxes at user defined altitudes (see section 3.1). However, the input for the simulation model is not the whole energy range of the spectrum but only small intervals with identical fluxes. The resulting particle fluxes for every energy interval are stored in a huge matrix, which makes up the second part of the model. This matrix depends on energy and altitude. In a later step, these partial results have to be weighted by the true spectrum and combined to yield the final result. This procedure makes the simulation model independent of the primary input spectrum, hence fast and even realtime dose calculations are possible. This plays an important role in the assessment of solar events, where the spectra change very rapidly. Section 3.2 explaines this procedure in more detail.

Figure 17 shows a flowchart of the input and output parameters of the model.

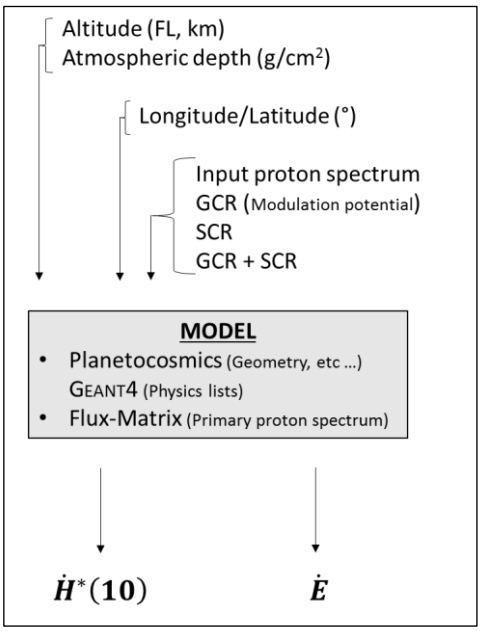

Figure 17: Flowchart of input and output parameters of the model

3.1 Planetocosmics simulation model

The *Planetocosmics* simulation model consists of the four main sections named:

- GEOMETRY
- PHYSICS
- ANALYSIS AND HISTOGRAMMING
- SOURCE

The *GEOMETRY* part defines the setup and the structure of the simulated environment. It sets the dimensions and properties of the core, the soil, the atmosphere and also the empty space surrounding the planet. The environment is built up by successive flat layers with its respective properties. Furthermore, it defines the positions of the detectors that measure the generated particle fluxes during the simulaton. The bottom layer of the model is a core with a thickness of 1 km, which absorbes all particles that manage to penetrate down to this level. The layer on top of that is a 10 m thick slab of SiO_2 with a density of 1.7 g / cm^3, which represents the soil of the Earth. Above the soil follows a 100 km thick layer of atmosphere. Density, atmospheric depth, temperature and composition profiles versus altitude as a function of geographic latitude and longitude are offered by the *NRLMSISE00* atmospheric model that is already implemented in *Planetocosmics.* 174 detectors are positioned within the atmospheric layer, nine in the upper range from 25 km to 100 km and 165 in the lower range from the ground to an altitude of 25 km. Additionally, one detector is positioned at an altitude of 100.01 km, outside of the atmosphere, just below the primary particle source. The geometrical setup of the model is sketched in Figure 18.

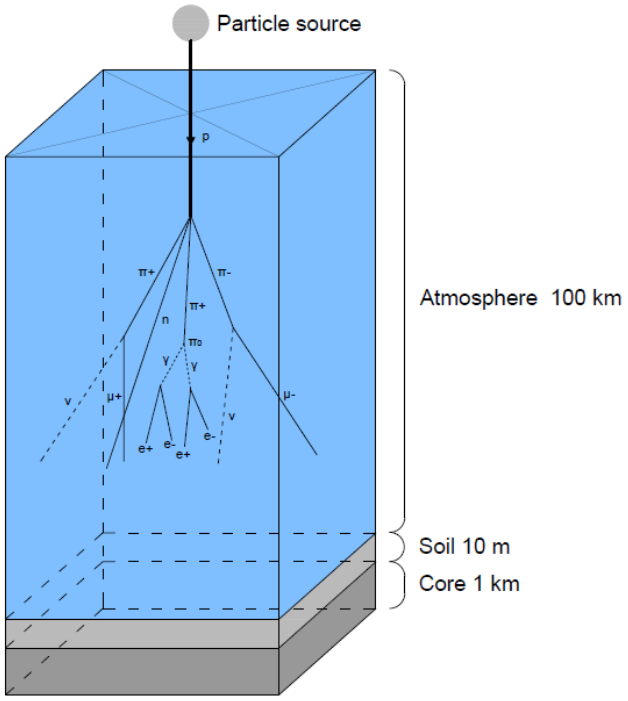

Figure 18: Geometrical setup of the *Planetocosmics* model (not to scale) with a possible particle shower

The *primary particle source* is positioned on top of the atmospheric layer at an altitude of 100.02 km. More information regarding the particle input for the model as well as the shape of the GCR and SCR spectra is given in section 3.3.1.

The *analysis and histogramming* tool implemented in *Planetocosmics* computes the upward and downward fluxes for primary and secondary particles at every detector altitude. The following particles are considered: protons (p), electrons (e^-, e^+), muons (μ^-, μ^+), pions (π^-, π^+), photons (γ) and neutrons (n). The output fluxes are given in $[particles/(cm^2 \cdot s)]$.

The *PHYSICS* section defines, which GEANT4 physics lists are used for the physical processes in the model. The model in this work uses the physics list *QGSP_BERT_HP* for the hadronic interactions and the *Livermore* physics list for the electromagnetic interactions. More information on these physics lists is given in section 2.7.2.1.

Even though *Planetocosmics* allows to consider the magnetic field in its calculation, this feature was disabled during the simulations. The magnetic field only comes into play during the

calculation of the input spectra, where the low-energy range is cut according to the cutoff rigidity at the point of incident. This procedure is described in section 3.3.2.

3.2 Flux-Matrix

As described at the beginning of this chapter, the flux-matrix is used to store and handle the output fluxes of the *Planetocosmics* simulations, which depend on altitude and energy. The energy range of the primary proton spectrum stretches from 10^{-1} MeV / proton to 10^{7} MeV / proton, therefore covering 8 orders of magnitude. The spectrum is divided into intervals on a logarithmic scale with 7 energy intervals per decade, leading to 56 energy segments in total. Each interval serves as input for a *Planetocosmics* simulation with a unitary proton flux of $1\ [\mathrm{particle}/(\mathrm{cm}^2\ \mathrm{s})]$. During the MC calculation of a simulation, the input proton energies are sampled from this interval. This procedure leads for each of the 56 energy intervals to particle fluxes for the previously mentioned particles at the defined detector altitudes.

In the next step, these fluxes are converted into dose rates (*ambient dose equivalent rate* and *effective dose rate*) using fluence-to-dose conversion coefficients [34] and added up along the different kinds of particles. This is done for every energy interval. The final (partial) result for an energy interval are dose rates dependent on altitude that were produced by a unitary proton flux from this energy interval. These partial results are stored in the flux-matrix, which is now a function of energy and altitude. However, the true proton spectrum has still not been considered.

The flux-matrix now contains all information that is needed to compute the final dose rates. Since every entry in the matrix originates from a unitary proton flux, the entries simply have to be weighted by the real proton flux of the respective energy interval. As this is a simple multiplication, this step is done in a very short time. In order to obtain the final result, all energy intervals have to be combined, leading to final dose rates for every detector altitude.

The above illustrated technique has a major advantage. Once the results for all energy intervals are calculated (which only has to be done once), the determination of the dose rates with any proton spectrum is possible within seconds, no matter if it is a GCR or a SCR spectrum. This procedure is sketched in Table 5.

Table 5: Simplified procedure of dose calculation implementing 56 energy intervals

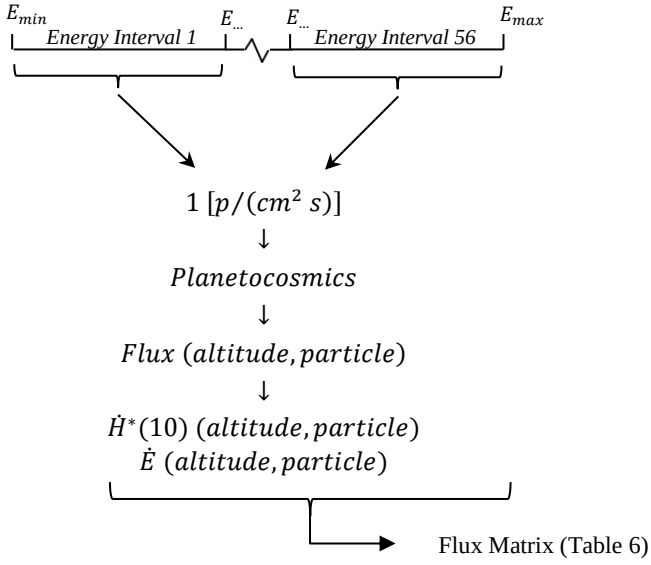

Table 6: Flux matrix

		Altitude →		
Energy ↓	$p - Flux$	$0\ km$	$\cdots$	$100\ km$
$Interval\ 1$	f_{E_1}	$\dot{H}^*_{E_1,H_1}(10) \cdot f_{E_1}$ $\dot{E}_{E_1,H_1} \cdot f_{E_1}$	$\cdots$	$\dot{H}^*_{E_1,H_{174}}(10) \cdot f_{E_1}$ $\dot{E}_{E_1,H_{174}} \cdot f_{E_1}$
$\vdots$	$\vdots$	$\vdots$		$\vdots$
$Interval\ 56$	$f_{E_{56}}$	$\dot{H}^*_{E_{56},H_1}(10) \cdot f_{E_{56}}$ $\dot{E}_{E_{56},H_1} \cdot f_{E_{56}}$	$\cdots$	$\dot{H}^*_{E_{56},H_{174}}(10) \cdot f_{E_{56}}$ $\dot{E}_{E_{56},H_{174}} \cdot f_{E_{56}}$
	$\sum_{Interval\ 1}^{Interval\ 56}$	$\dot{H}^*_{0\ km}(10)$ $\dot{E}_{0\ km}$	$\cdots$	$\dot{H}^*_{100\ km}(10)$ $\dot{E}_{100\ km}$

3.3 Input parameters

The radiation exposure in the atmosphere depends on several factors that have to be considered by the simulation model. The main input parameters are the proton spectrum, the geographical position and the altitude, which is sketched in Figure 17. This chapter describes how these dependencies are taken account of.

3.3.1 Proton spectra

The proton spectrum for the input of the simulation model is a key element, since it triggers the dose production. This section explaines, how the GCR and SCR spectra are modelled, which later on weight the entries of the Flux-matrix.

3.3.1.1 Construction of the GCR proton spectrum

A neutron monitor indirecty measures the galactic cosmic ray flux arriving at Earth (cf. section 2.3). However, it only gives information on the energy integrated flux, while it tells nothing about its energy distribution. Even though energy spectra of cosmic radiation have been measured by balloon flights and space missions, these cannot be used in this work since the shape of the spectra change constantly in the course of a solar cycle. Therefore, each measured spectrum only has validity in a limited time period. For the study of GCR-induced radiation in the atmosphere, appropriate spectra are necessary that are consistent with the respective solar activity.

In this work the "force field model" of *Gleeson and Axford (1968)* is used to describe the primary proton spectrum arriving at the orbit of the Earth. It is a mathematical model that varies the shape of the spectrum according to the current solar activity, so that it fits to measured data sets. It only depends on one single parameter, the *modulation potential* ϕ. The flux is related to the undisturbed GCR flux in the local interstellar medium as follows: [35]

$$\frac{j_{1AU}(E_{kin})}{E^2 - m_0^2} = \frac{j_{LIS}(E_{kin} + |z|\ e\ \phi)}{(E + |z|\ e\ \phi)^2 - m_0^2} \tag{26}$$

The modulation potential ϕ is usually given in MV and is available for a time period stretching from several decades in the past until present time. It describes the modulating effect of the solar cycle on the GCR flux. During solar maximum, the potential is very high with values of typically 1000 MV, therefore deflecting low energy particles. If the Sun is in solar minimum, the potential is about 400 MV and less particles are lost. In equation (26), E_{kin} is the kinetic

energy of the particles at the position of Earth and the quantity $|z|\ e\ \phi$ represents the energy that a particle loses on its path through the interplanetary space. E is the total energy, thus the kinetic energy plus the rest mass $m_0 = mc^2$ of the particle. The last remaining quantity is j_{LIS}, the local interstellar omnidirectional particle flux, in other words, the particle flux outside the influence of the Sun. In literature a variety of different models for the local interstellar flux can be found, that all give reasonable results, if the appropriate modulation parameter is chosen [36]. Therefore, one has to be careful with the choice of the correct value for the modulation potential. In this work, the model by *Garcia-Munoz et al. (1975)* is used: [35]

Unit: $cm^{-2}\ s^{-1}\ MeV^{-1}$

$$j_{LIS}(E_{kin}) = 1.244 \cdot 10^6 \left(E_{kin} + 780 \cdot exp(-2.5 \cdot 10^{-4} E_{kin})\right)^{-2.65} \quad (27)$$

A list of reconstructed monthly modulation potentials from 1936 until now (2014) is offered by the *Oulu Cosmic Ray Station* and is listed in Table 26 in the appendix. However, these values have to be transformed in order to use them in the LIS model described above, as they were obtained using a different LIS model by *Burger et al. (2000)* . This is done by using a linear equation: [36]

Unit: MV

$$\phi_{LIS\ GM} = m \cdot \phi_{LIS\ Oulu} + b \quad (28)$$

with

$$m = 1.03378;\ b = -48.0287$$

All modulation potentials mentioned in the further course of this work are converted values compatible to the model by Garcia-Munoz et al. Equation (26), (27) and (28) combined yield GCR primary proton spectra used for the calculations in this thesis. Figure 19 shows the different shapes of spectra for solar minimum and solar maximum. Here it can be seen, that the modulation only affects the low energy range. Above approximately 10 GeV the modulation is very small.

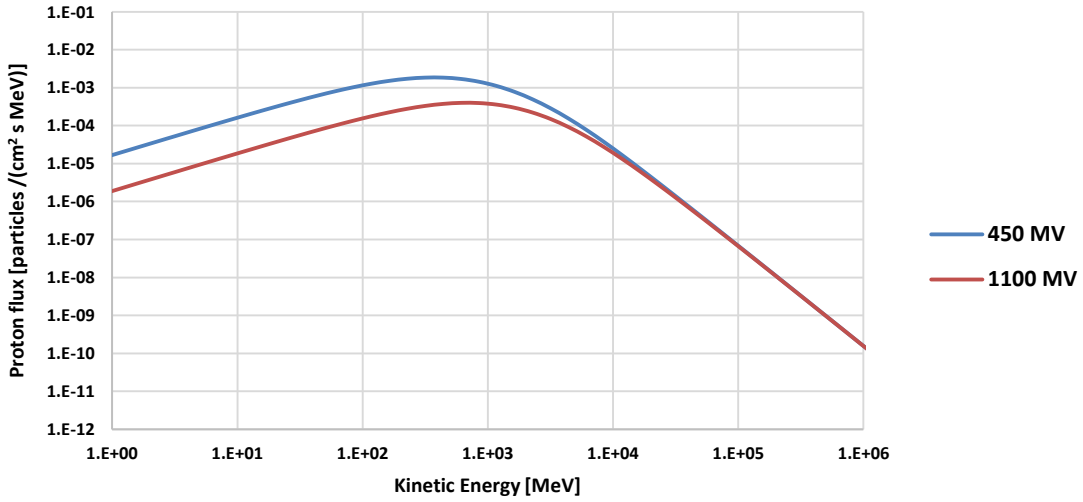

Figure 19: GCR proton flux for solar minimum (blue) and solar maximum (red) (calculated by equation (26) and (27))

3.3.1.2 Reconstruction of the SCR proton spectrum using neutron monitor count rates

As presented in section 2.3, a neutron monitor measures the neutron flux at ground level in order to deduce the cosmic ray spectrum arriving at the orbit of the Earth. For this purpose, an energy-dependent *yield function* is necessary that connects the cosmic ray energy spectrum with the measured neutron count rate on the ground, by considering the atmospheric transport as well as the neutron monitor detection efficiency. The relation between measured neutron flux and primary proton spectrum is given as [37]

$$N(R_{C,}, z, t) = \int_{R_C}^{\infty} S(R, z) \cdot J(R, t) \cdot dR \tag{29}$$

with
R .... *primary particle rigidity* [GV]
R_C .. *effective vertical cutoff rigidity at the position of the monitor* [GV]
z ..... *atmospheric depth of the neutron monitor* [g cm^{-2}]
J ..... *primary proton rigidity spectrum* [#/(cm^2 s sr GV)]
S ..... *proton yield function* [m^2 sr]
N .... *Neutron monitor count rate* [s^{-1}]

The proton yield function for a standard 6-NM64 neutron monitor can be expressed by the following formula: [37]

$$\log S(R, z) = \sum_{m,n=0}^{3} C_{mn} \cdot z^m \cdot (\log R)^n \tag{30}$$

Here, C_{mn} are the coefficients for a standard 6-NM64 neutron monitor, listed in Table 7.

Table 7: Standard 6-NM64 proton yield function coefficients [37]

C_{mn}	$n = 0$	$n = 1$	$n = 2$	$n = 3$
$m = 0$	*7.983E-1*	*2.859E+0*	*-2.060E+0*	*5.654E-1*
$m = 1$	*-6.985E-3*	*1.188E-2*	*-9.264E-3*	*2.169E-3*
$m = 2$	*3.593E-6*	*-1.516E-5*	*1.522E-5*	*-4.214E-6*
$m = 3$	*-1.950E-9*	*7.969E-9*	*-8.508E-9*	*2.491E-9*

The neutron monitor count rates used for the spectrum calculations were retrieved from the database of the *Oulu Cosmic Ray Station*. The Oulu neutron monitor is located in Finland at an altitude of 15 m above sea level at an cutoff rigidity of approximately 0.8 GV [38]. The downloaded data are pressure corrected, which means, that the count rate is normalized to a pressure of 1000 mbar. This corresponds to an atmospheric depth of $z = 1019$ g cm^{-2}. In the next step, equation (30) is reorganized by inserting the coefficients C_{nm} from Table 7 and the atmospheric depth z. Additionally, a normalisation factor $\alpha = 1.499$ is introduced that considers the shielding of the housing of the NM and the circumstance that the Oulu NM is a 9-NM64 device with 9 tubes [39]. The resulting Oulu yield function in [cm^2 sr] is presented in equation (31):

$$S^{Oulu}(R) = \frac{1}{1.499} \cdot 10^{-0.65+7.66 \cdot log_{10}(R) - 4.70 \cdot \left(log_{10}(R)\right)^2 + 1.04 \cdot \left(log_{10}(R)\right)^3} \tag{31}$$

The combination of equation (29) and (31) leads to an equation for the neutron count rate increase of the Oulu NM station during a GLE [39]:

$$\Delta N^{Oulu}(t) = N^{Oulu}(t) - N^{Oulu}(t_0) = \int_{R_C^{Oulu}=0.8\ GV}^{20\ GV} S^{Oulu}(R) \cdot J_{SCR}(R,t) \cdot dR \tag{32}$$

$\Delta N^{Oulu}(t)$ .....*absolute count rate increase* [s^{-1}]
$N^{Oulu}(t)$.....*count rate during GLE event at time t* [s^{-1}]
$N^{Oulu}(t_0)$ .....*averaged count rate before the GLE* [s^{-1}]
$S^{Oulu}(R)$.....*Oulu Yield Function* [cm^2 sr]
$J_{SCR}(R,t)$ .....*Solar cosmic ray proton flux* [$\#/(cm^2$ s sr GV)]
R_C^{Oulu} .....*Effective vertical cutoff rigidity at position of Oulu NM* [GV]

The last remaining component is the SCR spectrum itself. The spectrum is expressed in the rigidity domain and can be approximated by a power law. It has two important ingredients, its *amplitude A* and its *slope* γ*:* [37]

$$J_{SCR}(R,t) = A(t) \cdot \left(\frac{R}{1\ GV}\right)^{-\gamma(t)} \tag{33}$$

$A(t)$ .....*Amplitude at time t* [$\#/(cm^2$ s sr GV)]
$\gamma(t)$.....*Slope of the spectrum at time t*

Both amplitude and slope depend on time. The slope represents the hardness of the spectrum. As explained in the theory section 2.1.2, the high-energy particles are the first ones to arrive at Earth, hence the spectrum at the beginning of the GLE is harder than during later stages. This fact is modelled by a slope that increases over time. The true value for γ can be determined by using a larger group of neutron monitors. This was not done in this study. Here, only two values for the slope are considered, a minimum value ($\gamma = 4$) and a maximum value ($\gamma = 7$), which represent two extreme moments during a GLE. This can be viewed as a best-case and a worst-case scenario and defines a reasonable range for the spectrum and the resulting dose rates.

The last unknown parameter is the amplitude, which now can be calculated by inserting equation (33) into equation (32), replacing the integral by a sum and solving for A. This leads to two time series for the amplitude, one for $\gamma = 4$ and one for $\gamma = 7$.

$$A(t) = \frac{\Delta N^{Oulu}(t)}{\sum_{0.8\ GV}^{20\ GV} S^{Oulu}(R) \cdot R^{-\gamma} \cdot \Delta R} \tag{34}$$

Using the amplitude calculated from the equation above, the neutron monitor count rate and the power law from equation (33), the SCR spectrum can be calculated for every time step during the GLE. Figure 20 compares the GCR spectrum for solar minimum ($\phi = 400$ MV) with the

two SCR-spectra for GLE69. It is immediately obvious that the SCR proton flux below approximately 1000 MeV is several orders of magnitude higher than the GCR flux. This elevated proton flux poses a threat to air traffic through the polar regions. Section 5.1 analyses the dose rates that are expected to arise from some historic solar events.

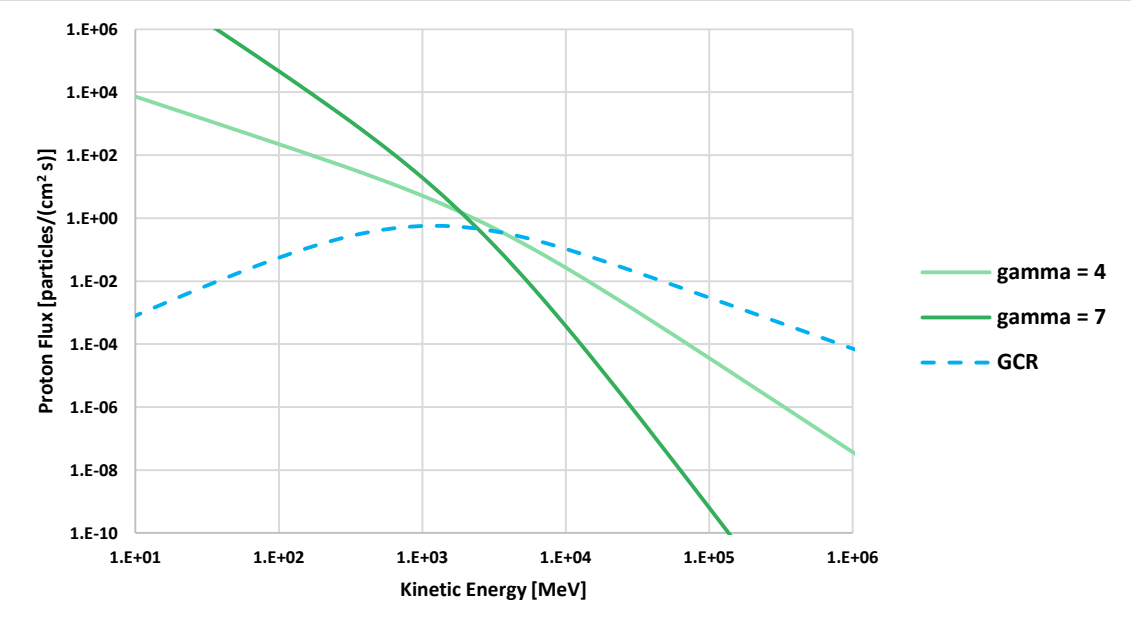

Figure 20: SCR spectra for GLE69 during maximal intensity for $\gamma = 4$ and $\gamma = 7$ compared with GCR spectrum during solar minimum ($\phi = 400$ MV)

3.3.2 Geographic coordinate

The quantity, which is directly connected with the geographic coordinate on Earth, is the magnetic field. Up to this point, the magnetic field has not been considered in the simulation model. However, as described in section 2.2, the magnetic field has a strong shielding effect on the cosmic radiation, which has to be included in the further analysis. This is done by considering the *vertical cutoff rigidity* R_C that describes the shielding efficiency for a certain position on Earth. A charged particle can only enter the atmosphere if its *magnetic rigidity* R_p (equation (2)) is higher than the vertical cutoff rigidity R_C at its point of entry. Otherwise it is deflected by the Lorentz force and therefore cannot contribute to any dose production. As a consequence, the magnetic field at a certain entry point can be considered by cutting the low energy part of the input spectrum according to the associated cutoff rigidity value.

A world grid of vertical cutoff rigidity values was determined by *Shea et. al.* and is listed in Table 27 in the appendix. Values for coordinates that lie between the nodes of the grid are interpolated during the calculation. In order to cut the input spectrum, it first has to be converted from the usual energy domain (MeV or GeV) into the rigidity domain (GV). Following this, it is compared to the associated cutoff rigidity value and then the flux below this value is set to zero. This cut corresponds to the deflection of the low energetic protons. For the conversion of the spectrum into the rigidity domain, two equations are needed. The first one is the equation for the magnetic rigidity of a charged particle, which was already described in equation (2), but in a slightly rearranged way:

$$pc = R_p \cdot q \tag{35}$$

The second is Einstein's formula for the mass-energy equivalence:

$$E^2 - (pc)^2 = (mc^2)^2 \tag{36}$$

Here, E is the *total energy* ($E = E_0 + E_{kin}$) in Joule, E_0 is the *rest energy* ($E_0 = mc^2$) and E_{kin} the kinetic energy of the particle. Plugging in equation (35) into equation (36) and solving for the magnetic rigidity R_p leads to the final conversion equation:

Unit: GV

$$R_p = \frac{1}{q}\sqrt{2E_0E_{kin} + E_{kin}^2} \tag{37}$$

The next step is to retrieve the value for the vertical cutoff rigidity R_p that is associated with the geographic coordinate of interest. Finally, the range of the converted spectrum that lies below the cutoff value is set to zero. This procedure is demonstrated in Figure 21. The blue line shows a GCR spectrum for the North Pole (90° N 0° O) where the vertical cutoff rigidity is zero. Here, the magnetic field provides no shielding effect, therefore the spectrum is untouched. The dashed black line shows the cut of the spectrum as it would be the case at the geographic coordinate of Vienna, which is 48° 12' N 16° 22' O. The vertical cutoff rigidity at this coordinate is 4.2 GV, which is why there is no flux below this rigidity value. The cut at the equator is marked by the dashed red line. The vertical cutoff rigidity at 0° N 0° O amounts to 13.7 GV, so the energy region of particles that cannot enter the atmosphere is even wider.

The above described procedure is not only applied on the GCR- but also on the SCR spectra. Only then, after the consideration of the vertical cutoff rigidity at the considered geographic location, the spectrum serves as input for the Flux-matrix. This procedure is illustrated in Table 8.

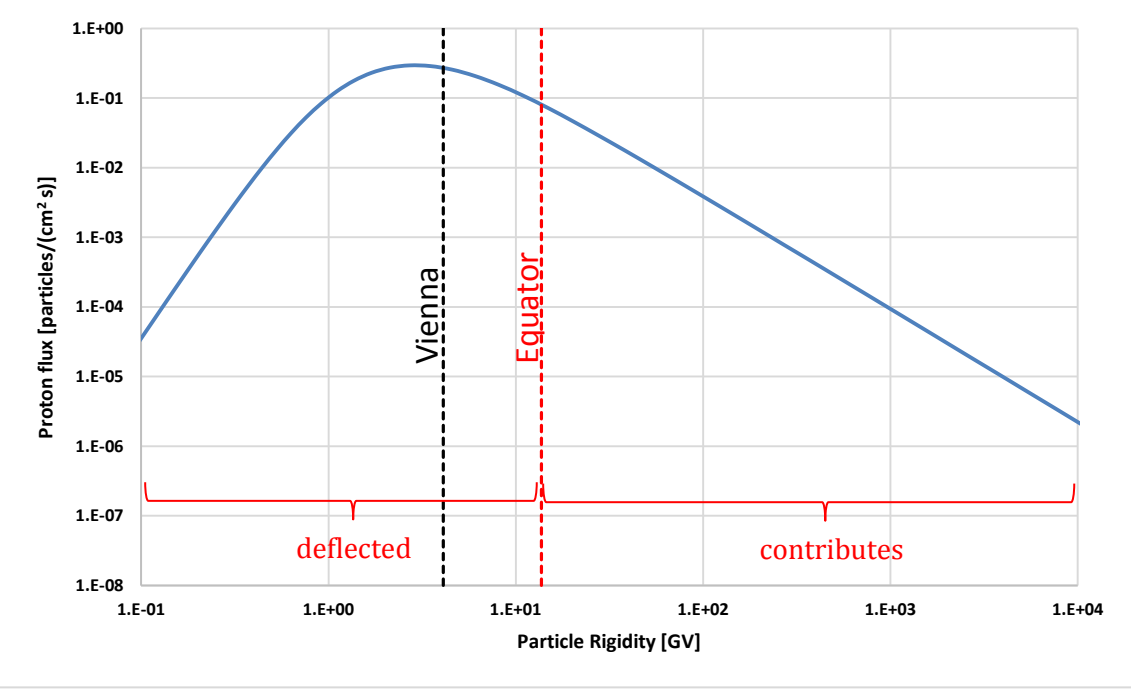

Figure 21: The blue line represents the GCR proton spectrum ($\phi = 1000$ MV) for $R_C = 0$ GV as it would be in the polar regions; dashed lines show the cuts for Vienna ($R_p = 4.2$ GV) and Equator ($R_p = 13.7$ GV)

Table 8: Illustration of how the cut spectrum effects the flux-matrix

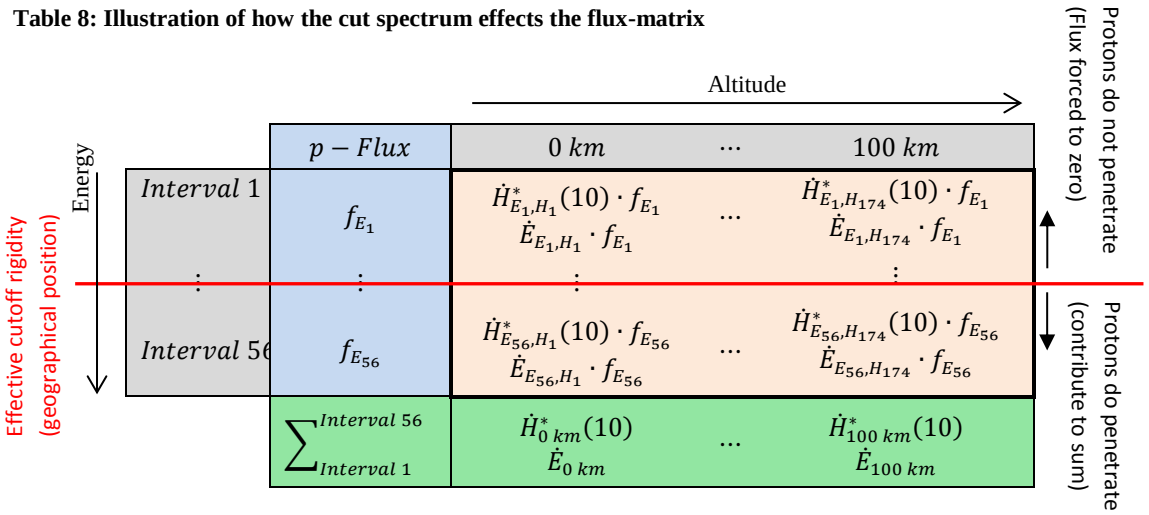

3.3.3 Altitude

The altitude dependence of the radiation doses goes hand in hand with the density profile of the atmosphere. As already explained in the theory section for atmospheric showers (section 2.4.2), there is a distinct maximum of the dose production rate at an altitude of approximately 20 km. This maximum is achieved through the interplay of the particle density in the atmosphere and absorption as well as recombination processes. *PLANETOCOSMICS* uses for the simulation of the particle interactions the *NRLMSISE00* model, which describes the atmospheric density dependence on altitude and several other parameters.

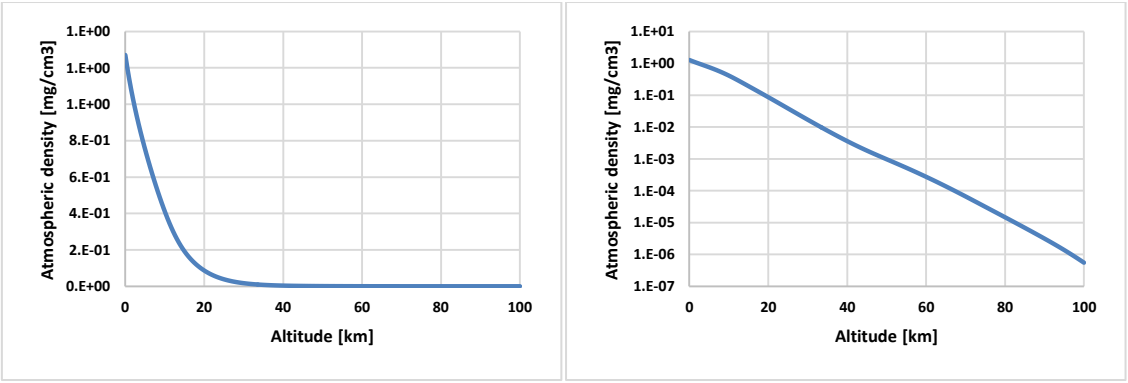

Figure 22: Atmospheric density profile of the *NRLMSISE00* model used in *PLANETOCOSMICS*

In order to retrieve a dose rate at a certain altitude from the Flux-matrix, the respective column has to be selected. Afterwards, the energy dependent entries are weighted by the proton spectrum and summarized.

4 Simulation results for dose rates caused by galactic cosmic radiation

This chapter displays the simulation results for GCR-induced dose rates that were computed using the simulation model described in chapter 3 and the GCR input spectrum according to chapter 3.3.1.1 and 3.3.2. At first, a typical output of such a simulation is presented. Following this in section 4.1, the precision of the simulation is verified by means of reference values. At the end of the chapter in section 4.2, the dose rates for different solar activities and cutoff rigidities are discussed.

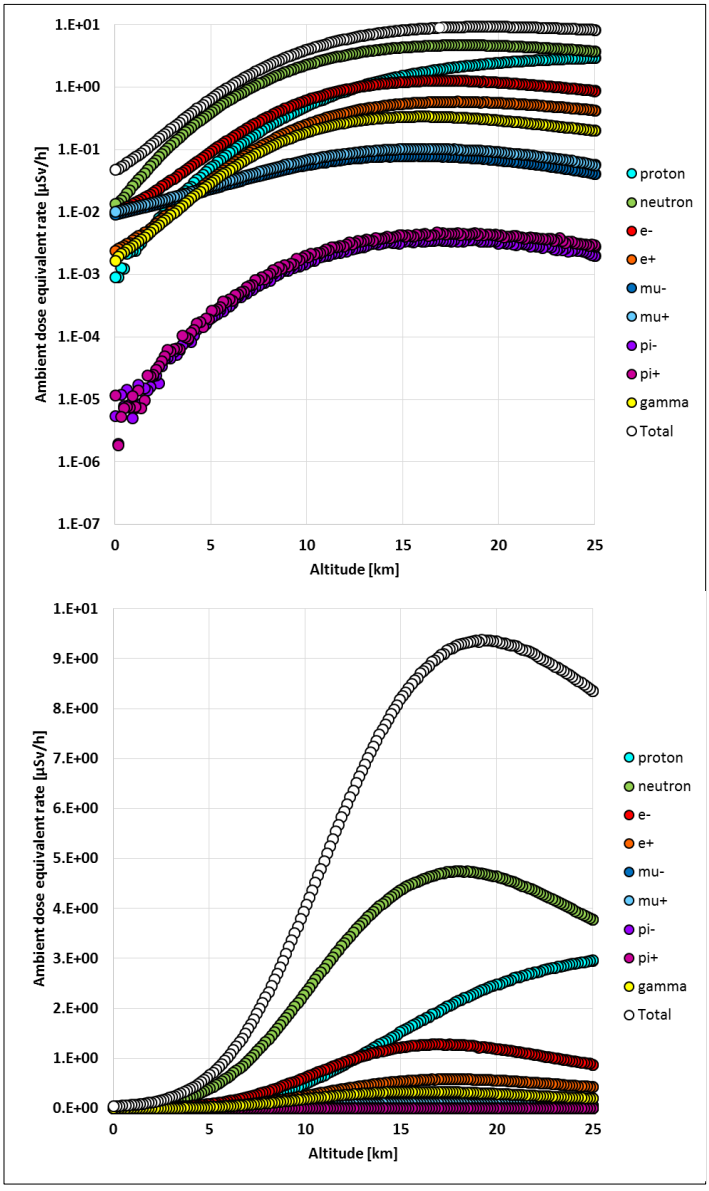

Figure 23: Typical output of a simulation; contributors to ambient dose equivalent rate as a function of altitude (top: logarithmic scale; bottom: linear scale)

Figure 23 on the left demonstrates how a typical output of a simulation looks like. For this example a cutoff rigidity of 0 GV and a modulation potential of 900 MV was chosen. Both diagrams show the resulting ambient dose equivalent rates produced by the various secondary cosmic radiation components as a function of altitude. The bottom diagram is shown in a linear representation where the *Pfotzer maximum* is clearly visible. Here, the highest dose rate can be found at an altitude of 19.2 km with a value of 9.4 µSv/h. Since the values of the dose rates stretch across many orders of magnitude, the diagram is usually plotted logarithmically as it was done in the top figure. At high altitudes, the main contributors to the dose rate are neutrons and protons. Near the ground however, the distribution looks very different. Here, neutrons, electrons and both positively and negatively charged muons play the most important role, while protons only have a very small contribution to the dose. The smallest contributor throughout the whole altitude range are the pions with only a fraction of a percent. The distribution of contributors to the dose rates is discussed in more detail in section 4.2.

4.1 Comparison with ICRU reference values

In order to verify the simulation results, a comparison with reference values is necessary. These values are provided by the *International Commission on Radiation Units & Measurements (ICRU)*, which result from a variety of coordinated and summarized in-flight measurements of the doses from cosmic radiation exposure of aircraft crew. The reference values are given as ambient dose equivalent rate at three typical flight altitudes for three time periods and for 18 vertical cutoff rigidity values. The altitudes are FL310, FL350 and FL390, given in *flight levels*, where the number counts the multiples of 100 feet above the reference level with a pressure of 1013.25 hPa. The time periods were chosen in such a way, that different solar activities are considered. These are the solar minimum for January 1998, the intermediate solar activity for January 2000 and the solar maximum for January 2002. The reference values are available for the whole range of vertical cutoff rigidity, from 0 GV to 17 GV in increments of 1 GV. [40] For a list of these values, see Table 28 through Table 33 to in the Appendix.

After converting the related modulation potentials of the *Oulu Cosmic Ray Station* with equation (28) and cutting the resulting spectra according to the cutoff rigidity values specified by ICRU, the simulations were performed and the dose rates at the three flight levels retrieved. Figure 24 through Figure 26 show the agreement in a graphical representation. The calculated values including percental deviations from the ICRU reference values are listed in tabular form in the appendix. During January 1998 the Sun had minimal activity, which corresponds to a very low modulation potential of 393 MV. The calculated results presented in Figure 24 agree quite well with the reference values. Only for very low cutoff rigidity values, the simulation model overestimates the dose rates up to 27 %. For high cutoff rigidities, the simulation results are about 10 % lower than the reference.

The modulation potential for January 2000 is 729 MV, almost twice as high as in January 1998. Because of the higher solar activity the results in Figure 25 show lower dose rates. The results of the simulation model agree very well with the reference values. The biggest percental deviations from the reference are the results for the high cutoff rigidity values. Here, the dose rates are slightly underestimated. The third data set of reference values is for the time of the solar maximum in January 2002. The modulation potential for this period is 961 MV. Again, the results in Figure 26 agree well with the reference values. A high percental deviation only occurs for the high cutoff rigidity values.

On the whole the simulation model achieves results that agree quite well with the reference values. The only major deviations occur for low cutoff rigidities in the case of solar minimum in January 1998. The most likely reason for the overestimation of these dose rates is the choice of a too low modulation potential. If this is the case, the low energy flux of the GCR spectrum is too high, which affects the dose rates for low cutoff rigidities. The high cutoff range is not affected, since the modulation only changes the low energy flux of the spectrum, which cannot penetrate at these values. Consequently, the choice of an appropriate modulation potential is crucial.

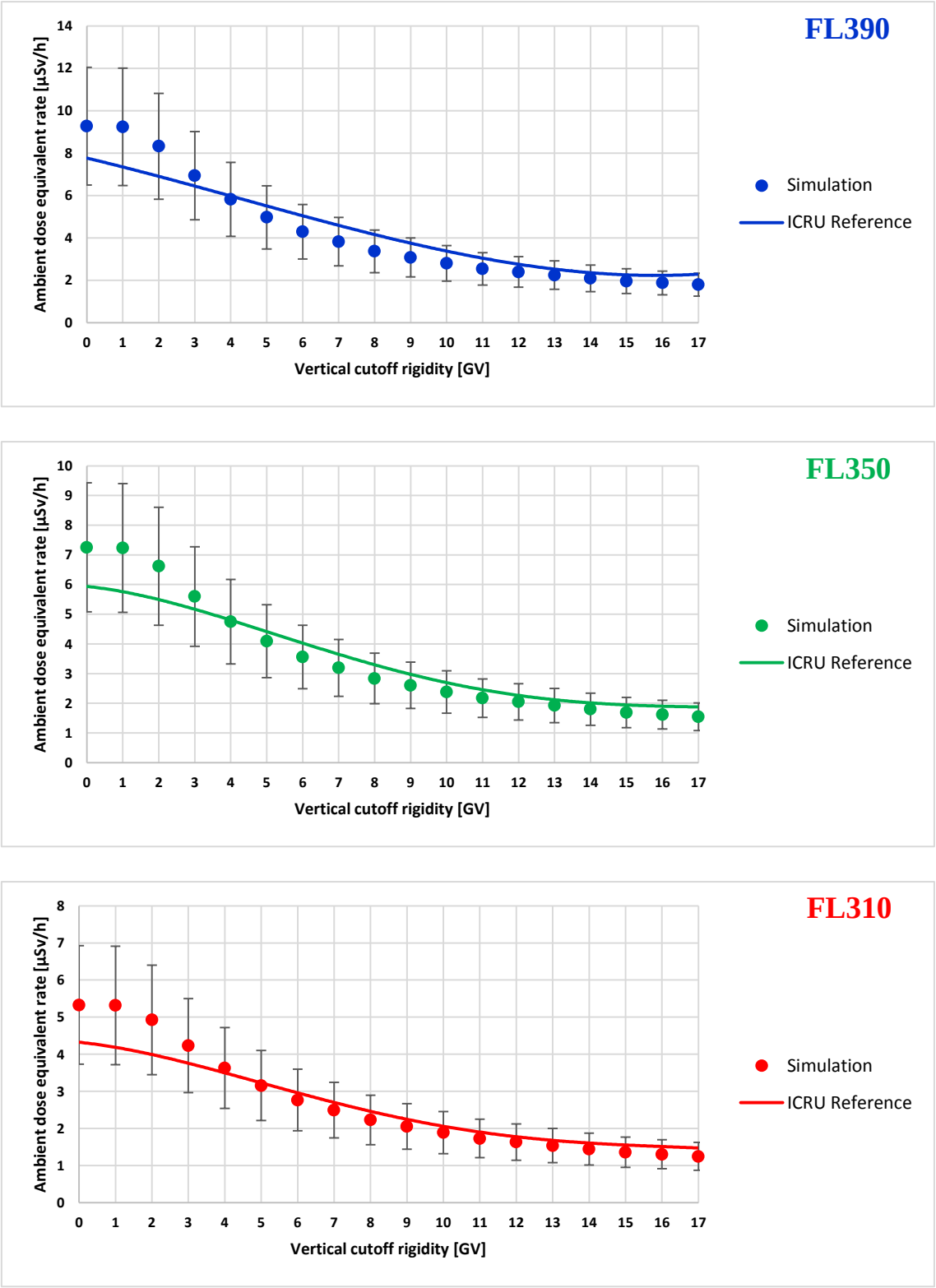

Figure 24: Comparison to ICRU reference values for January 1998; simulation results with modulation potential $\phi = 393$ MV; error bars indicate a range of ± 30 %

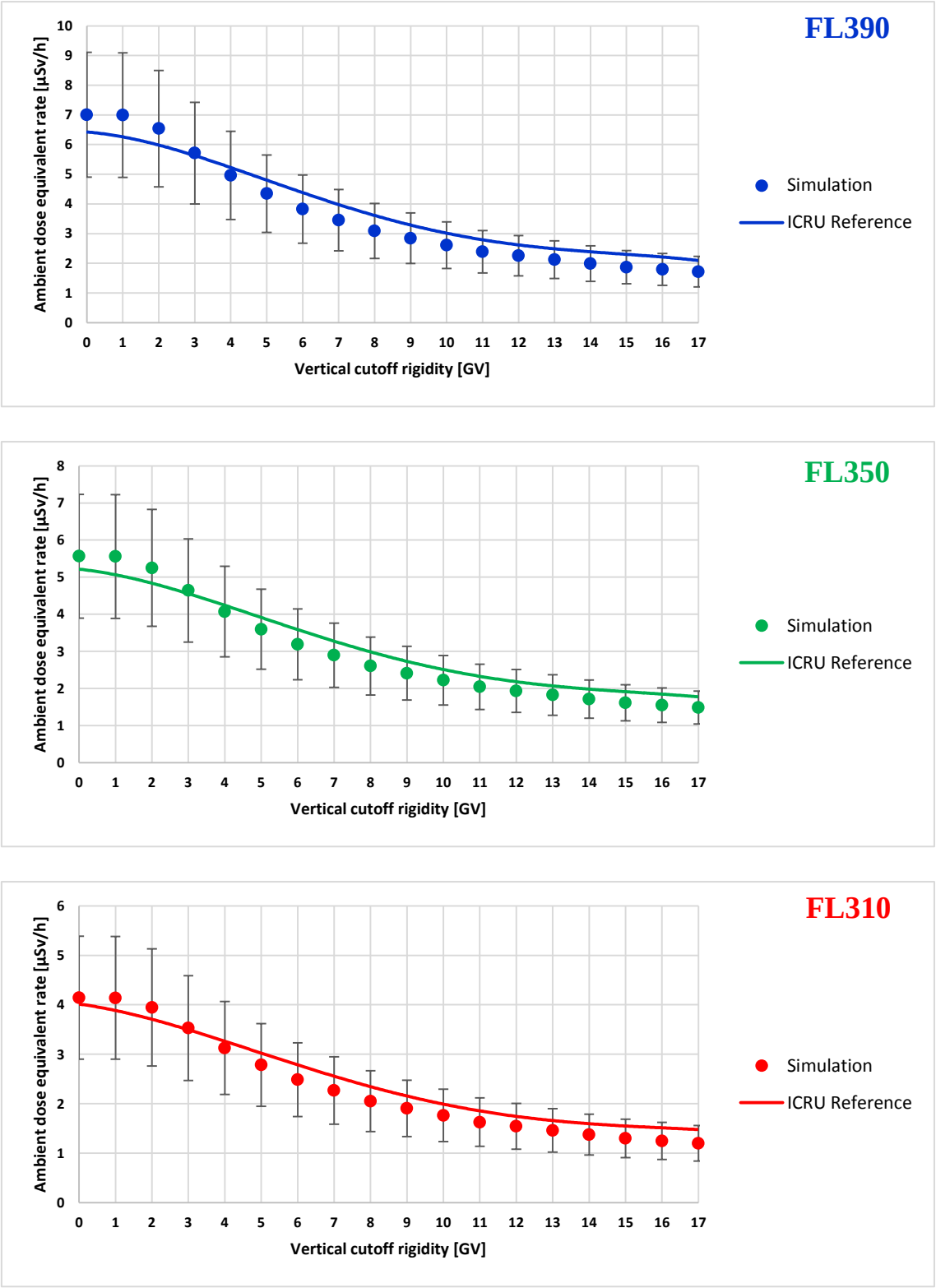

Figure 25: Comparison to ICRU reference values for January 2000; simulation results with modulation potential $\phi = 729$ MV; error bars indicate a range of ± 30 %

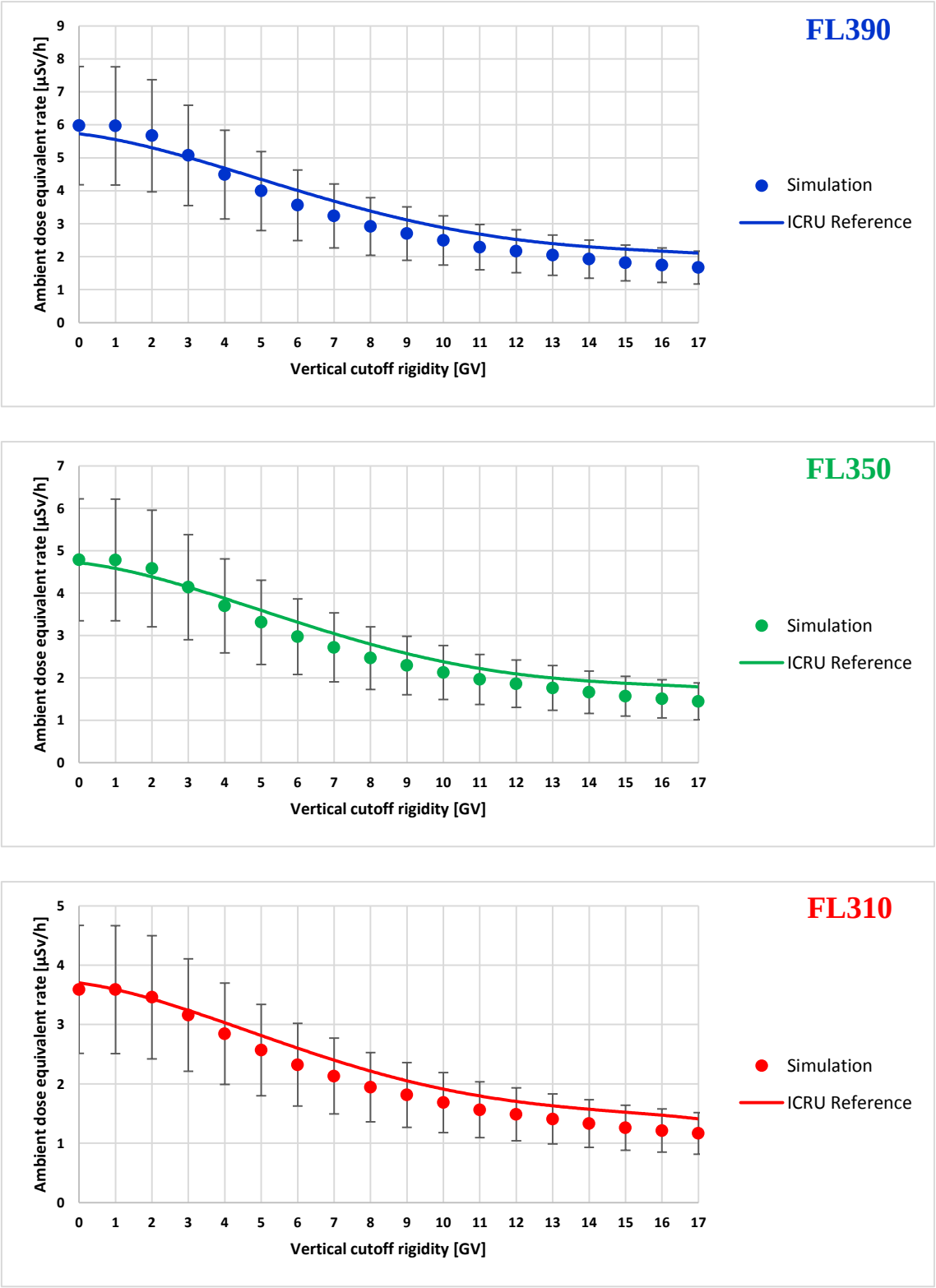

Figure 26: Comparison to ICRU reference values for January 2002; simulation results with modulation potential $\phi = 961$ MV; error bars indicate a range of ± 30 %

4.2 Simulated dose rates during solar minimum and solar maximum

This chapter displays a variety of simulation results for GCR-induced dose rates in the atmosphere and illustrates the impacts of the three major influencing factors on the radiation exposure. Figure 27 simultaneously demonstrates, how the change of these influencing factors, solar activity (ϕ), geographical position (R_C) and altitude (km, FL), effects the total dose rate. Four extreme cases have been considered, two for solar minimum and two for solar maximum, each for a high and a low cutoff rigidity value, which correspond to low and high latitude regions. The red curves show the dose profiles for solar minimum, the ones in green correspond to solar maximum. Three characteristics are immediately visible. First of all, the dose rates strongly decrease with decreasing altitude due to atmospheric shielding. Near the ground, the dose rates are only a fraction of a µSv per hour, at flight altitude however, for instance at 10 km, the dose rates lie between 1.5 and 6.2 µSv per hour. The second eye-catching feature is the large split between the dose profiles for low and high cutoff rigidity regions. This split is even more pronounced during the time of solar minimum and is caused by magnetic shielding (see section 2.2 and 3.3.2). The third influencing factor is the solar activity, which, as clearly visible in Figure 27, only has a strong effect on low cutoff rigidity regions. As described in the previous section, equatorial regions with high cutoff rigidity values are only little affected by the solar modulation, since the modulation does not change the high energy flux, which is responsible for the radiation production at these positions. A set of selected dose rates for the four considered cases is listed in Table 9 and additionally shows the dose variability in numbers.

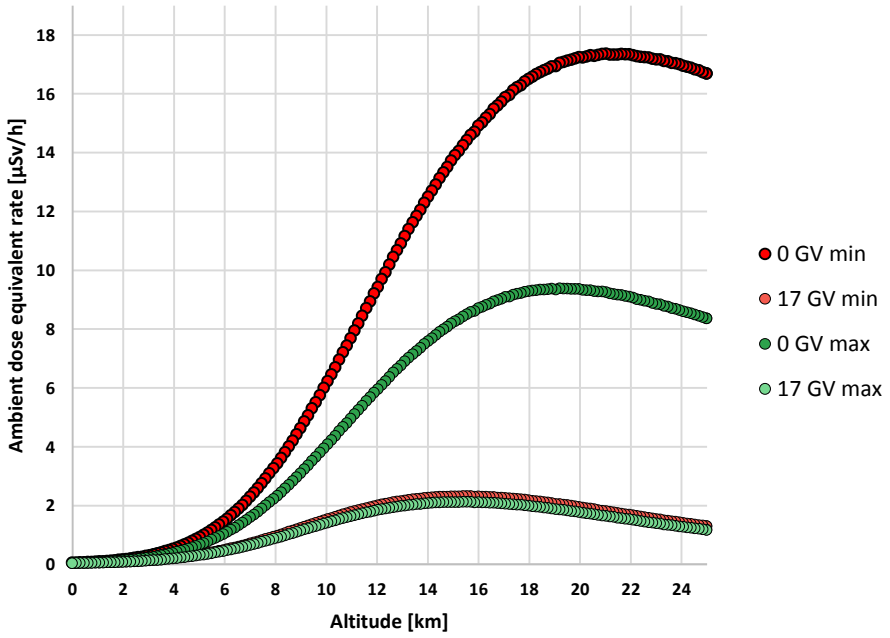

Figure 27: Height profile of total ambient dose equivalent rate for solar minimum($\phi = 400$ MV) and solar maximum ($\phi = 1000$ MV) at cutoff rigidity 0 GV and 17 GV

Table 9: Ambient dose equivalent rate in µSv/h for selected altitudes

ϕ [MV]	R_C [GV]	0 km	3 km	8 km	10 km	12 km
400	0	0.1	0.3	3.4	6.2	9.4
	17	0.0	0.1	1.0	1.5	2.0
1000	0	0.0	0.2	2.3	4.1	6.0
	17	0.0	0.1	0.9	1.5	2.0

The total ambient dose equivalent rate is the result of many contributors. The significance of these contributors depend on the altitude, as depicted in Figure 28 and Table 10. The main portion of the dose rate on all heights below approximately 25 km is caused by neutrons, above by protons. Towards the ground, protons lose most of their importance, while the importance of electrons increases. The contribution of positrons, photons and pions is rather low and constant throughout the whole altitude range. The same holds for muons, except for very low altitudes, where the contribution reaches almost 20 %.

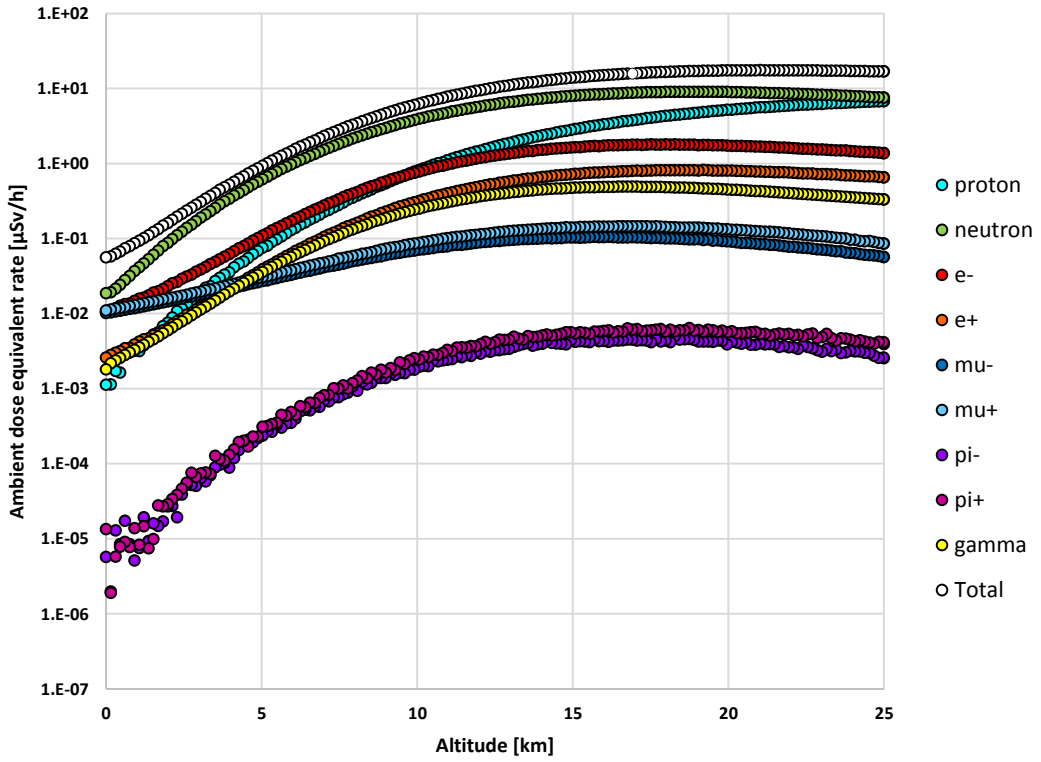

Figure 28: Ambient dose equivalent rate profile for all dose contributors for solar minimum ($\phi = 400$ MV) and cutoff rigidity $R_C = 0$ GV

Table 10: Percentage contribution to ambient dose equivalent rate for the above depicted dose rate profile

altitude	0 km	5 km	10 km	15 km	20 km	25 km
proton	2.02%	8.10%	13.05%	20.56%	29.80%	40.18%
e-	18.69%	11.67%	12.44%	11.81%	9.96%	8.17%
e+	4.64%	4.16%	5.03%	5.18%	4.63%	3.91%
mu-	18.13%	2.91%	1.14%	0.74%	0.53%	0.34%
mu+	19.72%	3.27%	1.40%	1.00%	0.77%	0.51%
pi-	0.01%	0.03%	0.03%	0.03%	0.02%	0.02%
pi+	0.02%	0.03%	0.04%	0.04%	0.03%	0.02%
gamma	3.24%	3.82%	4.00%	3.39%	2.60%	1.98%
neutron	33.53%	66.01%	62.87%	57.24%	51.66%	44.88%
total	100.00%	100.00%	100.00%	100.00%	100.00%	100.00%

The energy distributions of particle fluxes for neutrons, protons and electrons are given in Figure 29.

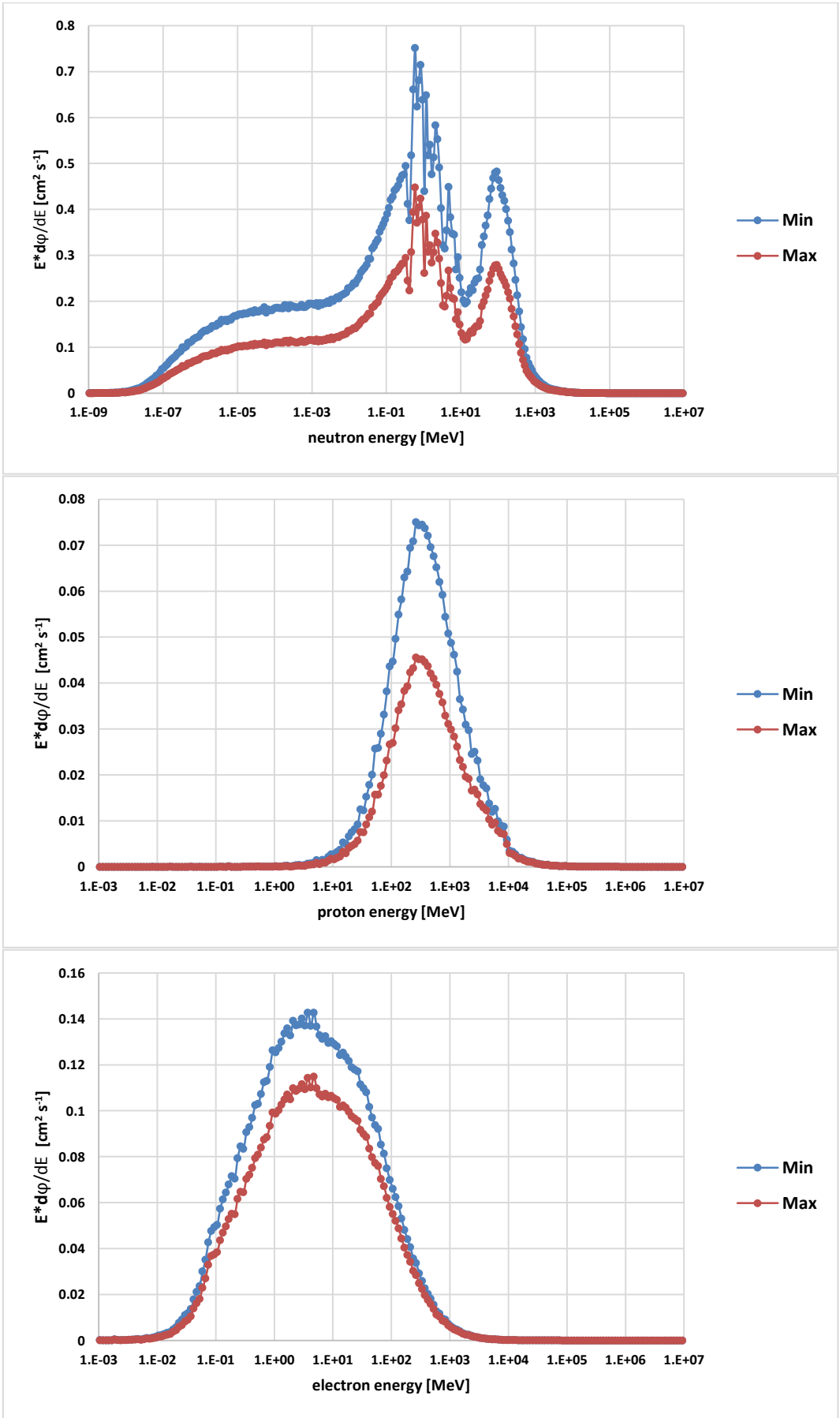

Figure 29: Energy spectra for neutrons, protons and electrons at $FL350 \triangleq 10.67$ km for solar minimum ($\phi = 400$ MV) and solar maximum ($\phi = 1000$ MV)

The graphic below shows two dose maps produced by the simulation model, which illustrate the dose rate distribution across the globe for solar minimum and solar maximum at a typical commercial aircraft altitude. During a solar minimum the radiation exposure in northern and southern areas is by about a factor of 4 higher than in equatorial regions, during a solar maximum only by afactor of around 2.

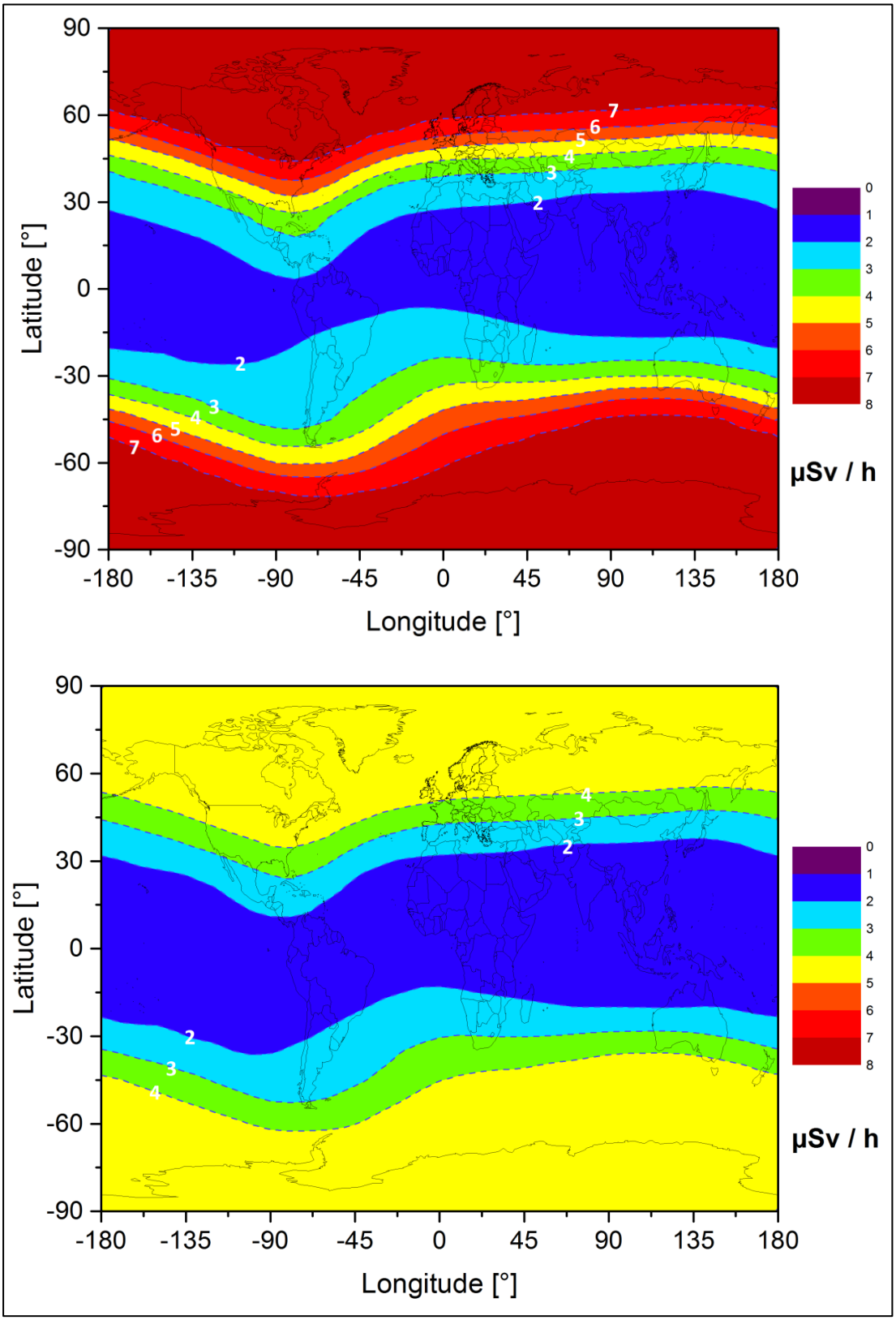

Figure 30: Dose map for ambient dose equivalent rate for solar minimum $(top;\ \phi = 400\ \text{MV})$ and solar maximum $(bottom;\ \phi = 1000\ \text{MV})$ at altitude $FL350 \triangleq 10.67$ km

Since the dose maps in Figure 30 only show the dose rate distribution at one single altitude, the altitude dependence is demonstrated in Figure 31 by looking at the dose rates along the prime meridian from the south to the north pole at different altitudes, both for solar minimum and solar maximum. In the polar regions, the climb of one kilometer corresponds to a dose rate increase of approximately 2 µSv per hour during solar minimum, and approximately 1 µSv per hour during solar maximum.

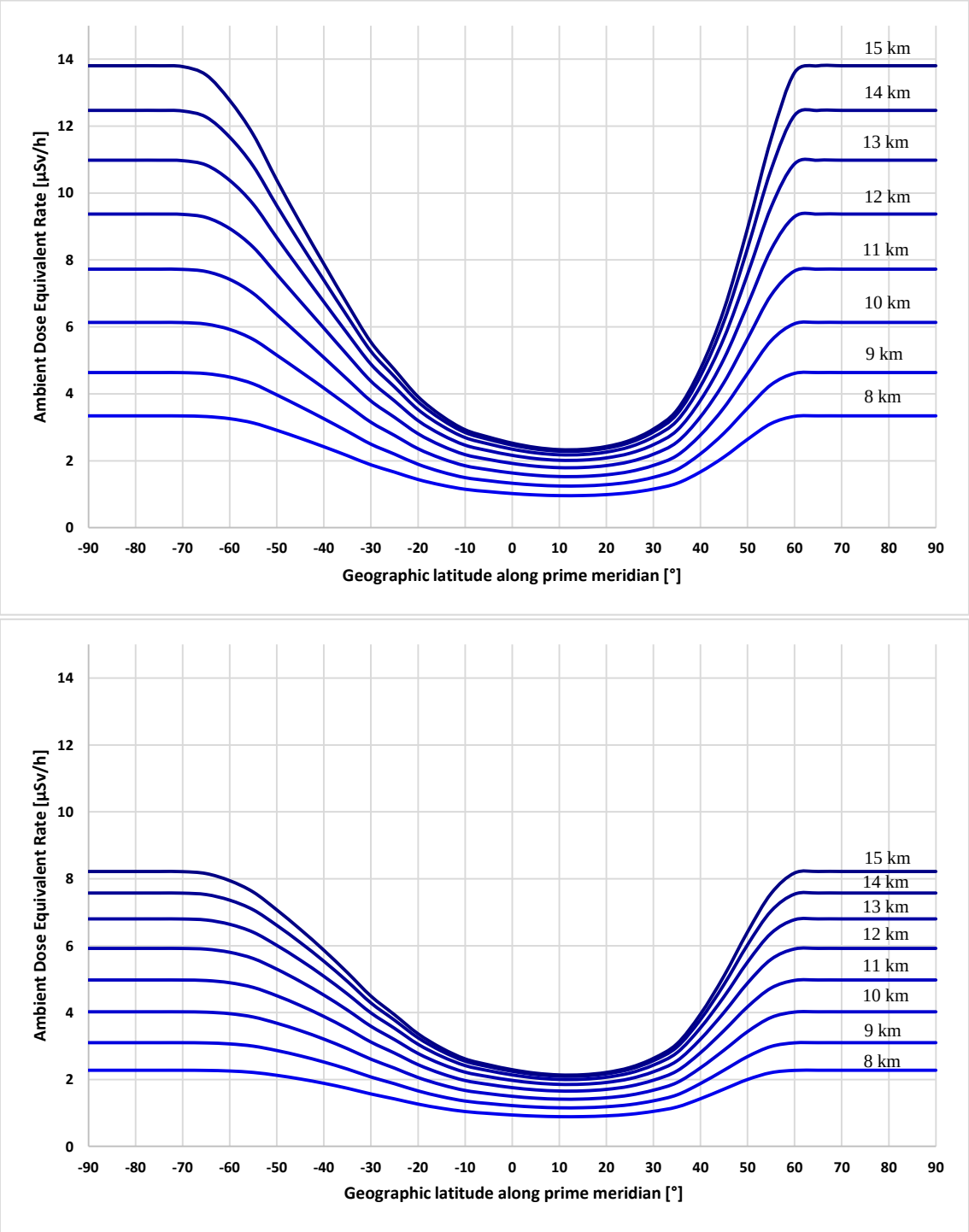

Figure 31: Ambient dose equivalent rate along prime meridian during solar minimum (top; $\phi = 400$ MV) and solar maximum ($bottom$; $\phi = 1000$ MV) at different altitudes from 8 to 15 km

4.3 TEPC flight-measurement

4.3.1 Measured dose rates

On 2nd of September 2014, a TEPC flight measurement was performed in cooperation with the military airbase in Zeltweg (Austria). The measuring instrument, a TEPC "HAWK" (see section 2.6.1), was transported in a Eurofighter and the radiation doses at two flight levels were determined. The duration of the entire flight, the durations at the individual flight altitudes as well as the altitudes in kilometers are listed in Table 11.

Table 11: Duration and altitudes of measurement flight

	$\boldsymbol{Duration}$ [min]	$\boldsymbol{Altitude}$ [km]
$\boldsymbol{FL400}$	30	12.2
$\boldsymbol{FL450}$	17	13.7

The GPS-receiver of the TEPC device had to be deactivated during the measurement for reasons of secrecy. However, the variation in altitude can easily be seen in the change in dose rate of the low LET channel depicted in Figure 32. Here, the time increment is one minute. The total dose rate, which is the sum of the doses from the high and the low LET channel, is plotted in the bottom diagram of Figure 32. Please note, that in the figures, the unit of the dose rate is the dose equivalent rate $\dot{H}$ and not the ambient dose equivalent rate $\dot{H}^*(10)$, as it was the case in the previous chapter. The time periods of the measurements at the two flight levels were identified using the dose profile of the low LET range. Two distinct plateaus can be distinguished, which correspond to the flight levels of interest. In the next step, the dose rates during these time periods were averaged and converted into ambient dose equivalent Rate $\dot{H}^*(10)$, allowing an easier comparison with the simulated values. The measured dose rates at the two flight levels are listed in Table 12. The calculation of the corresponding uncertainties can be looked up in the appendix on page 85.

Table 12: Results of TEPC measurement in ambient dose equivalent rate at altitudes $\boldsymbol{FL400 \triangleq 12.2}$ km and $\boldsymbol{FL450 \triangleq 13.7}$ km

	$\boldsymbol{\dot{H}^*(10)}$ [µSv/h]
$\boldsymbol{FL400}$	5.4 ± 0.7
$\boldsymbol{FL450}$	7.4 ± 1.1

The dose distribution as well as the distribution of dose equivalent for the two flight levels are depicted in Figure 33. Even though the majority of the dose is produced by low-LET events with a lineal energy smaller than $10\ \mathrm{keV/\mu m}$, the biological hazard comes for the most part from the high-LET events above $10\ \mathrm{keV/\mu m}$.

4.3.2 Comparison with simulated dose rates

Zeltweg is situated at the coordinates $47°\,11'26''N;\ 14°\,45'4''O$, which corresponds to a vertical cutoff rigidity of $4.4\ \mathrm{GV}$. The modulation potential during September 2014 was $607\ \mathrm{MV}$. These parameters were used to simulate the dose rates at both flight altitudes in order to verify the quality of the simulation model. The results of the simulation are compared to the measured values in Table 13.

Table 13: Comparison of results from TEPC flight measuremet in Zeltweg (September 2014) with simulated values

	$\dot{H}^*(10)\ TEPC$ [µSv/h]	$\dot{H}^*(10)\ Simulation$ [µSv/h]	$Deviation\ from\ measurement$
$FL400$	5.4 ± 0.7	5.1 ± 1.0	-6.8%
$FL450$	7.4 ± 1.1	5.9 ± 1.2	-20.1%

The results that were delivered by the simulation model agree with the values from the TEPC-measurement and lie within the margin of error. At the considered altitudes, the simulation does not exceed a deviation of 30 %.

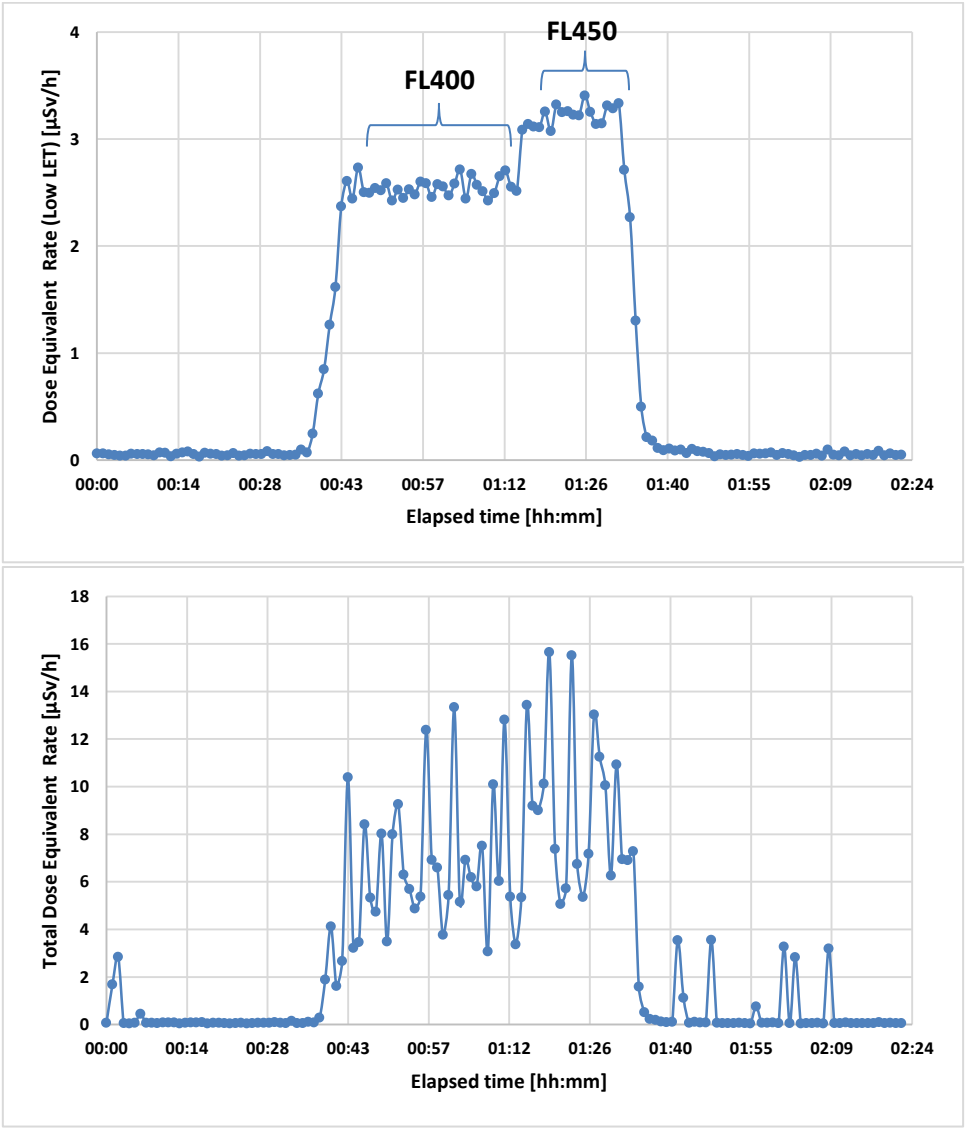

Figure 32: Dose Equivalent Rate during the measurement flight of the low LET channel (top) and total dose rate including high LET channel (bottom)

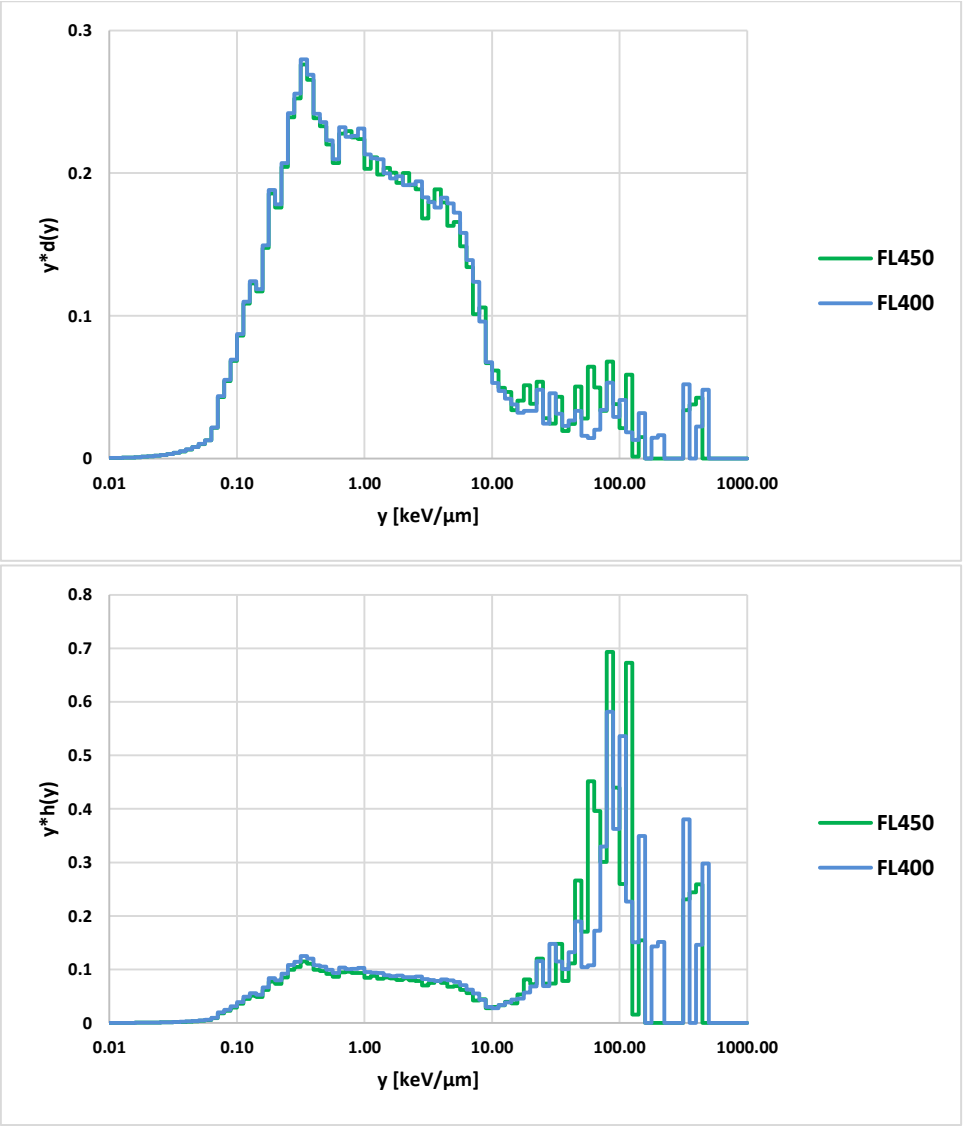

Figure 33: Dose distribution (top) and distribution of dose equivalent (bottom) for measurement flight at altitudes $FL400 \triangleq 12.2$ km and $FL450 \triangleq 13.7$ km

5 Simulation results for dose rates caused by solar cosmic radiation

Up until now, only the GCR component of the cosmic radiation has been considered. This component has the big advantage, that apart from the slow changes over the solar cycle it is rather constant, which makes it predictable and therefore a lot easier to deal with than the second component, which is the solar cosmic radiation. The SCR was described in section 2.1.2 and can lead to severe dose rate increases due to the elevated low-energy flux of the SCR proton spectrum. Hence, the SCR mainly raises the radiation exposure in northern and southern polar regions. The biggest difficulty in calculating the dose rates arising from solar events is the determination of the energy spectrum, as it varies from event to event and in addition has a time dependence in the course of the GLE itself. The reconstruction of the SCR spectra using data from ground based neutron monitors was described in section 3.3.1.2 on page 28. This chapter presents simulation results for dose rates during some selected GLEs.

5.1 Simulated dose rates during historic solar particle events at flight altitudes

A complete list of ground level enhancements recorded by the *Oulu Cosmic Ray Station* can be found in Table 1 on page 5. Three of the most powerful events were selected for a closer analysis. These are GLE31 from May 1978, GLE42 from September 1989 and GLE69 from January 2005 with a count rate increase of 84 %, 174 % and 269 % respectively. The proton spectra during the maxima of the GLEs were calculated using the neutron count rate from the peak increase and a subsequent evaluation of equation (33) and (34). Two spectra were calculated for each GLE, a hard one with $\gamma = 4$ and a soft one with $\gamma = 7$. Afterwards, the resulting proton spectra were used as input for the simulation model. The impact of these events on the radiation exposure is analysed in the further course.

5.1.1 GLE31

GLE31 occurred on 7th May 1978 and lasted for approximately 90 minutes. The evolution of the increase in neutron count rate is mapped in Figure 34. It took only 15 minutes from the onset of the GLE to reach the maximum intensity. The peak of the GLE corresponds to an increase in count rate of 74 c/s above the count rate caused by GCR alone. After roughly 10 minutes, the count rate started to decrease again and reached the baseline after approximately an hour.

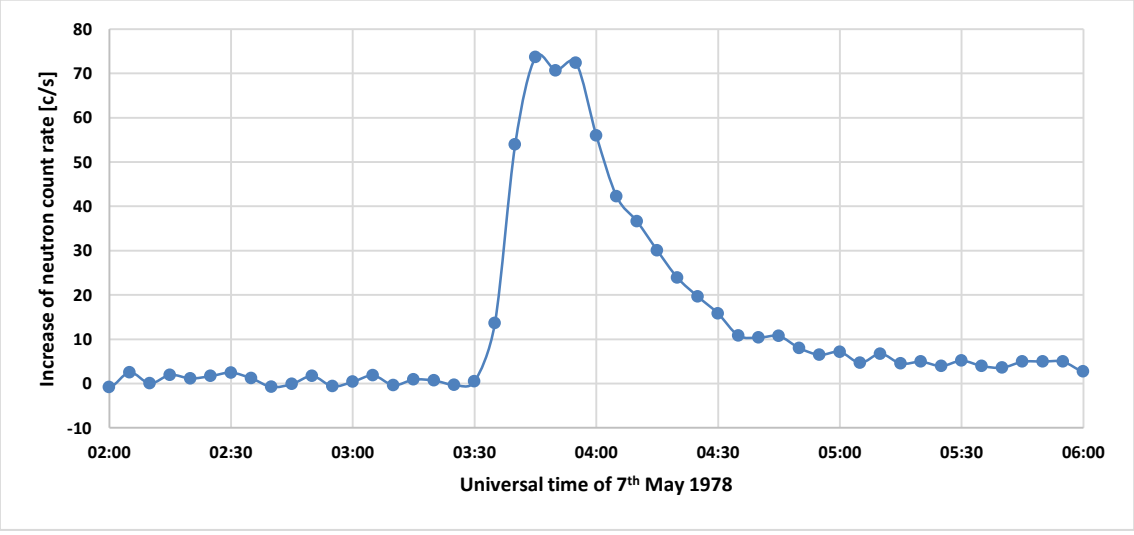

Figure 34: Evolution of count rate increase during GLE31 on 7th May 1978 (data from OULU cosmic ray station)

The results are presented in two-dimenional dose maps in Figure 36 and in a three-dimensional diagram in Figure 35, where the dose rates are distributed according to their geographical longitude and latitude. Both figures show the minimum and the maximum ambient dose equivalent ratest at an altitude of 10.67 km that arise from the hard and the soft primary proton spectra using the two previously discussed slopes.

It is immediately obvious that the radiation exposure during solar flares must not be underestimated. Very high dose rates with values above 200 µSv/h are expected for the polar regions, where the magnetic shielding is very weak. However, the immediate radiation hazard is confined to areas above roughly 50° northern and southern latitude. There is a dramatic decrease in dose rate when moving towards the equator, because the flare is effectively blocked out of regions with even relatively low magnetic cutoff rigidities. Starting from a cutoff value of approximately 0.3 GV, which corresponds to northern or southern latitudes between 70° and 80°, the dose rate drops rapidly until it is negligible below a latitude of about 40°. In equatorial regions, the dose rates are not expected to exceed 0.2 µSv/h, which is by about a factor 10 smaller than what is expected to be caused by GCR. It is important to stress that the extreme dose rates in Figure 36 and Figure 35 correspond the peak intensity of the GLE, which lasted only several minutes.

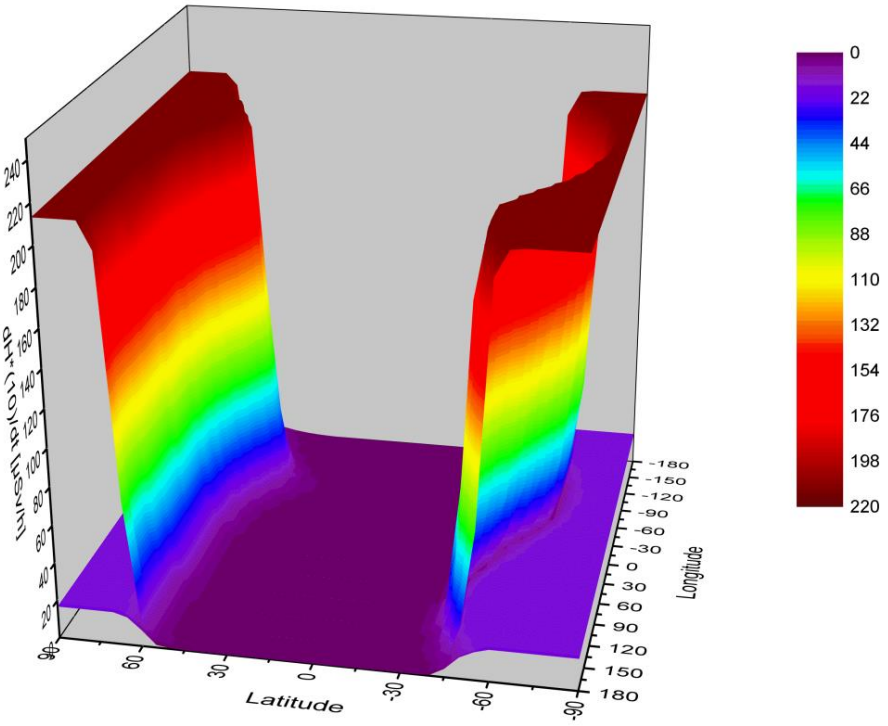

Figure 35: Minimum and maximum ambient dose equivalent rate in µSv/h for maximum of GLE31 at altitude $FL350 \triangleq 10.67$ km

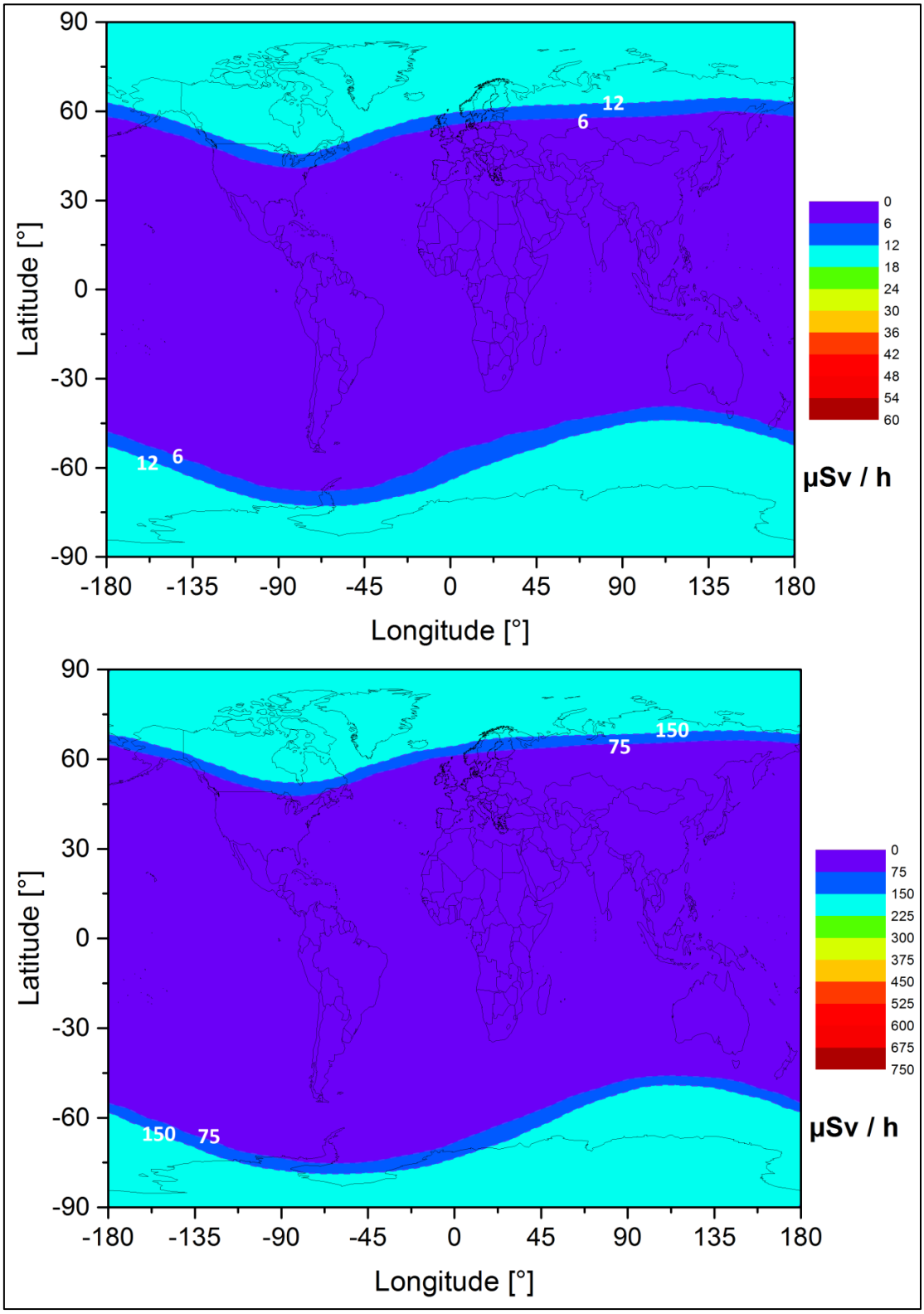

Figure 36: **Map of minimal (top) and maximal (bottom) expected ambient dose equivalent rate in µSv/h during maximum intensity of GLE31 at altitude $FL350 \triangleq 10.67$ km**

5.1.2 GLE42

GLE42 took place from 29th to 30th December 1989 and was the second strongest GLE ever recorded by the *Oulu Cosmic Ray Station.* The increase in neutron count rate during the event is depicted in Figure 37. The peak increase was a little over 160 c/s, thus more than twice as strong as GLE31. Moreover, it did not last mere 90 minutes, as it was the case for GLE31, but even more than 8 hours.

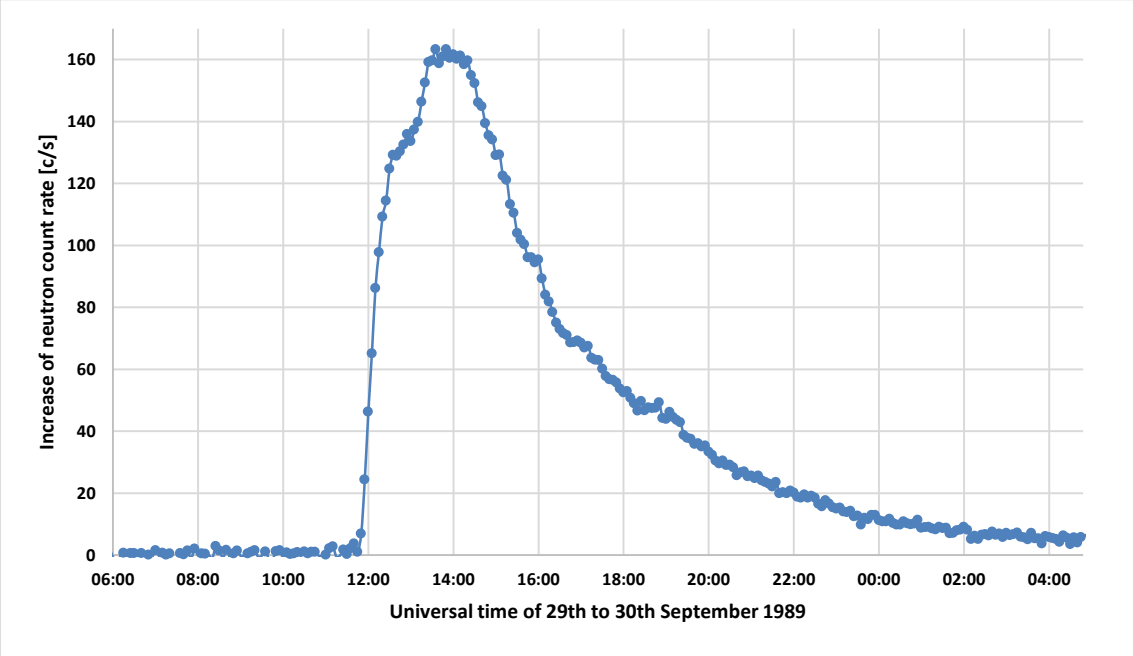

Figure 37: Evolution of count rate increase during GLE42 from 29th to 30th September 1989 (data from OULU cosmic ray station)

Figure 38 and Figure 39 show the simulated radiation exposure in ambient dose equivalent rate in a three- and two-dimensional representation. Three time steps are depicted in Figure 38, the onset, the maximum and the fade out of the GLE. During the maximum of the event, a dose rate of up to 470 µSv/h can be expected in the polar regions. Apart from the higher dose rates, the results look very similar to those from GLE31. Starting from northern and southern latitudes between 70° and 80°, the dose rates drop rapidly toward equatorial regions where a dose rate of 0.5 µSv/h is not exceeded. This thin transition area is best seen in Figure 39, where the contour lines in the dose map show a decrease from 450 to 75 µSv/h within a range in latitude of only 15°. Another minor difference between the dose maps of GLE31 and GLE42 is, aside from the higher dose rates in the polar regions, that the countour lines representing the same level of radiation exposure are slightly shifted towards the equator. However, the shift is very small, not bigger than 5°.

The third time step in Figure 38 represents the dose rates during a late stage of the GLE, where the neutron count rate has subsided to a fraction of the peak intensity. It corresponds to a point in time approximately 10 hours after the onset of the GLE or 8 hours after the maximum intensity of the solar event. Still, the expected dose rate is considerably high, with values between 5 and 60 µSv/h in the polar regions, depending on the true nature of the proton spectrum. Even in the best case, the radiation exposure caused by the solar event alone is in the order of the dose rate produced by GCR. This example demonstrates that flight routes across the poles during long-lasting GLEs can lead to dramatically increased accumulated doses, which are

much higher than what would be expected from GCR. For that reason, the accumulated doses of several long-distance flights during GLE42 were calculated in section 6.1.

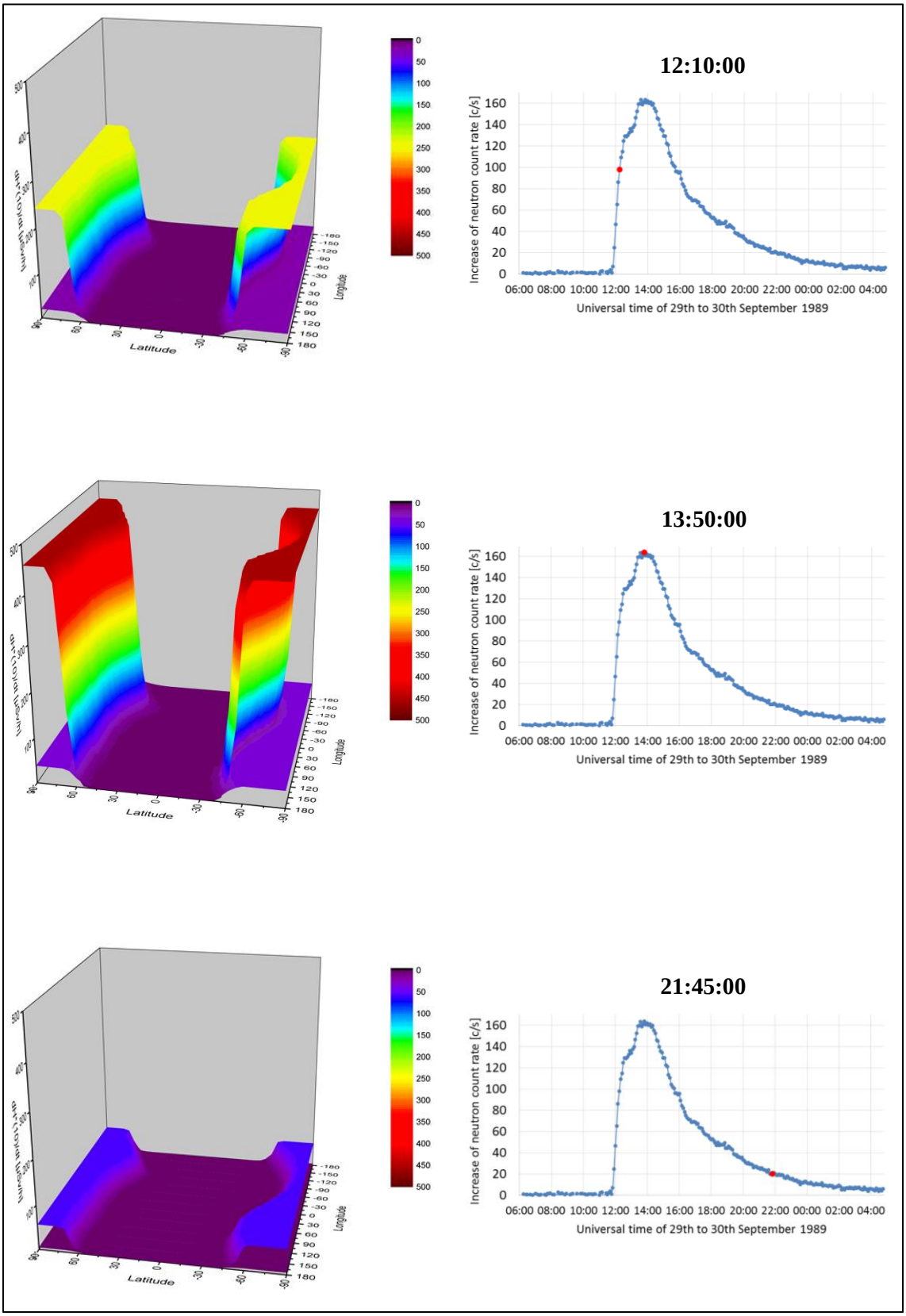

Figure 38: Minimum and maximum ambient dose equivalent rate in µSv/h for three time steps of GLE42 at altitude $FL350 \triangleq 10.67$ km

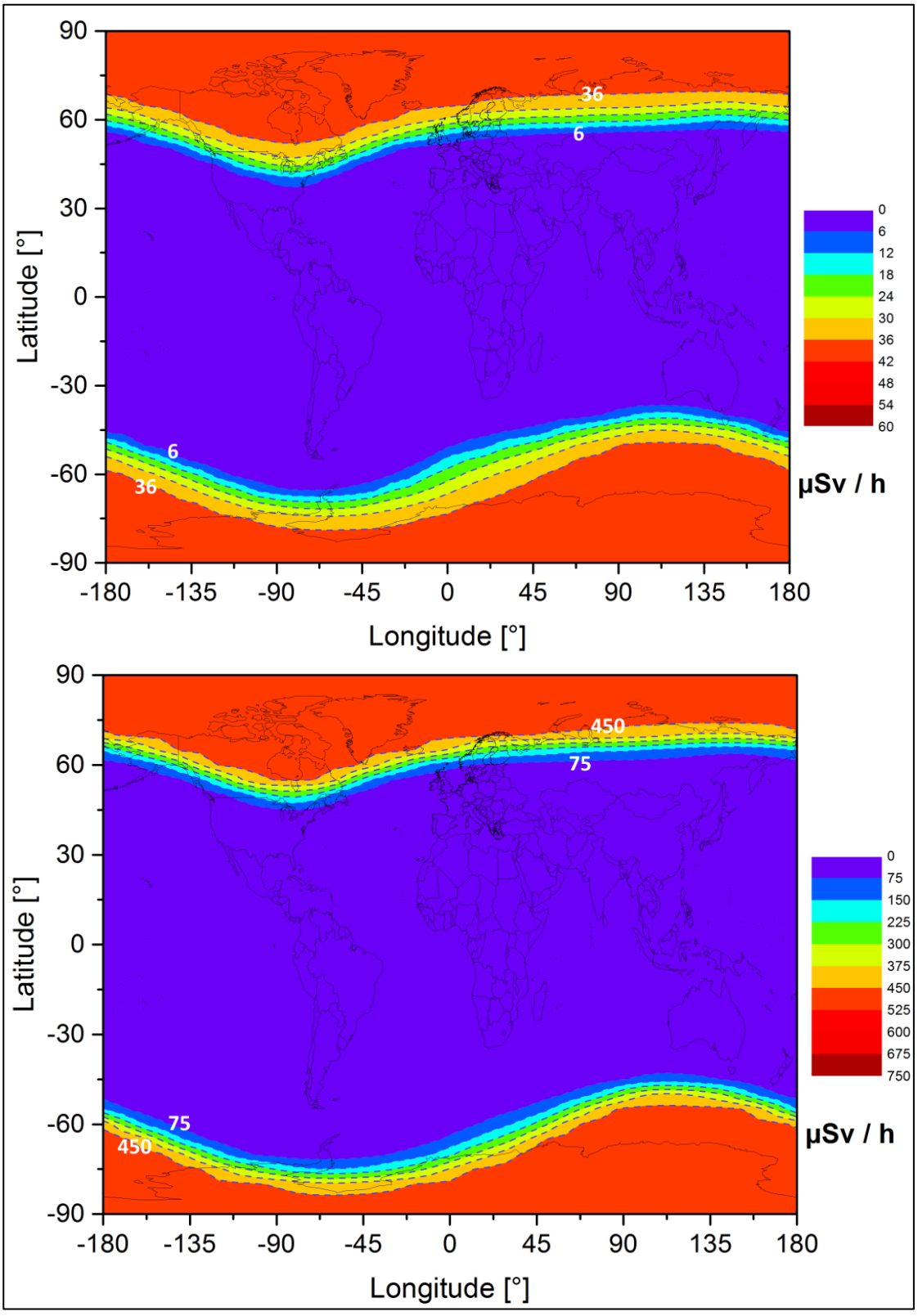

Figure 39: Map of minimal (top) and maximal (bottom) expected ambient dose equivalent rate in µSv/h during maximum intensity of GLE42 at altitude $FL350 \triangleq 10.67$ km

5.1.3 GLE69

GLE69 was recorded on 19th January 2005 by the *Oulu Cosmic Ray Station* with an unprecedented high increase in neutron count rate. Within 15 minutes the count rate increased by 250 c/s. After the peak increase, the count rate immediately started to drop down again and recovered to the original value within approximately 4 hours. The whole evolution of the GLE is depicted in Figure 40.

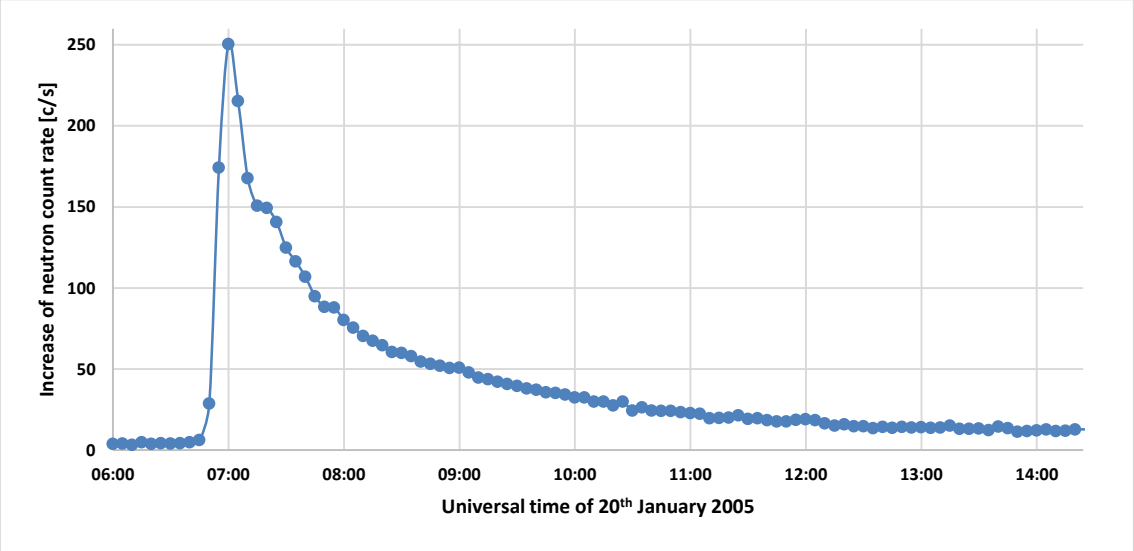

Figure 40: Evolution of count rate increase during GLE69 on 20th January 2005 (data from OULU cosmic ray station)

The minimum and maximum ambient dose equivalent rate during the peak intensity of the GLE at an altitude of 10.67 km is presented in Figure 41 and Figure 42. The distribution of dose rates according to the geographical position shows the same characteristics as GLE31 and GLE42, but the dose rates in the polar regions are even higher due to the extreme peak increase. Here, values between 60 and 725 µSv/h are expected to be reached. At the equator, the dose rate is only 0.7 µSv/h. However, the peak intensity lasts for a much shorter time than it was the case for GLE42.

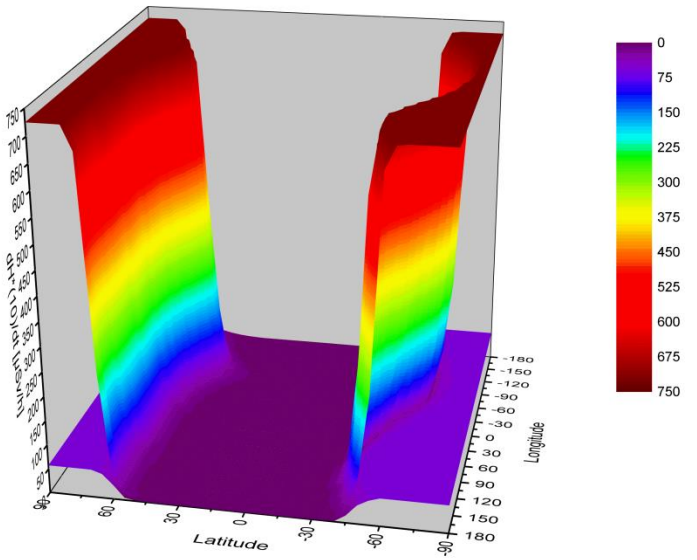

Figure 41: Minimum and maximum ambient dose equivalent rate in µSv/h for maximum of GLE69 at altitude $FL350 \triangleq 10.67$ km

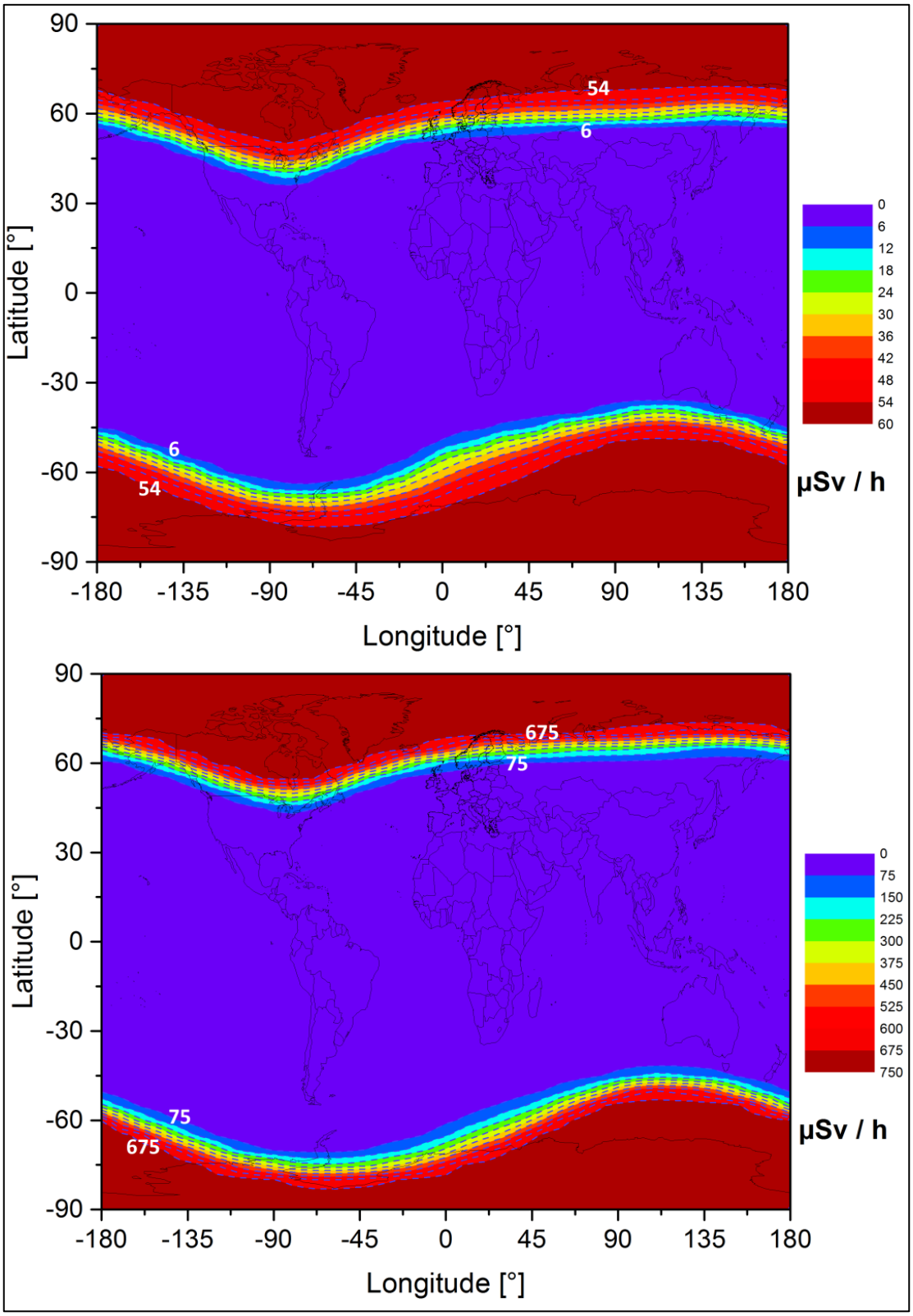

Figure 42: Map of minimal (top) and maximal (bottom) expected ambient dose equivalent rate in µSv/h during maximum intensity of GLE69 at altitude $FL350 \triangleq 10.67$ km

Figure 43 compares the maximum and minimum dose rates during GLE31, GLE42 and GLE69 along the prime meridian at an altitude of 10.67 km (FL350).

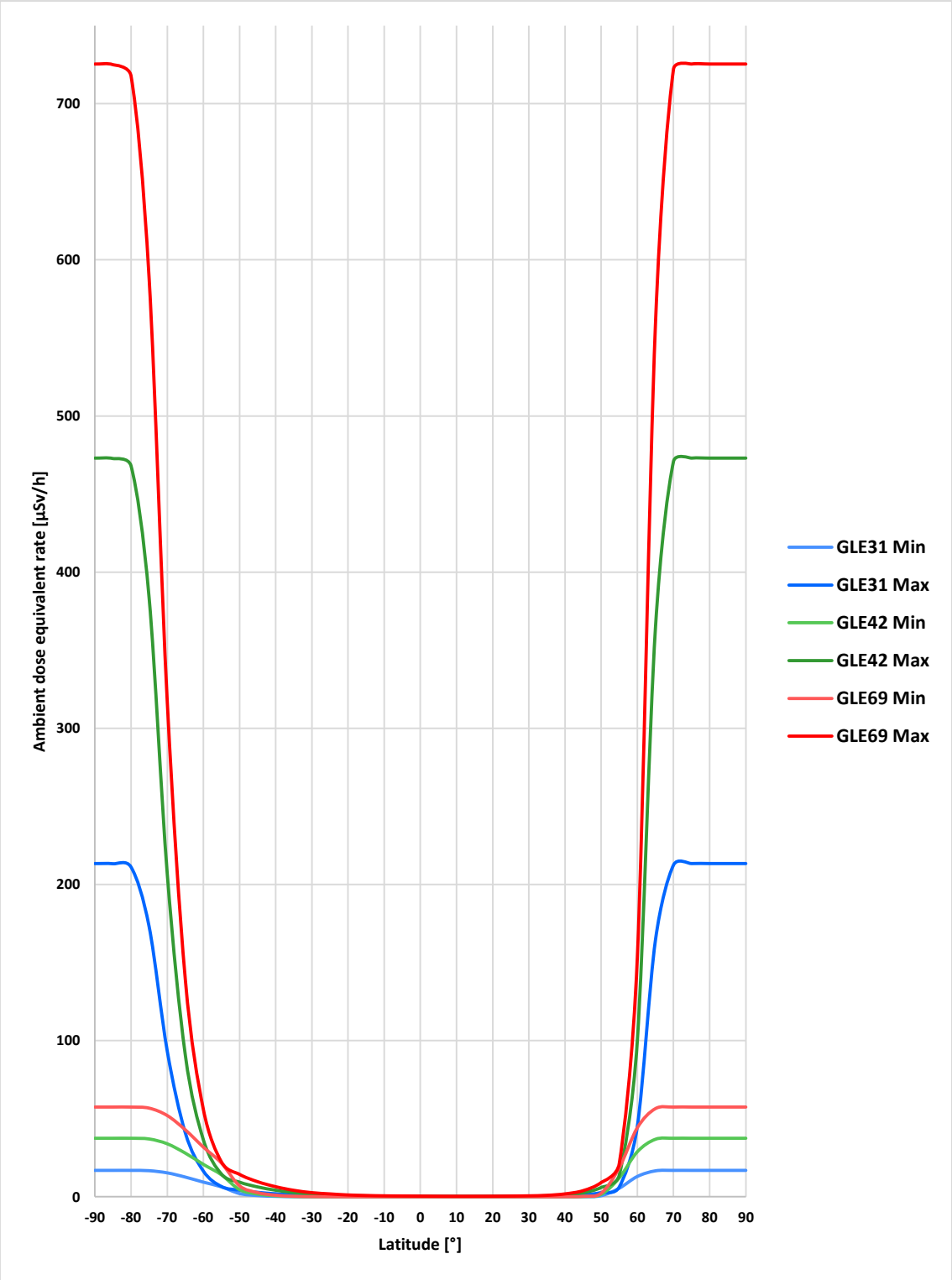

Figure 43: Summary of GLE31, GLE42 and GLE69 during maximum increase at altitude $FL350 \triangleq 10.67$ km

6 Implication of galactic and solar cosmic radiation on commercial air flights

The characteristics of galactic and solar cosmic radiation as well as its effect on the atmospheric radiation exposure were presented in the previous chapters. In this chapter, the impact of GCR and SCR is compared. Later on, the simulation model is used to assess the threat that GCR and SCR pose to passengers and crew members on commercial air flights.

In contrast to the steady galactic component of the cosmic radiation, the solar component only strikes the Earth very sporadically. One of the main aspects in assessing the radiation harzard of GLEs is to look at their frequency of occurrence. Figure 44 displays the distribution and the strength of all GLEs recorded by the *Oulu Cosmic Ray Station* since 1966 (see also Table 1).

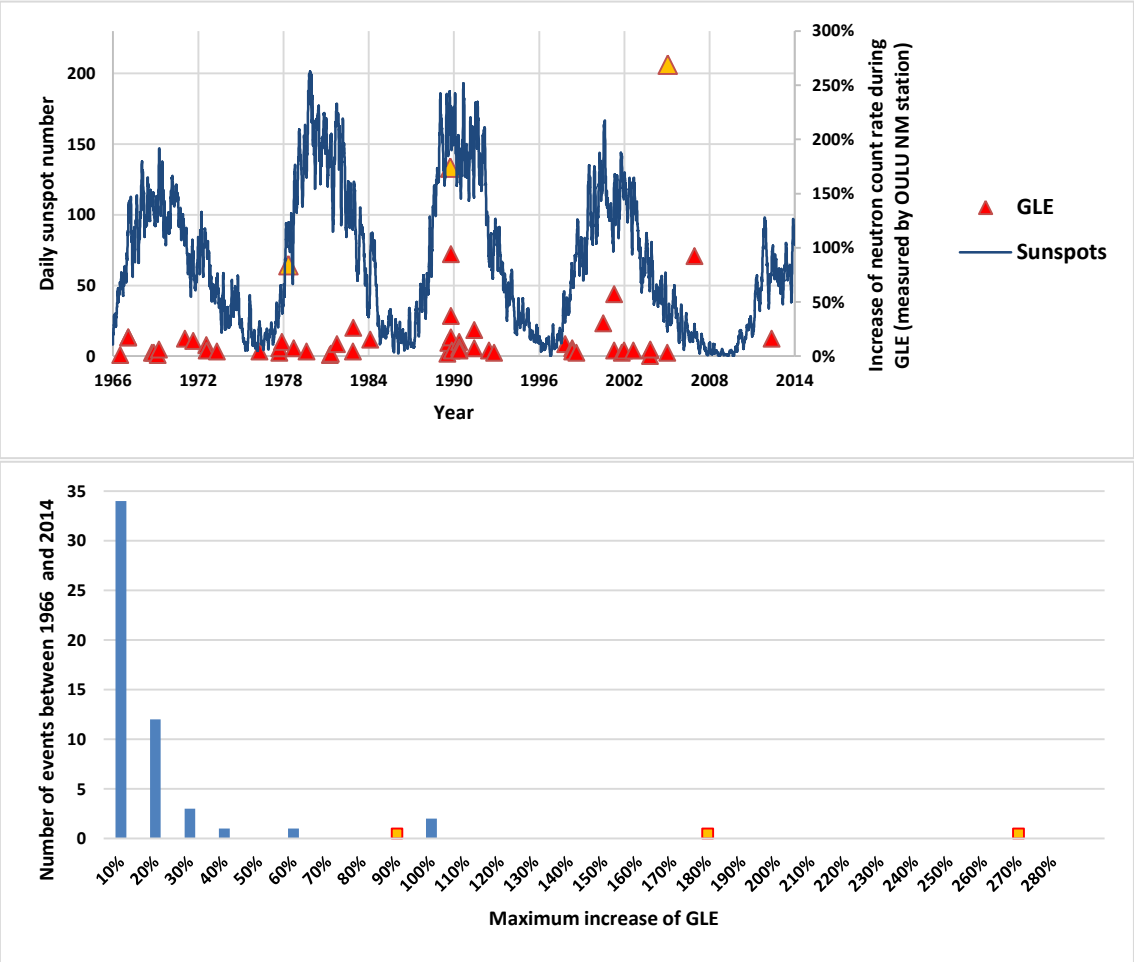

Figure 44: Top: Distribution of GLE events along solar cycles; Bottom: Histogram for the frequency of GLEs with respect to their strength (from 1966 to 2014); yellow markers correspond to GLE31, GLE42 and GLE69, which were discussed in chapter 5.1; (GLE data from *Oulu cosmic ray station*, sunspot data from [4])

Obviously, a GLE is a rather rare phenomenon, which happens on average once per year. Extremly powerful events, like those analysed in the previous chapter, only take place approximately once per solar cycle. From the overall 57 solar events since 1966, only 8 exceeded the 30 % mark. Nonetheless, the earlier analysis demonstrated, that the expected dose rates during GLEs in the polar regions are extremely high, so that the legal limit of radiation exposure, which is 1 mSv of effective dose, can be exceeded. Therefore, solar erruptions should

be considered in the health policy for aircraft personel. The global network of neutron monitors allows a realtime surveillance of solar activity and could be used to warn against GLEs when an onset is registered.

Another important aspect, which distinguishes GCR- from SCR-induced radiation doses is their dependence on the geographical position on Earth. In order to understand, how the different proton spectra behave when they encounter the magnetic field, it is necessary to look at which particles can penetrate at the local magnetic cutoff rigidity and which particles are deflected. Figure 45 shows both the soft and the hard spectrum during the maximum of GLE42 and also the GCR spectrum, reconstructed using the modulation potential from December 1989, when the GLE took place. The dashed vertical lines represent the cutoff rigidity values from 1 to 17 GV and indicate, which part of the spectrum is blocked out of the magnetosphere. By cancelling the flux below one of the marking lines, the main flux of the SCR disappears. The soft SCR spectrum is more affected than the hard one, while the GCR spectrum is the least affected. This is the reason why GLEs have their highest impact in the polar regions and are more or less negligible near the equator.

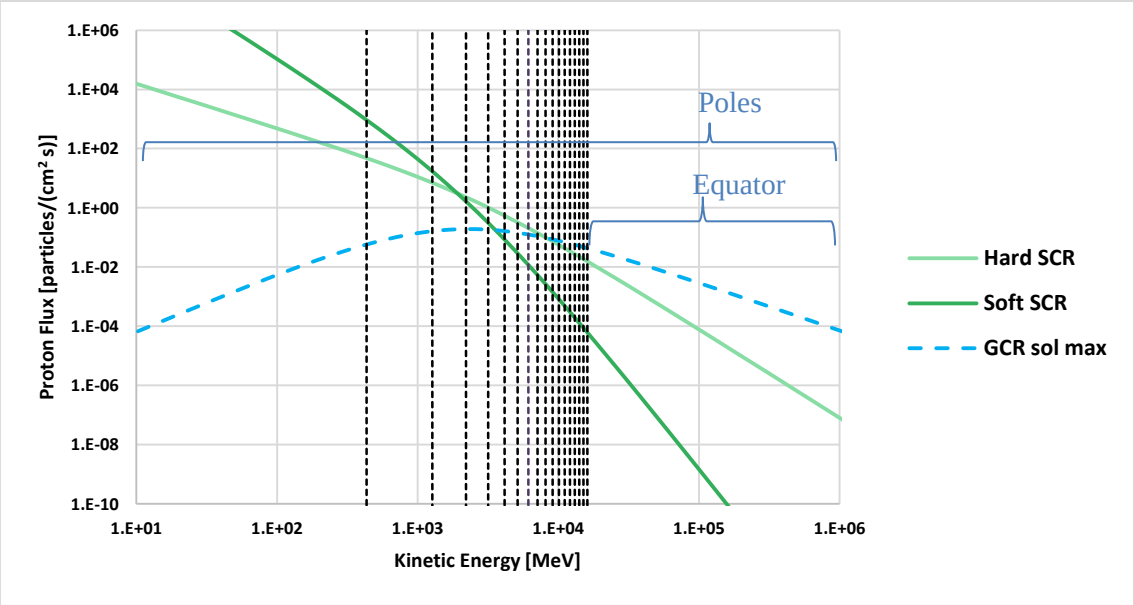

Figure 45: SCR proton spectra for GLE42 during maximal intensity for $\gamma = 4$ and $\gamma = 7$ compared with GCR proton spectrum from December 1989 ($\phi = 1152$ MV); the vertical dashed lines show the cuts of the spectrum from 1 to 17 GV (left to right)

Figure 46 demonstrates the cutoff rigidity dependence for GCR- and SCR-induced dose rates by the example of GLE42. Clearly, dose rates originating from GCR depend a lot less on cutoff rigidity as it is the case for SCR. The GCR dose rate is reduced to half of its original value at a cutoff rigidity of approximately 9 GV. At the maximum rigidity value of 17 GV, which corresponds to a position near the equator, still more than 30 % of the original dose rate survives. The case of SCR looks very different. Here, the dose rate is reduced to half at a rigidity of less than 1 GV in the case of the soft spectrum and less than 2 GV in the case of the hard spectrum. The dose rates vanish completely towards higher rigidity values.

The whole radiation budget during the peak of the GLE42 event including the solar and the galactic component is plotted in Figure 47. It shows the proportion of the dose rates produced

by the three proton spectra in Figure 45. The GCR component dominates low latitude regions, while the SCR component dominates the polar regions.

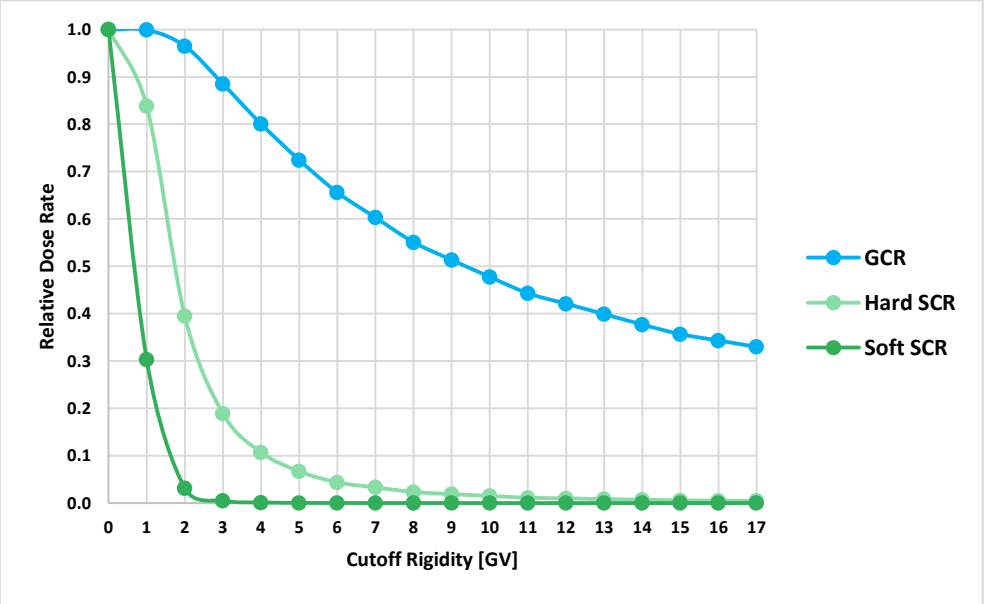

Figure 46: Dependence of dose rate on cutoff rigidity for GCR ($\phi = 1152$ MV) and SCR ($\gamma = 4$; $\gamma = 7$) during maximum intensity of GLE42, normalised to dose rate at cutoff $R_C = 0$ GV; $FL350 \triangleq 10.67$ km

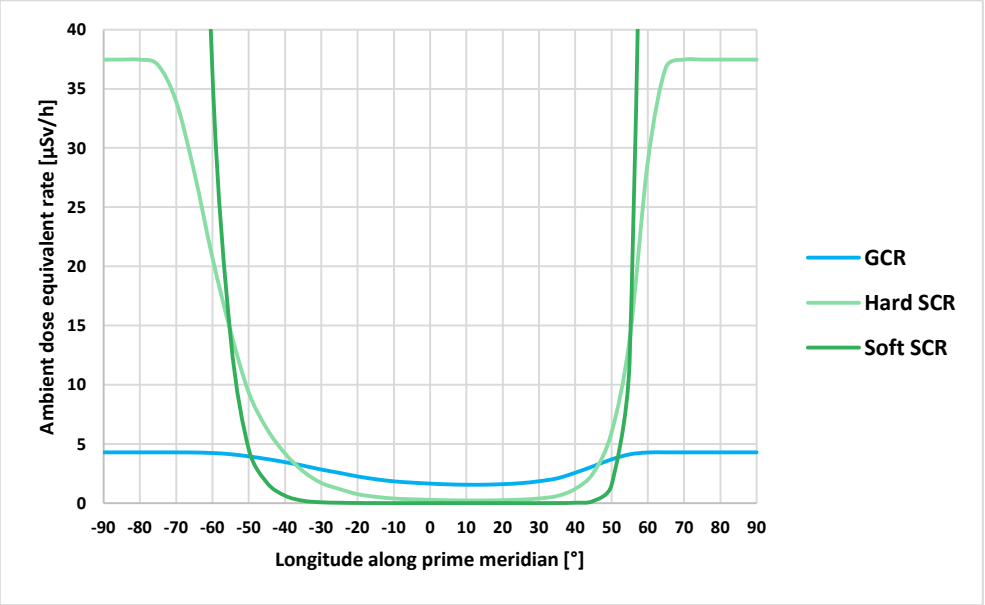

Figure 47: Maximum and minimum dose rates at altitude $FL350 \triangleq 10.67\,km$ during peak intensity of GLE42 compared with dose rates produced by GCR; the corresponding proton spectra are plotted in Figure 45

6.1 Simulated flights during GLE42

Four long-distance flight routes were picked out for the simulation of accumulated doses during the GLE42 event. One each across extreme northern and southern regions, one in mid-latitudes and one in low-latitudes. The flight routes are sketched in Figure 48. The time of the onset of the GLE was chosen in such a way that it coincides with the takeoff of the airplane. Each time

step during the simulation is defined by longitude, latitude, altitude, vertical cutoff rigidity and the proton spectrum of the GLE, which in turn depends on the increase of neutron cout rate. The simulation was performed three times per flight, once each for the hard and the soft SCR spectrum ($\gamma = 4$ and $\gamma = 7$) and once for GCR with a modulation potential of $\phi = 1152$ MV. The SCR results are given as minimum and maximum values. Eventually, the time series of dose rates were multiplied by the time increment and added up in order to gain the accumulated doses of the flight routes.

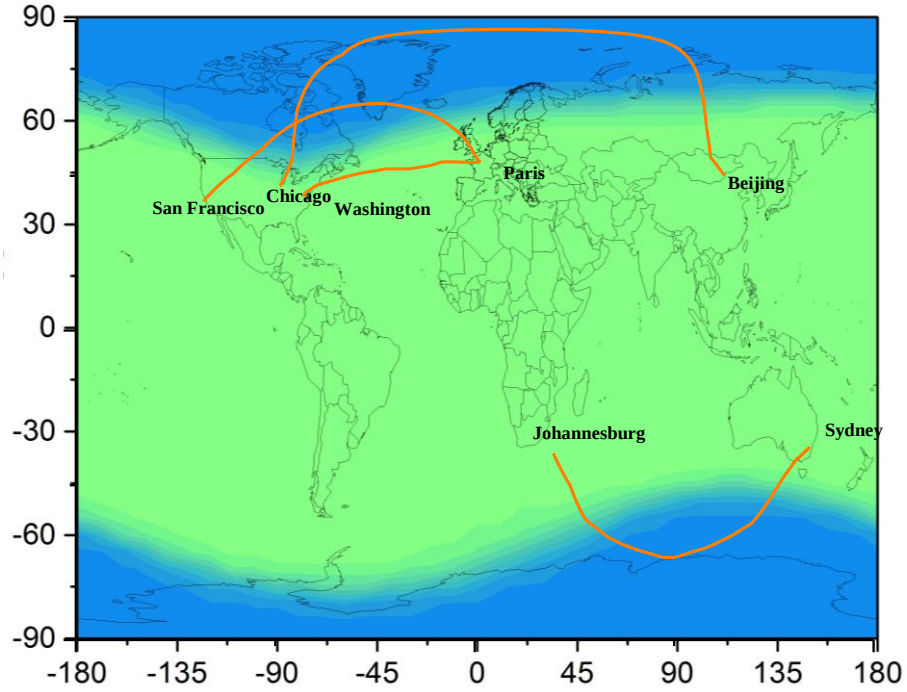

Figure 48: Flight routes for simulation of accumulated doses during GLE42

6.1.1 Chicago → Beijing

The chosen flight from Chicago to Beijing lastet 13 hours and 11 minutes and covered a range of latitude from 40° to 88°. This corresponds to a mean vertical cutoff rigidity of 1.6 GV. The averaged altitude from takeoff to landing is 327 (~10 km). The simulated accumulated doses during the entire flight period are listed in Table 14.

Table 14: Accumulated ambient dose equivalent on flight Chicago-Beijing during GLE42

	$H^*(10)$ [µSv]
SCR minimum	144
SCR maximum	1515
GCR	46

The simulation shows that the minimum accumulated dose caused by SCR is expected to be three times higher than what is expected from GCR alone. The maximum dose that can be expected reaches a total of more than 1.5 mSv, which is extremely large. The dose rate profiles during the flight are depicted in Figure 49.

6.1.2 San Francisco → Paris

The flight form San Francisco to Paris had a mean flight altitude of $FL356$ ($\sim$10.9 km) and lastet 9 hours and 15 minutes. The flight route lies in a range of latitude between 38° to 66°, which corresponds to a mean vertical cutoff rigidity of 1.2 GV. The simulated dose rates for the SCR and GCR component are listed in Table 15.

Table 15: Accumulated ambient dose equivalent on flight San Francisco-Paris during GLE42

	$H^*(10)$ [µSv]
SCR minimum	169
SCR maximum	1746
GCR	42

Even though the duration of the flight is about 4 hours shorter than the flight from Chicago to Beijing, the accumulated doses are higher. The reason for this is the higher flight altitude and the higher cutoff rigidities in the Asian region. The minimum expected dose that is accumulated during the flight and is produced by the GLE is approximately four times higher than the dose from GCR. Figure 50 shows the corresponding dose rate profiles during the flight.

6.1.3 Sydney → Johannesburg

Flight Sydney-Johannesburg took 13 hours and 45 minutes on a mean flight altitude of 332 ($\sim$10.1 km). The flight route was located in a range of southern latitude between -26° and -66°, which leads to a mean vertical cutoff rigidity of 1.9 GV. Table 16 lists the accumulated doses that were calculated from the SCR and GCR spectra.

Table 16: Accumulated ambient dose equivalent on flight Sydney-Johannesburg during GLE42

	$H^*(10)$ [µSv]
SCR minimum	106
SCR maximum	972
GCR	50

The accumulated doses are slightly smaller than in the previous two flights, because of the higher cutoff rigidities. Still, the accumulated dose from the GLE event is at least twice as big as the dose from the GCR component. The simulated dose profiles during the flight are depicted in Figure 51.

6.1.4 Paris → Washington

The 7 hours and 43 minute flight from Paris to Washington was chosen because it avoids high latitudes. The flight path lies within a latitude of 39° and 49°, which corresponds to a mean cutoff rigidity of 2.7 GV. The averaged flight altitude is $FL365$ ($\sim$11 km). Table 17 lists the results for the simulation of the accumulated doses.

Table 17: Accumulated ambient dose equivalent on flight Paris-Washington during GLE42

	$H^*(10)$ [µSv]
SCR minimum	33
SCR maximum	55
GCR	34

This example shows very well the latitude dependence of the SCR induced dose rates. The dose rates are a lot smaller than during the previously discussed flight routes, even though the flight altitude is higher.

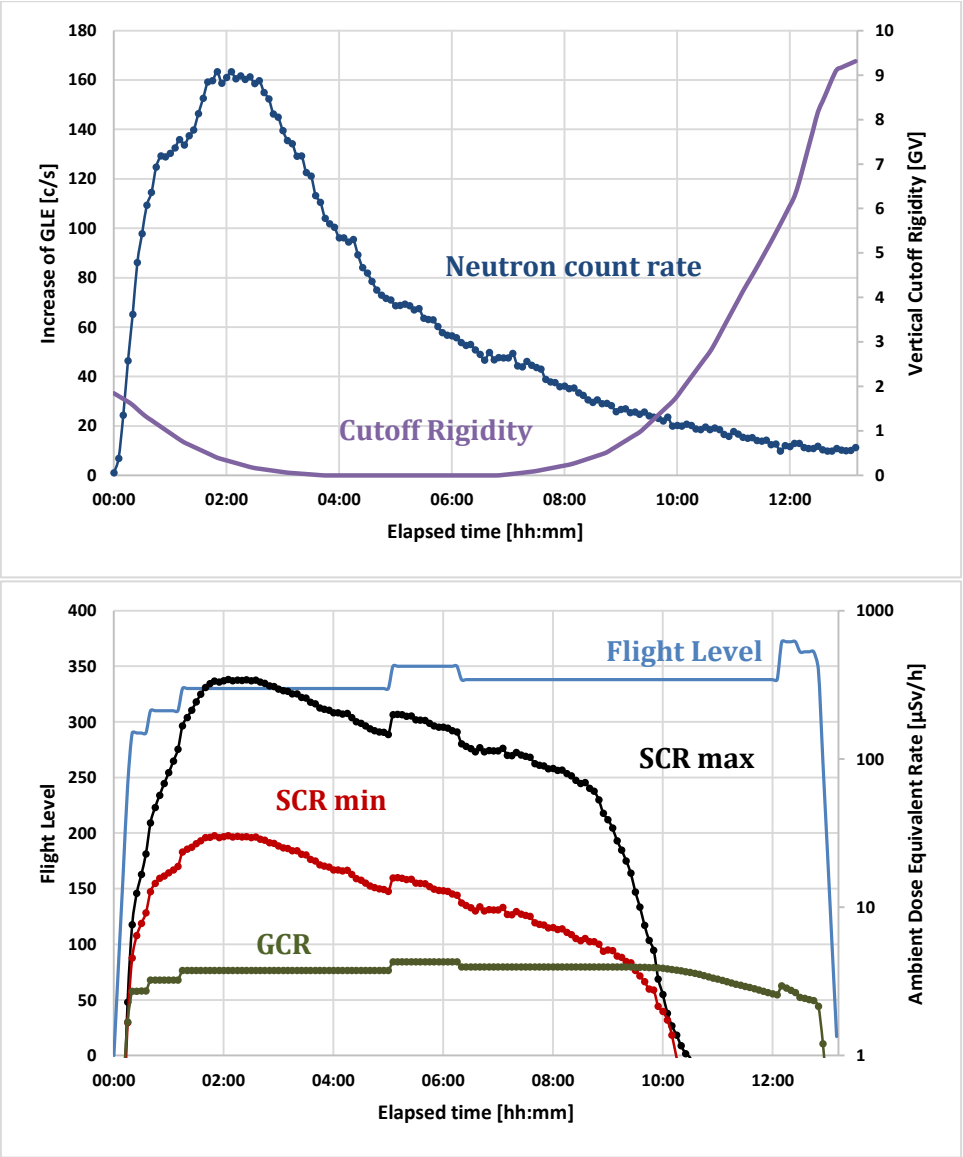

Figure 49: Dose rates during flight from Chicago to Beijing at the time of GLE42; Top: Profile of neutron count rate during GLE and cutoff rigidity at the location of the airplane; Bottom: Maximum and minimum dose rate expected from SCR and dose rate produced by GCR

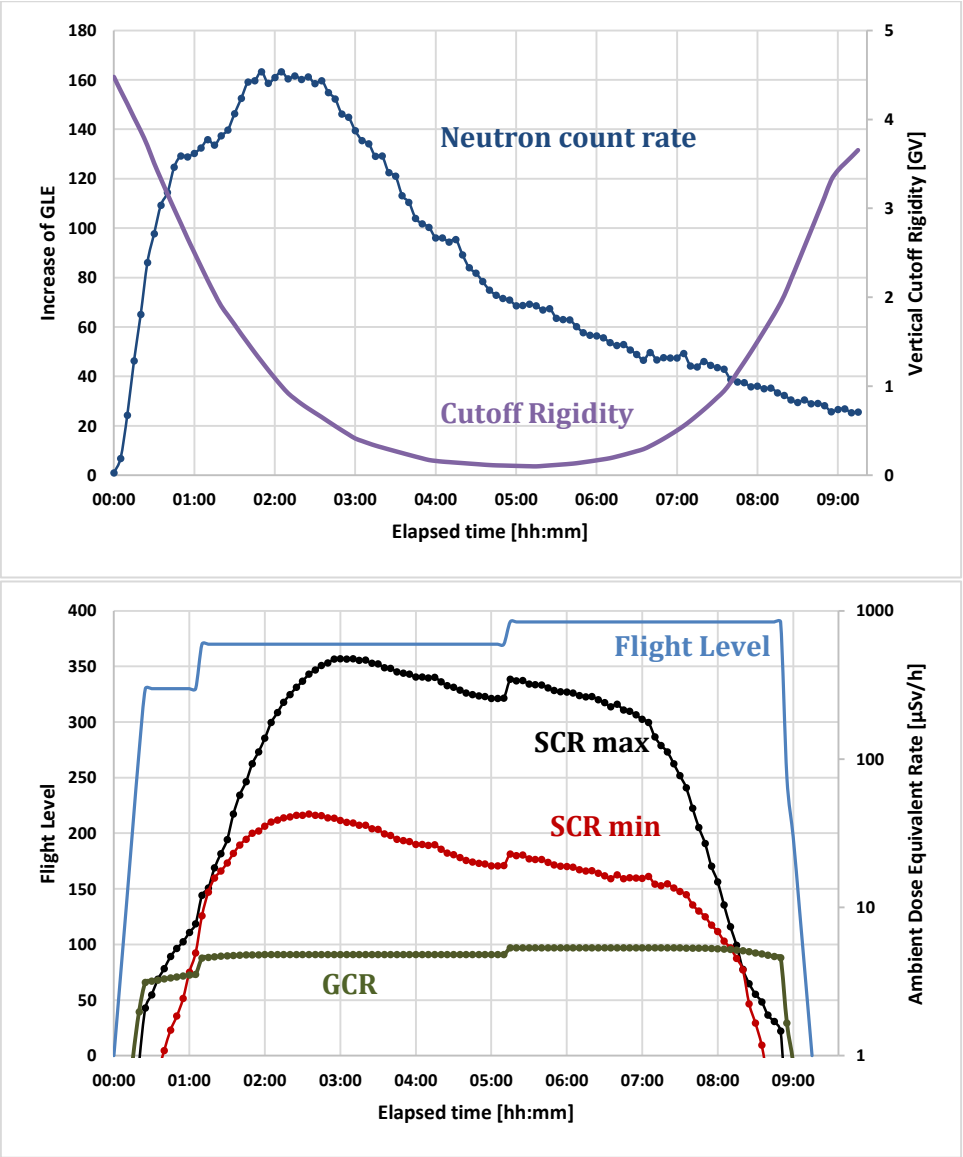

Figure 50: Dose rates during flight from San Francisco to Paris at the time of GLE42; Top: Profile of neutron count rate during GLE and cutoff rigidity at the location of the airplane; Bottom: Maximum and minimum dose rate expected from SCR and dose rate produced by GCR

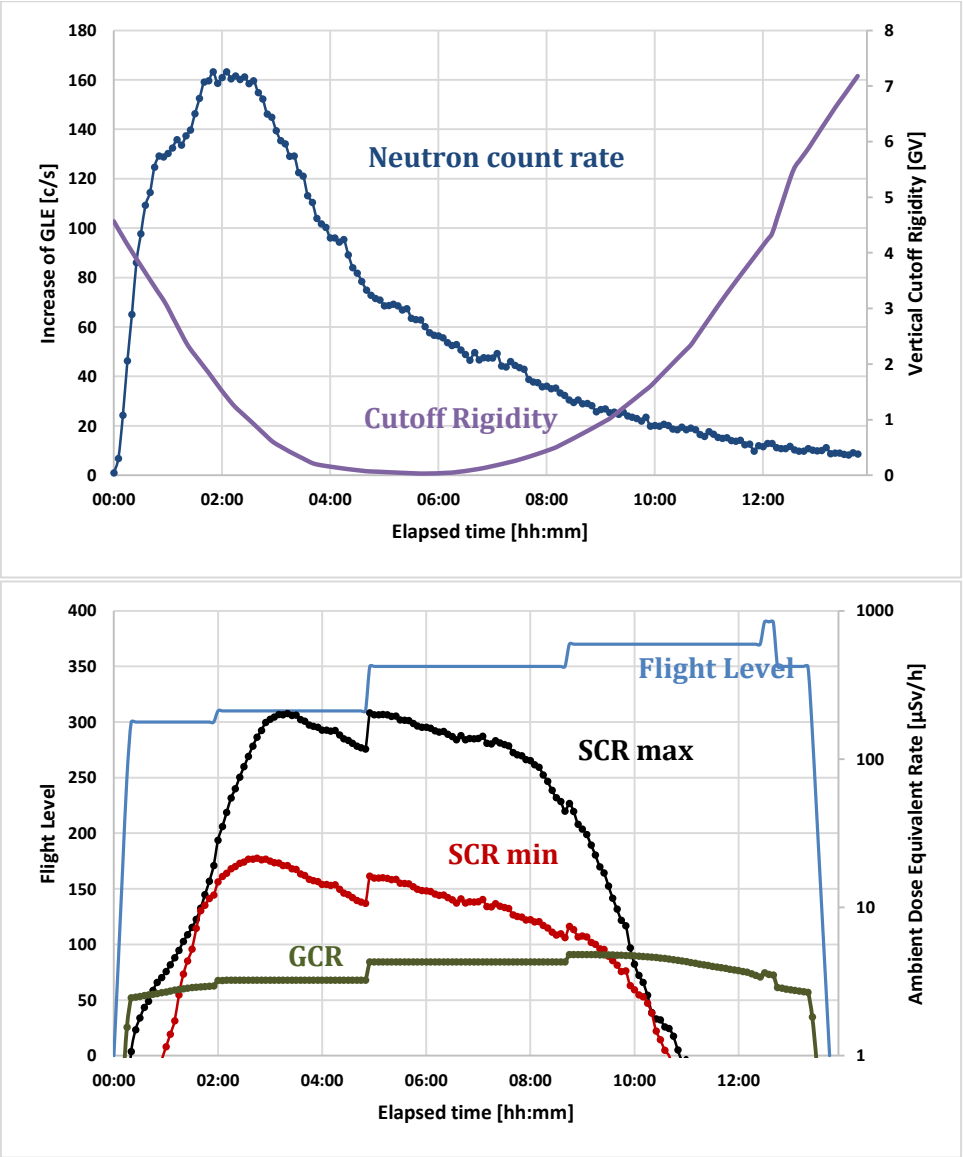

Figure 51: Dose rates during flight from Sydney to Johannesburg at the time of GLE42; Top: Profile of neutron count rate during GLE and cutoff rigidity at the location of the airplane; Bottom: Maximum and minimum dose rate expected from SCR and dose rate produced by GCR

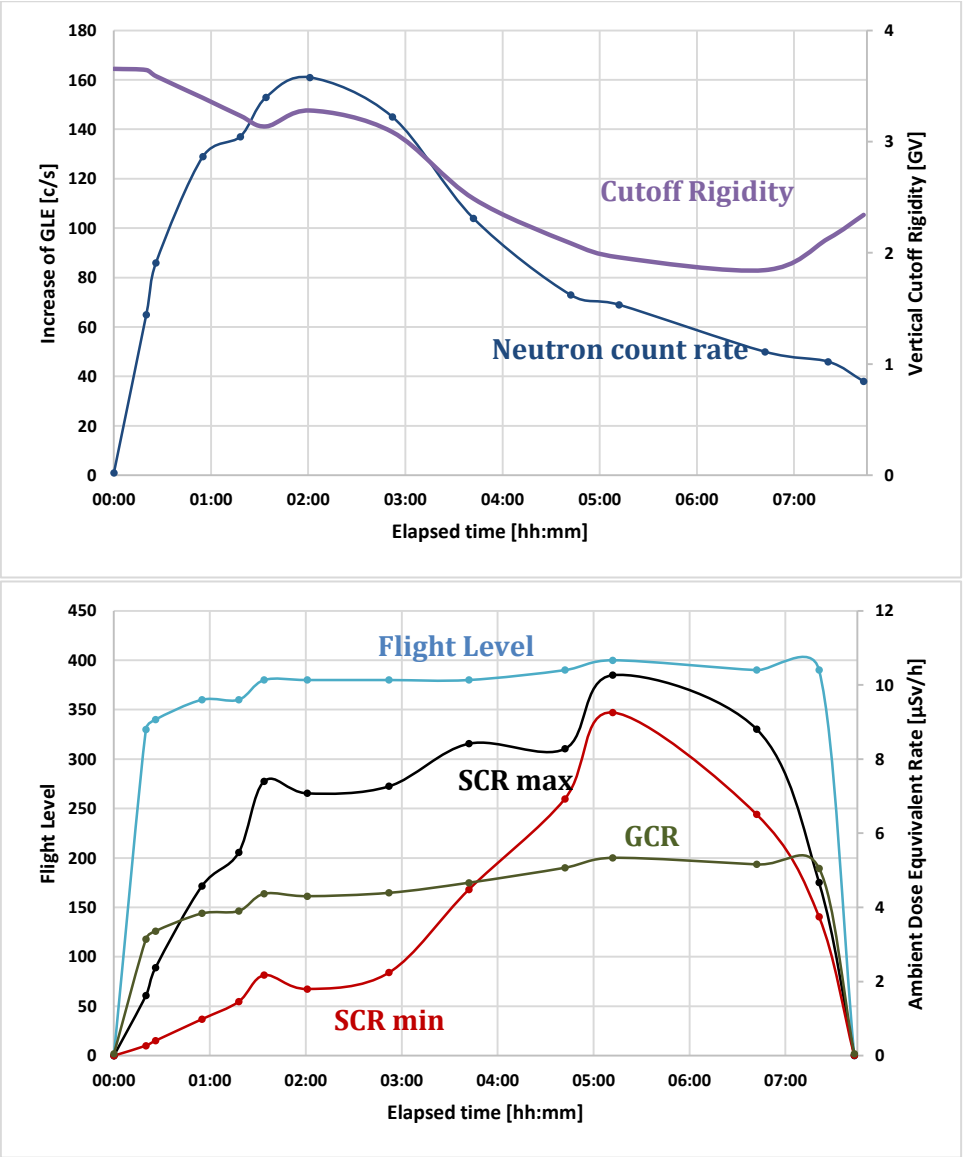

Figure 52: Dose rates during flight from Paris to Washington at the time of GLE42; Top: Profile of neutron count rate during GLE and cutoff rigidity at the location of the airplane; Bottom: Maximum and minimum dose rate expected from SCR and dose rate produced by GCR

7 Conclusion and Summary

The main result of this work is an

- *easy-to-use computer application* that allows a
- *rapid and even real-time assessment of the radiation dose rates in the atmosphere.*

The model is valid for an altitude range reaching from the ground level up to an altitude of 100 km. The model has to meet a multitude of requirements. On the one hand, it has to consider

- *the variation of the radiation exposure due to the magnetic field* and also
- *the height-dependence that is caused by atmospheric shielding.*

On the other hand, it has to be

- *applicable both to galactic and solar cosmic radiation.*

For this purpose, the spectra of these types of radiation have to be modelled, which is a key factor for the accuracy of the results.

The possibility of a *real-time dose assessment* was realised by *pre-calculating* the results for small energy intervals with unitary proton fluxes. This procedure is very time-consuming, but once all the information is stored in a matrix, the end result is easily obtained by weighting the matrix with any desired input spectrum.

The proton spectrum of the galactic cosmic radiation was reconstructed using the "force field model" of *Gleeson and Axford (1968).* This model depends on only one parameter (i.e. the modulation potential ϕ), which describes the periodic change of the spectrum during a solar cycle. A difficulty here lies in the choice of the correct potential. There exists a variety of different models in the literature that all give similar, but still slightly different parameters. Therefore, one has to make sure to use the appropriate potential that is compatible with the model.

The solar cosmic ray spectrum is calculated from the *increase in neutron count rate* measured by the *Oulu Cosmic Ray Station.* The measured increase during a solar event can either be caused by a soft proton spectrum with high amplitude, or by a hard proton spectrum with smaller amplitude. In addition, the hardness and the amplitude of the radiation also show a time-dependence. While the true shape of the spectrum is unknown, one can estimate a minimum and a maximum value for its slope during the course of the event. This leads to minimum and maximum values for the dose rates that occur during ground level enhancements. This uncertainty of the solar event spectrum has the consequence that only a very broad value range for the dose rates can be given.

The aim of this work is not only the development of a simulation model, but also to present its results, and to verify its accuracy by means of reference values. This was done using reference values from the literature that offer reliable dose rates for three different solar activities across the whole range of cutoff rigidity. The simulation results show a very good agreement.

In addition, the simulation model was tested by comparing its results with values from TEPC in-flight measurement performed in September 2014. The results are listed in Table 18 and show a reasonable agreement.

Table 18: Comparison of simulation results with measured values from TEPC in-flight measurement

	$\dot{H}^*(10)\ TEPC$ [µSv/h]	$\dot{H}^*(10)\ Simulation$ [µSv/h]	$Deviation\ from\ measurement$
$FL400$	5.4 ± 0.7	5.1	-6.8%
$FL450$	7.4 ± 1.1	5.9	-20.1%

After the verification process, the simulation model was used to estimate the radiation exposure during three historic solar events. The results show extreme dose rates in the polar regions that are by far higher than the dose rates produced by the galactic radiation. However, this only holds for the polar regions. Near the equator, the situation is reversed and the galactic spectrum dominates the dose production, even though the involved dose rates are a lot lower.

The previous analysis of radiation exposure caused by galactic and solar cosmic radiation gives rise to a deeper investigation of the radiation hazard during long-distance flights. Of particular interest are flight routes that pass through high latitudes. For this reason, four flights have been chosen. Three of which pass through, or pass near the polar regions, while one was chosen which completely avoids polar regions so that the dependence on the flight route can be illustrated. The accumulated doses were calculated for the best and the worst case of the solar event GLE42 as well as for the galactic spectrum. The results are listed in Table 19 through Table 22. It is apparent that the flight route significantly influences the accumulated doses produced by the GLE. The radiation hazard during solar events must not be underestimated, as very high doses can occur. By avoiding polar regions, the dose can effectively be reduced, which is demonstrated by flight Paris-Washington in Table 22. Another effective way to keep the doses to a minimum is to reduce the flight level.

Table 19: Accumulated ambient dose equivalent on flight Chicago-Beijing during GLE42

	$H^*(10)$ [µSv]
SCR minimum	144
SCR maximum	1515
GCR	46

Table 20: Accumulated ambient dose equivalent on flight San Francisco-Paris during GLE42

	$H^*(10)$ [µSv]
SCR minimum	169
SCR maximum	1746
GCR	42

Table 21: Accumulated ambient dose equivalent on flight Sydney-Johannesburg during GLE42

	$H^*(10)$ [µSv]
SCR minimum	106
SCR maximum	972
GCR	50

Table 22: Accumulated ambient dose equivalent on flight Paris-Washington during GLE42

	$H^*(10)$ [µSv]
SCR minimum	33
SCR maximum	55
GCR	34

The simulation model developed in this work is very advanced, but there is still room for improvement. This is particularly true for the calculation of the solar cosmic ray spectra. The current model only delivers minimum and maximum values for the dose rates during solar events. The 'true' value is concealed, because the slope of the spectrum can only be estimated. With only one neutron monitor, the determination of the slope is impossible, since there are more unknowns (amplitude and slope) than equations. This problem can be overcome by including data from further neutron monitors in the calculation. In addition, extra neutron monitors could be used to determine the anisotropy of the solar particle event, which is presently neglected.

Also the simulation model itself can be further improved. One example is the enhancement of energy and height resolution. Furthermore, as the model is based on the computer codes *Planetocosmics* and *GEANT4*, any improvements and updates of these codes should be considered.

References

[1] O. C. Allkofer; *Introduction to Cosmic Radiation;* Munich (DE): Karl Thiemig Verlag; 1975

[2] L. I. Dorman; *Cosmic Rays in the Earth's Atmosphere and Underground;* Dordrecht (NL): Kluwer Academic Publishers; 2004

[3] A. Holmes-Siedle and L. Adams; *Handbook of radiation effects;* New York (USA): Oxford Universiy Press; 2002

[4] WDC-SILSO (Sunspot Index and Longterm Solar Observations); Royal Observatory of Belgium, Brussels; http://www.sidc.be/silso/datafiles; [Accessed 25 November 2014]

[5] University of Delaware, Bartol Resarch Institute, Neutron Monitor Program; GLE List: http://neutronm.bartol.udel.edu; [Accessed 25 November 2014]

[6] Cosmic Ray Station of the University of Oulu / Sodankyla Geophysical Observatory; GLE: http://cosmicrays.oulu.fi; [Accessed 26 November 2014]

[7] W. Baumjohann and R. Treumann; *Basic Space Plasma Physics;* London (GB): Imperial College Press; 1996

[8] D. F. Smart & M. A. Shea; *World Grid of Calculated Cosmic Ray Vertical Cutoff Rigidities for Epoch 2000.0;* Proceedings of the 30th International Cosmic Ray Converence, Mexico City (MX), Vol. 1, p. 737-740; 2008

[9] M. Latocha, M. Autischer, P. Beck, J. F. Bottolier-Depois, S. Rollet and F. Trompier; *The results of cosmic radiation in-flight TEPC measurements during the CAATER flight campaign and comparison with simulation;* Ratiation Protection Dosimetry, 125(1-4): 412-415; 2006

[10] Neutron Monitor Database; Public Outreach: http://www.nmdb.eu; [Accessed 18 April 2015]

[11] P. Beck, M. Latocha, S. Rollet, G. Stehno; *TEPC reference measurements at aircraft altitudes during a solar storm;* Advances in Space Research Vol. 36, Nb. 9, p. 1627-1633; ARC Seibersdorf Reasearch GmbH; Seibersdorf, Austria; 2005

[12] Bogdan Povh, Klaus Rith, Christoph Scholz, Frank Zetsche, Werne Rodejohann; *Eine Einführung in die physikalischen Konzepte;* Heidelberg (DE): Springer Spektrum; 2013

[13] H. Krieger; *Grundlagen der Strahlenphysik und des Strahlenschutzes;* Wiesbaden (DE): Vieweg + Teubner; 2011

[14] P. Dunne; *Demonstrating Cosmic ray induced electromagnetic cascades;* Preston College; UK; Teaching Materials: https://teachers.web.cern.ch; [Accessed 8 January 2015]

[15] ICRU Report 51; *Quantities and Units in Radiation Protection Dosimetry;* Bethesda, Maryland, USA: International Commission on Radiation Units and Measurements; 1993

[16] F. H. Attix; *Introduction to radiological physics and radiation dosimetry;* New York (USA): John Wiley & Sons, Inc; 1986

[17] G. F. Knoll; *Radiation detection and measurement;* New York (USA): John Wiley & Sons, Inc; 2010

[18] H. Krieger; *Strahlungsmessung und Dosimetrie;* Wiesbaden (DE): Vieweg + Teubner; 2011

[19] ICRP Publication 103; *The 2007 Recommendations of the International Commission on Radiological Protection;* International Commission on Radiological Protection; ICRP Publication 103. Ann. ICRP 37 (2-4); 2007

[20] H. Rossi & M. Zaider; *Microdosimetry and its Applications;* New York (USA): Springer; 1996

[21] *Operations and repair manual (HAWK-TEPC);* Far West Technology, Inc; 2000

[22] P. Beck, C. Dyer, N. Fuller, A. Hands, M. Latocha, S. Rollet and F. Spurný; *Overview of on-board measurements during solar storm periods;* Radiation Protection Dosimetry, 136(4): 297-303; 2009

[23] M. Autischer; *Simulation von Kosmischer Strahlung und Vergleich mit experimentellen Ergebnissen (Dissertation);* Graz University of Technology; Graz (AT); 2010

[24] ICRU Report 36; *Microdosimetry;* Bethesda, Maryland, USA: International Commission on Radiation Units and Measurements; 1983

[25] C. Theis, W. Kernbichler; *Grundlagen der Monte Carlo Methoden;* Graz University of Technology; Graz (AT); 2002

[26] W. L. Dunn, J. K. Shultis; *Monte Carlo methods for design and analysis of radiation detectors;* Radiation Physics and Chemistry 78: 852-858; 2009

[27] S. Raychaudhuri; *Introduction to Monte Carlo simulation;* Proceedings of the 2008 Winter Simulation Conference, Austin (Texas USA), p. 91-100; Oracle Crystal Ball Global Business Unit; Broomfield; USA; 2008

[28] Epixanalytics; *Introduction to Monte Carlo simulation;* Model Assist: http://www.epixanalytics.com; [Accessed 23 January 2015]

[29] ESA; *GEANT4 Space Users Homepage;* http://geant4.esa.int/; [Accessed 31 January 2015]

[30] CERN; *GEANT4;* http://geant4.cern.ch/; [Accessed 31 January 2015]

[31] T. Ersmark; *Geant4 Monte Carlo Simulations of the International Space Station Radiation Environment (Doctoral Thesis);* Stockholm (SE): KTH Engineering Sciences, 2006

[32] M. Asai; *Geant4 Tutorial Course (Kernel1);* SLAC National Acceleration Laboratory

[33] CERN; *Reference Physics Lists;* http://geant4.cern.ch/support; [Accessed 4 February 2015]

[34] CERN; *Model: Bertini Cascade;* http://geant4.cern.ch/support; [Accessed 4 February 2015]

[35] CERN; *Model: G4NeutronHPInelastic;* [Accessed 4 February 2015]

[36] CERN; *Physics Lists EM Constructors in Geant4 9.5;* [Accessed 5 February 2015]

[37] Geant4 Physics Reference Manual (Version: geant4 10.0); 2013

[38] L. Desorgher; *PLANETOCOSMICS Software User Manual;* Physikalisches Institut University Bern; 2005

[39] M. Pelliccioni; *Overview of fluence-to-effective dose and fluence-to-ambient dose equivalent conversion coefficients for high energy radiation calculated using the FLUKA code;* Radiation Protection Dosimetry, Vol. 88, No. 4, p. 279-297; 2000

[40] L. Desorgher; *PLANETOCOSMICS GEANT4;* Physikalisches Institut Universität Bern; 2006 http://cosray.unibe.ch/~laurent/planetocosmics/; [Accessed 7 February 2015]

[41] K. Herbst, A. Kopp, B. Heber, F. Steinhilber, H. Fichtner, K. Scherer and D. Matthiä; *On the importance of the local interstellar spectrum for the solar modulation parameter;* Journal of the Geophysical Reasearch, Vol. 115; 2010

[42] E. Flückiger, M. Moser, B. Pirard, R. Bütikofer, L. Desorgher; *A parameterized neutron monitor yield function for space weather applications;* Proceedings of the 30th International Cosmic Ray Conference, Mérida (Mexico), Vol. 1, p. 289-292; 2006

[43] I. Usoskin, K. Mursula, J. Kangas and B. Gvozdevsky; *On-Line Database of Cosmic Ray Intensities;* Proceedings of ICRC 2001: 1-4; 2001

[44] Flückiger et. al; *Yield function by Flückiger et al;* 2008

[45] ICRU; *Reference Data for the Validation of Doses from Cosmic-Radiation Exposure of Aircraft Crew;* ICRU Report 84 (prepared jointly with ICRP); Journal of the ICRU Vol. 10, No. 2; 2010

[46] U. Ellwanger; *Vom Universum zu den Elementarteilchen;* Heidelberg (DE): Springer; 2008

[47] C. Berger; *Elementarteilchenphysik;* Heidelberg (DE): Springer; 2006

[48] I. Usoskin; Cosmic Ray Station, University of Oulu / Sodankyla Geophysical Observatory; CR Modulation: http://cosmicrays.oulu.fi; [Accessed 17 February 2015]

[49] D. Smart and M. Shea; *World grid of calculated cosmic ray vertical cutoff rigidities for epoch 1990.0;*Proceedings of the 25th International Cosmic Ray Conference, Durban (South Africa), Vol. 2, p. 401; 1997

[50] JGCM 100:2008; *Evaluation of measurement data – Guide to the expression of uncertainty in measurement;* Sévres (FR): Joint Committee for Guides in Metrology; 2008

[51] D. Smart M. Shea; *A review of geomagnetic cutoff rigidities for earth-orbiting spacecraft;* Advances in Space Research 36: 2012-2020; 2005

List of tables

List of figures

Abbreveations

GCR.....Galactic cosmic radiation

GLE.....Ground level enhancement

ICRP.....International Commission on Radiological Protection

ICRU .....International Comission on Radiation Units & Measurements

LET .....Linear energy transfer

MC .....Monte Carlo

NM .....Neutron Monitor

SCR .....Solar cosmic radiation

SDP .....Solar deceleration potential

SPE.....Solar particle event

TEPC.....Tissue equivalent proportional counter

Appendix

A. Particle families

The classification of particles according to the their spin leads to two families, the *Fermions* and the *Bosons*. All particles that have half-integer spin belong to the fermions, for instance the electron, the proton or the neutron. They all obey the *Pauli Exclusion Principle*, which says, that every atomic state that is given by a unique set of quantum numbers can only be occupied by one single fermion. This has very strong consequences on the electronic configuration of atoms and the structure of the periodic table of elements. [13] Another interesting property is that in a physical process, the amount of fermions is either conserved, or they are created or destroyed as a pair of particle and antiparticle. [41]

The second family are the Bosons, which contain all particles with integer spin. In comparison with fermions, they neither obey the Pauli Exclusion Principle nor are the amounts of bosons before and after a physical process conserved. They can be created or annihilated without the presence of an antiparticle. In general one can say that matter is built up from fermions, while bosons act as exchange particles for the fundamental forces. [41]

All particles that are made of quarks obey the strong interaction and are called *Hadrons*. They can be further divided into *Baryons* and *Mesons* depending on whether they have half-integer or integer spin respectively. Therefore, baryons belong to the family of fermions and mesons to the family of bosons. [12] Now there remain only two species of particles. The first are the *Leptons*, which are fermions that obey the weak interaction, if charged the electromagnetic interaction but not the strong interaction. [12] The second are the *Photons*, which are bosons and only underlie the electro-magnetic force. [42] The categorization of the particle families is outlined in Table 23.

Table 23: Particle families

	Fermionen *half-integer spin*	**Bosonen** *integer spin*
Hadrons: obey strong interaction	**Baryons**	**Mesons**
	→ proton	→ pions
	→ neutron	→ kaons
Independent of strong interaction	**Leptons**	**Photons**
	→ electron	
	→ electron-neutrino	
	→ myon	
	→ myon-neutrino	
	→ tauon	
	→ tauon-neutrino	

Hadrons: Baryons and Mesons

Scattering experiments have shown that nucleons are not point-like objects but instead they have an inner structure and a charge distribution. [13] Based on this discovery, a new model was developed that should be able to explain the properties of the nucleons. This model is the

quark model and it uses new elementary particles, the quarks that lead as compounds to the observed properties such as charge and spin. [12] Nowadays the quark model consists of three generations, altogether resulting in six quarks:

Table 24: Quarks and their properties [13] [41]

	Name	Symbol	Charge [e_0]	Mass [GeV / c^2]	Spin	Strong interaction	Weak interaction
Generation I	*Up* *Down*	*u* *d*	⅔ - ⅓	~ *0.3* ~ *0.3*	½ ½	✓ ✓	✓ ✓
Generation II	*Charm* *Strange*	*c* *s*	⅔ - ⅓	~ *1.4* ~ *0.5*	½ ½	✓ ✓	✓ ✓
Generation III	*Top* *Bottom*	*t* *b*	⅔ - ⅓	~ *171* ~ *4.4*	½ ½	✓ ✓	✓ ✓

Bound states of three quarks are called Baryons whose most famous members are the nucleons. Since every quark carries spin ½ the resulting total spin is half-integral, therefor they are fermions. The total charge of the baryon is obtained by summing up the charges of the single components. The proton for instance contains two up-quarks with a charge of ⅔ e_0 and one down-quark with a negative charge of ⅓ e_0, leading to a total charge of 1 e_0. The electrically neutral neutron however contains only one up-quark but two down-quarks so that the charges cancel out, making it electrically neutral to the outside. [12] [13]

$$|p\rangle = |uud\rangle$$

$$|n\rangle = |udd\rangle \qquad [42]$$

Aside from the nucleons, there exist a lot more baryons, for instance the Delta-particles that also consist of up- and down-quarks or hyperons that possess strange-quarks. [12] However, a full description of all these particles would exceed the scope of this work.

The second group are the Mesons. They are made up of two quarks, more precisely a quark-antiquark pair. The spin-coupling of the two quarks leads to an integer spin, that is why they belong to the family of bosons. The most important mesons are the *Pions.* They are the lightest hadrons and exist in three states of charge, π^-, π^0 and π^+. Their composition is as follows: [12]

$$|\pi^-\rangle = |\bar{u}d\rangle$$

$$|\pi^0\rangle = \frac{1}{\sqrt{2}}\{|u\bar{u}\rangle - |d\bar{d}\rangle\}$$

$$|\pi^+\rangle = |u\bar{d}\rangle$$

The π^0 Meson is a mixed state where $\frac{1}{\sqrt{2}}$ is the normalisation. Another important group of mesons that has to be mentioned are the *Kaons.* They also consist of a quark-antiquark pair, but one of the quarks is a strange-quark: [12]

$$|K^+\rangle = |u\bar{s}\rangle \qquad |K^-\rangle = |\bar{u}s\rangle$$

$$|K^0\rangle = |d\bar{s}\rangle \qquad |\bar{K}^0\rangle = |\bar{d}s\rangle$$

Leptons

Leptons are fundamental particles that belong to the family of fermions. According to the present knowledge, there exist six leptons. Three of them are negatively charged and are called the *Electron (e)*, the *Muon (μ)* and the *Tauon (τ).* The electron, being the lightest of them, is the only one that is stable. Since there are no lighter charged particles than the electron, any decay would violate the rule of charge conservation. Therefore, it has an infinite lifetime. The muon and the tauon are considerably heavier and decay into lighter particles within a fraction of a second. For every charged lepton, there exists an electrically neutral partner, the *Neutrino (v_e, v_μ and v_τ).* Their masses are extremely small. Initially they were believed to have zero mass, but it was observed that given certain conditions, they can transform from one lepton generation (e.g. ν_e) into another (e.g. ν_μ), which is only possible if they have a mass. Their detection is extremely difficult, because they are the only particles that only obey the weak interaction. As a result, they can penetrate easily through matter since they are neither diffracted by electrons due to the electromagnetic interaction, nor by the nuclei due to the strong interaction. [41] [42] [12]

Table 25: Leptons and their properties [13] [42]

	Name	Symb.	Charge [e_0]	Mass [MeV]	Lifetime [s]	St.	W.
Gen. I	*Electron*	e^-	*-1*	*0.511*	∞	✖	✓
	Electron Neutrino	ν_e	*0*	$< 2 \cdot 10^{-6}$	∞	✖	✓
Gen. II	*Muon*	μ	*-1*	*106*	$2.2 \cdot 10^{-6}$	✖	✓
	Muon Neutrino	ν_μ	*0*	< 0.19	∞	✖	✓
Gen. III	*Tauon*	τ	*-1*	*1777*	$2.9 \cdot 10^{-13}$	✖	✓
	Tauon Neutrino	ν_τ	*0*	< 18.2		✖	✓

Photons

Photons are the basic building blocks of electromagnetic radiation. They have zero mass and belong to the bosons because their spin is equal to one. [41]

B. Modulation parameter Φ

Values for the modulation parameter in MV reconstructed from ground based cosmic ray data. Values downloaded from [43].

Table 26: Modulation parameter in MV (Data from [43])

Year	Jan.	Feb.	Mar.	Apr.	May.	Jun.	Jul.	Aug.	Sep.	Oct.	Nov.	Dec.	*Annual*
1936	-	-	-	-	-	-	252	242	260	271	290	363	*279*
1937	401	451	516	550	546	662	557	588	546	553	492	496	*528*
1938	716	696	560	650	502	401	348	371	389	401	401	416	*481*
1939	416	509	506	599	632	509	422	345	389	389	295	303	*438*
1940	287	300	292	290	255	273	268	281	287	295	320	345	*291*
1941	389	342	371	354	323	287	303	271	309	268	273	311	*316*
1942	273	273	447	340	287	268	279	239	237	245	242	237	*279*
1943	250	255	258	271	268	271	306	309	314	292	279	273	*279*
1944	279	263	258	239	211	187	184	192	177	184	170	211	*212*
1945	250	250	334	340	258	258	255	245	234	229	242	245	*261*
1946	303	768	610	581	647	595	602	550	578	486	457	407	*543*
1947	432	413	560	685	658	1166	925	1031	1128	1001	911	827	*788*
1948	716	677	708	602	748	581	581	595	712	669	602	588	*647*
1949	696	677	613	632	585	539	486	522	479	599	526	486	*568*
1950	606	628	512	512	526	473	496	463	512	512	435	416	*506*
1951	492	647	631	618	555	510	553	587	523	514	535	513	*562*
1952	551	567	587	546	489	464	447	448	436	490	465	483	*497*
1953	515	497	506	500	500	482	495	488	483	469	472	453	*488*
1954	445	427	401	411	404	407	399	376	384	386	399	411	*404*
1955	462	413	409	409	399	406	405	417	400	429	425	476	*420*
1956	511	551	623	567	604	592	555	562	598	521	647	822	*593*
1957	955	967	929	1053	984	1033	1087	1021	1226	1149	1180	1284	*1068*
1958	1266	1226	1330	1308	1167	1090	1216	1120	1093	1089	1063	1125	*1172*
1959	1080	1139	1029	965	1072	996	1327	1269	1187	1044	1022	1056	*1095*
1960	1136	1080	1007	1112	1109	1042	1042	953	956	953	1024	945	*1028*
1961	848	815	813	822	776	783	956	836	787	749	676	698	*795*
1962	700	723	708	737	689	678	667	667	699	705	668	678	*693*
1963	612	587	592	567	603	566	562	575	613	578	561	538	*579*
1964	515	519	495	479	468	469	459	456	430	433	436	406	*451*
1965	389	394	371	348	338	386	406	413	406	394	371	376	*382*
1966	412	420	441	452	431	479	507	515	665	575	541	584	*499*
1967	632	656	597	579	630	655	625	671	658	645	690	689	*643*
1968	674	707	713	669	694	765	761	742	789	850	985	934	*770*
1969	811	799	820	823	962	1014	948	861	819	798	796	791	*852*
1970	810	769	784	834	835	937	934	855	780	758	834	706	*818*
1971	717	641	646	624	591	515	514	493	497	465	475	488	*553*
1972	507	520	453	427	457	528	461	636	475	461	505	476	*491*
1973	463	473	498	565	616	524	491	466	427	428	416	418	*481*
1974	420	402	438	461	527	567	630	563	605	590	565	499	*520*

Year	Jan.	Feb.	Mar.	Apr.	May.	Jun.	Jul.	Aug.	Sep.	Oct.	Nov.	Dec.	*Annual*
1975	494	459	450	429	420	407	417	442	436	437	471	448	*442*
1976	446	440	436	461	434	426	412	408	407	408	404	411	*424*
1977	421	417	419	416	417	442	487	476	475	438	408	418	*436*
1978	478	496	510	588	669	602	591	495	495	566	528	530	*544*
1979	584	609	653	738	706	812	799	906	860	778	774	688	*739*
1980	716	743	686	762	757	886	885	855	866	960	1052	1038	*845*
1981	878	968	995	1055	1124	967	930	923	871	1046	1010	886	*969*
1982	813	982	828	798	758	1009	1258	1240	1422	1222	1150	1256	*1046*
1983	1086	969	877	874	1029	928	826	836	803	787	762	761	*874*
1984	709	736	800	846	967	880	842	778	753	751	772	746	*797*
1985	724	656	636	609	596	542	549	543	501	495	464	485	*564*
1986	486	575	507	434	416	405	403	402	401	378	433	382	*434*
1987	339	311	312	328	349	406	435	468	501	492	534	534	*414*
1988	626	593	581	602	590	610	681	697	682	714	728	819	*658*
1989	893	898	1183	1132	1234	1187	1022	1114	1195	1356	1470	1362	*1161*
1990	1232	1196	1275	1424	1452	1435	1247	1294	1187	1073	996	985	*1226*
1991	872	862	1257	1197	1158	2016	1938	1471	1190	1126	1115	1028	*1234*
1992	1019	1066	948	815	860	748	682	695	724	658	679	616	*785*
1993	632	634	685	621	599	580	573	571	548	545	534	541	*588*
1994	536	598	603	605	576	573	544	518	497	507	499	505	*546*
1995	484	470	494	476	468	472	473	464	459	457	451	437	*467*
1996	436	414	412	411	419	424	425	429	431	449	451	437	*428*
1997	418	400	404	413	404	405	409	394	404	424	439	424	*412*
1998	427	423	413	513	572	555	514	568	515	478	502	540	*500*
1999	602	602	589	573	589	539	513	609	691	733	751	787	*629*
2000	752	794	865	848	967	1073	1167	1057	992	882	1023	960	*944*
2001	881	774	725	995	874	832	808	904	897	959	865	833	*860*
2002	977	826	888	895	900	863	948	1058	963	926	1023	986	*936*
2003	895	892	876	909	945	1067	959	908	869	963	1281	930	*954*
2004	936	784	705	676	630	636	693	662	632	545	645	615	*677*
2005	788	642	620	589	681	610	643	676	798	596	542	540	*641*
2006	516	462	435	430	423	423	443	436	440	407	408	467	*440*
2007	391	396	376	355	351	354	357	361	352	348	353	340	*361*
2008	360	367	362	361	370	367	356	342	336	322	302	309	*334*
2009	302	285	276	267	267	270	269	274	270	260	258	255	*271*
2010	271	316	347	376	361	371	377	388	388	374	389	412	*364*
2011	398	414	426	496	453	551	518	509	513	534	488	438	*478*
2012	490	533	634	506	494	546	664	643	583	587	571	544	*565*
2013	533	530	564	559	674	679	665	640	614	571	590	625	*603*
2014	606	681	652	633	660	656	628	590	634	632	645	731	*645*

C. Grid for vertical cutoff rigidity values

Table 27: World grid of vertical cutoff rigidity values in GV (data from [44])

↔ Longitude

Latitude ↕	-180	-170	-160	-150	-140	-130	-120	-110	-100	-90	-80	-70	-60	-50	-40	-30	-20	-10	0	10	20	30	40	50	60	70	80	90	100	110	120	130	140	150	160	170	180
90	0.0	0.0	0.0	0.0	0.0	0.0	0.0	0.0	0.0	0.0	0.0	0.0	0.0	0.0	0.0	0.0	0.0	0.0	0.0	0.0	0.0	0.0	0.0	0.0	0.0	0.0	0.0	0.0	0.0	0.0	0.0	0.0	0.0	0.0	0.0	0.0	0.0
85	0.0	0.0	0.0	0.0	0.0	0.0	0.0	0.0	0.0	0.0	0.0	0.0	0.0	0.0	0.0	0.0	0.0	0.0	0.0	0.0	0.0	0.0	0.0	0.0	0.0	0.0	0.0	0.0	0.0	0.0	0.0	0.0	0.0	0.0	0.0	0.0	0.0
80	0.1	0.0	0.0	0.0	0.0	0.0	0.0	0.0	0.0	0.0	0.0	0.0	0.0	0.0	0.0	0.0	0.0	0.0	0.0	0.0	0.0	0.1	0.1	0.1	0.1	0.1	0.1	0.1	0.1	0.1	0.1	0.1	0.1	0.1	0.1	0.1	0.1
75	0.2	0.2	0.1	0.1	0.1	0.0	0.0	0.0	0.0	0.0	0.0	0.0	0.0	0.0	0.0	0.0	0.1	0.1	0.1	0.1	0.1	0.2	0.2	0.2	0.2	0.2	0.3	0.2	0.3	0.3	0.3	0.3	0.2	0.3	0.2	0.2	0.2
70	0.5	0.4	0.3	0.2	0.2	0.1	0.1	0.0	0.0	0.0	0.0	0.0	0.0	0.0	0.1	0.1	0.2	0.2	0.3	0.3	0.4	0.4	0.4	0.4	0.4	0.5	0.5	0.5	0.5	0.5	0.6	0.6	0.6	0.6	0.6	0.5	0.5
65	0.9	0.8	0.7	0.5	0.4	0.3	0.2	0.1	0.1	0.1	0.1	0.1	0.1	0.2	0.2	0.3	0.4	0.5	0.6	0.7	0.7	0.8	0.8	0.9	0.9	0.9	0.9	0.9	1.0	1.0	1.1	1.1	1.2	1.2	1.1	1.1	0.9
60	1.7	1.5	1.2	1.0	0.8	0.6	0.4	0.3	0.2	0.2	0.2	0.2	0.3	0.4	0.5	0.7	0.8	1.0	1.2	1.3	1.4	1.4	1.5	1.6	1.5	1.6	1.7	1.6	1.7	1.8	1.9	2.0	2.1	2.0	2.0	1.9	1.7
55	2.8	2.4	2.1	1.7	1.4	1.1	0.8	0.6	0.5	0.4	0.4	0.4	0.5	0.8	1.0	1.3	1.6	1.9	2.1	2.2	2.3	2.4	2.4	2.5	2.6	2.6	2.6	2.8	2.8	2.9	3.1	3.2	3.2	3.2	3.1	3.0	2.8
50	4.2	3.7	3.2	2.7	2.3	1.8	1.4	1.1	0.9	0.8	0.8	0.8	1.0	1.4	1.8	2.3	2.6	3.0	3.3	3.5	3.6	3.7	3.8	3.9	3.9	4.1	4.1	4.2	4.3	4.4	4.6	4.8	4.9	4.9	4.7	4.6	4.2
45	5.5	5.1	4.6	4.2	3.6	2.9	2.4	1.9	1.6	1.4	1.3	1.4	1.8	2.3	2.9	3.6	4.2	4.7	5.0	5.1	5.2	5.2	5.3	5.4	5.5	5.6	5.8	5.9	6.0	6.2	6.5	6.7	6.8	6.8	6.5	6.0	5.5
40	7.8	6.9	6.0	5.4	4.9	4.3	3.6	3.0	2.5	2.2	2.1	2.2	2.7	3.6	4.5	5.3	6.0	6.6	7.1	7.3	7.4	7.4	7.5	7.6	7.8	8.1	8.5	8.8	8.9	9.2	9.5	9.8	9.9	9.7	9.2	8.6	7.8
35	9.5	9.2	8.6	7.7	6.6	5.7	5.1	4.5	3.8	3.2	3.0	3.4	4.0	4.9	6.3	7.9	8.9	9.5	9.7	9.8	9.9	10.0	10.1	10.4	10.9	11.3	11.4	11.3	11.4	11.6	11.9	12.1	12.0	11.6	10.9	10.2	9.5
30	11.6	10.8	10.1	9.7	9.1	8.1	6.8	5.8	5.0	4.4	4.1	4.4	5.4	7.3	9.2	10.3	10.9	11.3	11.6	11.7	11.8	12.0	12.2	12.5	12.9	13.4	13.8	14.1	14.2	14.2	14.2	14.0	13.8	13.4	13.0	12.4	11.6
25	13.0	12.5	12.1	11.6	11.1	10.4	9.5	8.2	6.9	5.9	5.5	6.1	7.7	9.7	11.2	12.0	12.6	13.0	13.3	13.5	13.8	14.0	14.2	14.4	14.8	15.1	15.4	15.6	15.7	15.6	15.4	15.2	14.8	14.4	13.9	13.4	13.0
20	13.8	13.4	13.1	12.7	12.3	11.8	11.1	9.7	8.4	7.5	6.9	7.4	9.2	11.2	12.5	13.0	13.5	13.9	14.2	14.5	14.7	14.9	15.2	15.5	15.8	16.2	16.5	16.7	16.7	16.6	16.3	16.0	15.6	15.2	14.7	14.2	13.8
15	14.5	14.1	13.8	13.5	13.2	12.8	12.2	11.2	10.1	9.1	8.7	9.8	11.5	12.5	13.0	13.6	14.0	14.3	14.6	14.9	15.2	15.5	15.8	16.1	16.5	16.8	17.1	17.3	17.3	17.2	16.9	16.6	16.1	15.7	15.3	14.9	14.5
10	15.0	14.7	14.4	14.2	13.9	13.6	13.1	12.5	11.7	11.1	11.1	11.6	12.3	12.9	13.4	13.8	14.1	14.4	14.7	15.0	15.3	15.6	15.9	16.3	16.7	17.1	17.4	17.6	17.6	17.4	17.2	16.8	16.4	16.0	15.7	15.3	15.0
5	15.3	15.1	14.8	14.6	14.3	14.1	13.7	13.3	12.8	12.3	12.2	12.4	12.7	13.1	13.5	13.7	13.9	14.1	14.3	14.5	14.8	15.1	15.5	16.0	16.6	17.0	17.3	17.4	17.5	17.3	17.1	16.8	16.4	16.1	15.8	15.6	15.3
0	15.4	15.2	15.0	14.8	14.6	14.3	14.0	13.7	13.3	13.0	12.7	12.7	12.9	13.1	13.3	13.3	13.4	13.5	13.7	13.9	14.2	14.5	15.0	15.4	16.0	16.4	16.8	16.9	17.0	16.9	16.7	16.4	16.2	15.9	15.8	15.6	15.4
-5	15.3	15.1	15.0	14.8	14.6	14.3	14.1	13.8	13.5	13.2	12.9	12.8	12.9	12.9	12.9	12.8	12.7	12.7	12.8	13.0	13.3	13.7	14.2	14.7	15.1	15.6	15.9	16.1	16.1	16.1	16.0	15.8	15.6	15.5	15.4	15.3	15.3
-10	14.8	14.7	14.6	14.5	14.4	14.2	14.0	13.8	13.5	13.2	12.9	12.7	12.6	12.5	12.4	12.1	11.8	11.6	11.7	11.8	12.1	12.5	13.0	13.5	14.0	14.3	14.6	14.8	14.9	14.9	14.9	14.7	14.6	14.6	14.7	14.7	14.8
-15	13.9	14.0	14.0	14.0	13.9	13.8	13.7	13.5	13.3	13.0	12.7	12.5	12.3	12.0	11.7	11.2	10.7	10.3	10.2	10.4	10.7	11.1	11.6	12.0	12.4	12.8	13.0	13.2	13.3	13.3	13.2	13.2	13.2	13.4	13.5	13.7	13.9
-20	12.6	12.9	13.1	13.2	13.3	13.3	13.2	13.1	12.9	12.6	12.3	12.0	11.7	11.3	10.8	10.1	9.4	8.9	8.7	8.7	8.9	9.3	9.7	10.0	10.4	10.6	10.7	10.7	10.7	10.8	10.8	10.7	10.6	10.7	11.4	12.2	12.6
-25	10.0	10.7	11.0	11.4	12.3	12.5	12.6	12.5	12.4	12.2	11.9	11.5	11.0	10.5	9.7	8.9	8.0	7.4	7.1	7.2	7.4	7.6	7.9	8.1	8.2	8.0	7.7	7.4	7.3	7.4	7.4	7.5	7.8	8.4	9.1	9.7	10.0
-30	8.0	9.1	9.3	9.2	10.1	11.2	11.7	11.8	11.7	11.6	11.3	10.8	10.2	9.5	8.6	7.6	6.9	6.4	5.9	5.7	5.8	5.9	5.9	5.9	5.8	5.6	5.4	5.3	5.2	5.2	5.2	5.2	5.5	5.9	6.3	6.9	8.0
-35	5.6	6.1	7.0	7.9	8.2	8.7	9.8	10.7	11.0	10.9	10.5	10.0	9.3	8.5	7.4	6.5	5.8	5.3	4.8	4.5	4.4	4.3	4.4	4.3	4.2	4.1	3.8	3.5	3.4	3.4	3.3	3.4	3.7	4.1	4.7	5.1	5.6
-40	4.1	4.5	4.9	5.5	6.2	7.2	8.2	9.3	9.9	9.8	9.5	9.1	8.4	7.4	6.5	5.9	5.1	4.4	3.9	3.6	3.5	3.4	3.4	3.2	2.9	2.7	2.5	2.2	2.0	2.0	2.0	2.1	2.3	2.6	3.0	3.5	4.1
-45	2.7	3.1	3.7	4.3	4.7	5.2	6.0	7.2	8.3	8.7	8.5	8.0	7.5	6.9	5.9	4.9	4.1	3.6	3.2	2.9	2.7	2.5	2.4	2.2	2.0	1.7	1.5	1.3	1.2	1.1	1.1	1.2	1.3	1.5	1.9	2.3	2.7
-50	1.6	2.0	2.5	3.0	3.5	4.1	4.6	5.1	6.0	6.8	7.2	6.9	6.3	5.4	4.6	4.0	3.4	3.0	2.6	2.3	2.1	1.9	1.7	1.5	1.3	1.1	0.9	0.7	0.6	0.5	0.6	0.6	0.7	0.8	1.0	1.3	1.6
-55	1.0	1.2	1.5	2.0	2.4	2.9	3.4	3.9	4.4	4.8	5.0	4.9	4.6	4.2	3.7	3.2	2.8	2.4	2.0	1.8	1.6	1.4	1.2	1.0	0.8	0.6	0.5	0.3	0.3	0.2	0.2	0.2	0.3	0.4	0.5	0.7	1.0
-60	0.5	0.7	0.9	1.2	1.5	1.9	2.3	2.7	3.2	3.7	3.8	3.7	3.6	3.4	3.0	2.5	2.1	1.9	1.6	1.4	1.2	1.0	0.9	0.7	0.5	0.4	0.2	0.2	0.1	0.1	0.1	0.1	0.1	0.2	0.2	0.3	0.5
-65	0.2	0.3	0.5	0.7	0.9	1.2	1.5	1.8	2.1	2.4	2.5	2.6	2.5	2.4	2.1	1.9	1.7	1.4	1.2	1.0	0.8	0.7	0.6	0.4	0.3	0.2	0.1	0.1	0.0	0.0	0.0	0.0	0.0	0.0	0.1	0.2	0.2
-70	0.1	0.2	0.3	0.4	0.5	0.7	0.9	1.1	1.4	1.5	1.6	1.7	1.7	1.6	1.4	1.3	1.1	1.0	0.8	0.7	0.6	0.5	0.3	0.2	0.2	0.1	0.1	0.0	0.0	0.0	0.0	0.0	0.0	0.0	0.0	0.0	0.1
-75	0.0	0.1	0.1	0.2	0.3	0.4	0.5	0.6	0.7	0.8	0.9	1.0	1.0	0.9	0.9	0.8	0.7	0.6	0.5	0.4	0.4	0.3	0.2	0.2	0.1	0.1	0.0	0.0	0.0	0.0	0.0	0.0	0.0	0.0	0.0	0.0	0.0
-80	0.0	0.1	0.1	0.1	0.2	0.2	0.3	0.3	0.4	0.4	0.5	0.5	0.5	0.5	0.5	0.5	0.4	0.4	0.3	0.3	0.2	0.2	0.1	0.1	0.1	0.0	0.0	0.0	0.0	0.0	0.0	0.0	0.0	0.0	0.0	0.0	0.0
-85	0.0	0.1	0.1	0.1	0.1	0.1	0.2	0.2	0.2	0.2	0.2	0.2	0.2	0.2	0.2	0.2	0.2	0.2	0.2	0.2	0.1	0.1	0.1	0.1	0.1	0.1	0.0	0.0	0.0	0.0	0.0	0.0	0.0	0.0	0.0	0.0	0.0
-90	0.0	0.1	0.1	0.1	0.1	0.1	0.1	0.1	0.1	0.1	0.1	0.1	0.1	0.1	0.1	0.1	0.1	0.1	0.1	0.1	0.1	0.1	0.1	0.1	0.1	0.1	0.0	0.0	0.0	0.0	0.0	0.0	0.0	0.0	0.0	0.0	0.0

D. ICRU reference values for ambient dose equivalent rate

Table 28: ICRU reference values for January 1998 (Data from [40])

R_C [GV]	$\dot{H}^*(10)$ [µSv/h]		
	FL310 ~ 9.45 km	FL350 ~ 10.67 km	FL390 ~ 11.89 km
0	4.3	5.9	7.6
1	4.2	5.8	7.4
2	4.0	5.5	7.0
3	3.8	5.2	6.6
4	3.5	4.8	6.0
5	3.2	4.4	5.5
6	2.9	4.0	5.0
7	2.7	3.6	4.5
8	2.5	3.3	4.1
9	2.2	3.0	3.7
10	2.1	2.7	3.3
11	1.9	2.5	3.0
12	1.8	2.3	2.8
13	1.7	2.1	2.6
14	1.6	2.0	2.5
15	1.5	1.9	2.3
16	1.5	1.9	2.2
17	1.5	1.9	2.2

Table 29: Comparison to ICRU reference values for January 1998
Left: Simulation results with modulation potential $\phi = 393$ MV
Right: Deviation percentage to ICRU reference values in Table 28

R_C [GV]	$\dot{H}^*(10)$ [µSv/h]			Deviation from ICRU reference values		
	FL310 ~ 9.45 km	FL350 ~ 10.67 km	FL390 ~ 11.89 km	FL310 ~ 9.45 km	FL350 ~ 10.67 km	FL390 ~ 11.89 km
0	5.3	7.3	9.3	+24%	+23%	+22%
1	5.3	7.2	9.2	+27%	+25%	+25%
2	4.9	6.6	8.3	+23%	+20%	+19%
3	4.2	5.6	6.9	+11%	+8%	+5%
4	3.6	4.8	5.8	+4%	-1%	-3%
5	3.2	4.1	5.0	-1%	-7%	-10%
6	2.8	3.6	4.3	-5%	-11%	-14%
7	2.5	3.2	3.8	-8%	-11%	-15%
8	2.2	2.8	3.4	-11%	-14%	-18%
9	2.1	2.6	3.1	-7%	-13%	-17%
10	1.9	2.4	2.8	-10%	-12%	-15%
11	1.7	2.2	2.5	-9%	-13%	-15%
12	1.6	2.0	2.4	-9%	-11%	-15%
13	1.5	1.9	2.2	-10%	-8%	-14%
14	1.4	1.8	2.1	-10%	-10%	-16%
15	1.4	1.7	2.0	-10%	-11%	-15%
16	1.3	1.6	1.9	-13%	-15%	-15%
17	1.2	1.5	1.8	-17%	-19%	-19%

Table 30: ICRU reference values for January 2000 (Data from [40])

R_C [GV]	$\dot{H}^*(10)$ [µSv/h]		
	FL310 ~ 9.45 km	FL350 ~ 10.67 km	FL390 ~ 11.89 km
0	4.0	5.2	6.4
1	3.9	5.1	6.3
2	3.7	4.8	6.0
3	3.5	4.6	5.6
4	3.3	4.2	5.2
5	3.0	3.9	4.8
6	2.8	3.6	4.4
7	2.5	3.3	4.0
8	2.3	3.0	3.6
9	2.2	2.7	3.3
10	2.0	2.5	3.0
11	1.9	2.3	2.8
12	1.7	2.2	2.6
13	1.7	2.1	2.5
14	1.6	2.0	2.4
15	1.5	1.9	2.3
16	1.5	1.8	2.2
17	1.5	1.8	2.1

Table 31: Comparison to ICRU reference values for January 2000
Left: Simulation results with modulation potential $\phi = 729$ MV
Right: Deviation percentage to ICRU reference values in Table 30

R_C [GV]	$\dot{H}^*(10)$ [µSv/h]			Deviation from ICRU reference values		
	FL310 ~ 9.45 km	FL350 ~ 10.67 km	FL390 ~ 11.89 km	FL310 ~ 9.45 km	FL350 ~ 10.67 km	FL390 ~ 11.89 km
0	4.1	5.6	7.0	+4%	+7%	+9%
1	4.1	5.6	7.0	+6%	+9%	+11%
2	3.9	5.2	6.5	+7%	+9%	+9%
3	3.5	4.6	5.7	+1%	+1%	+2%
4	3.1	4.1	5.0	-5%	-3%	-5%
5	2.8	3.6	4.3	-7%	-8%	-9%
6	2.5	3.2	3.8	-11%	-11%	-13%
7	2.3	2.9	3.5	-9%	-12%	-14%
8	2.1	2.6	3.1	-11%	-13%	-14%
9	1.9	2.4	2.8	-13%	-11%	-14%
10	1.8	2.2	2.6	-12%	-11%	-13%
11	1.6	2.0	2.4	-14%	-11%	-15%
12	1.5	1.9	2.3	-9%	-12%	-13%
13	1.5	1.8	2.1	-14%	-13%	-15%
14	1.4	1.7	2.0	-14%	-14%	-17%
15	1.3	1.6	1.9	-13%	-15%	-19%
16	1.2	1.5	1.8	-17%	-14%	-19%
17	1.2	1.5	1.7	-20%	-17%	-18%

Table 32: ICRU reference values for January 2002 (Data from [40])

R_C [GV]	$\dot{H}^*(10)$ [µSv/h]		
	FL310 ~ 9.45 km	FL350 ~ 10.67 km	FL390 ~ 11.89 km
0	3.7	4.7	5.7
1	3.6	4.6	5.6
2	3.4	4.4	5.3
3	3.3	4.1	5.0
4	3.0	3.9	4.7
5	2.8	3.6	4.3
6	2.6	3.3	4.0
7	2.4	3.0	3.7
8	2.2	2.8	3.4
9	2.1	2.6	3.1
10	1.9	2.4	2.9
11	1.8	2.2	2.7
12	1.7	2.1	2.5
13	1.6	2.0	2.4
14	1.6	1.9	2.3
15	1.5	1.9	2.2
16	1.5	1.8	2.2
17	1.4	1.8	2.1

Table 33: Comparison to ICRU reference values for January 2002
Left: Simulation results with modulation potential $\phi = 961$ MV
Right: Deviation percentage to ICRU reference values in Table 32

R_C [GV]	$\dot{H}^*(10)$ [µSv/h]			Deviation from ICRU reference values		
	FL310 ~ 9.45 km	FL350 ~ 10.67 km	FL390 ~ 11.89 km	FL310 ~ 9.45 km	FL350 ~ 10.67 km	FL390 ~ 11.89 km
0	3.6	4.8	6.0	-3%	+2%	+5%
1	3.6	4.8	6.0	0%	+4%	+7%
2	3.5	4.6	5.7	+2%	+4%	+7%
3	3.2	4.1	5.1	-4%	+1%	+1%
4	2.8	3.7	4.5	-5%	-5%	-4%
5	2.6	3.3	4.0	-8%	-8%	-7%
6	2.3	3.0	3.6	-11%	-10%	-11%
7	2.1	2.7	3.2	-11%	-9%	-13%
8	1.9	2.5	2.9	-12%	-12%	-14%
9	1.8	2.3	2.7	-14%	-12%	-13%
10	1.7	2.1	2.5	-11%	-12%	-14%
11	1.6	2.0	2.3	-13%	-11%	-15%
12	1.5	1.9	2.2	-13%	-11%	-13%
13	1.4	1.8	2.0	-12%	-12%	-15%
14	1.3	1.7	1.9	-17%	-13%	-16%
15	1.3	1.6	1.8	-16%	-18%	-18%
16	1.2	1.5	1.7	-19%	-16%	-21%
17	1.2	1.4	1.7	-17%	-20%	-21%

E. Uncertainty analysis

TEPC

The results delivered by the TEPC are dose equivalent rates for the high- and low-LET channel. The total ambient dose equivalent rate is:

$$\dot{H}^*(10)_{total} = k_{lowLET} \cdot \dot{H}_{TEPC\ lowLET} + k_{highLET} \cdot \dot{H}_{TEPC\ highLET} \tag{38}$$

k are the calibration factors for the conversion from dose equivalent rate to ambient dose equivalent rate: $k_{lowLET} = 1.03 \pm 9.3\ \%$

$k_{highLET} = 0.70 \pm 20.9\ \%$

The total uncertainty of the ambient dose equivalent rates for the TEPC flight measurement consists of two components, the statistical error of the measurement and the error of the calibration factors that were used for the conversion from dose equivalent rate to ambient dose equivalent rate.

The statistical error was estimated by the experimental variance of the mean: [45]

$$u^2(\bar{z}) = \frac{1}{n(n-1)} \sum_{i=1}^{n} (z_i - \bar{z})^2 \tag{39}$$

The total error that arises from the statistical error and the error of the calibration factors is given by the law of error propagation: [45]

$$u_{total} = \sqrt{\sum_{i=1}^{n} \left(\frac{\partial f}{\partial x_i}\right)^2 \cdot u^2(x_i)} \tag{40}$$

Simulation

The uncertainty of the output of the simulation model was estimated to be 20 %.